

ABSTRACT

Title of Document: TWO-DIMENSIONAL CRYSTALS ON
SUBSTRATES: MORPHOLOGY AND
CHEMICAL REACTIVITY

Mahito Yamamoto, Doctor of Philosophy, 2013

Directed By: Professor Theodore L. Einstein,
Department of Physics

Two-dimensional crystals such as graphene and transition metal dichalcogenides have emerged as a new class of materials. They serve as rich playgrounds for two-dimensional physics but also have great potential for a wide range of applications due to their exceptional tunability *via* external influences such as electric fields, light, chemical adsorbates, defects, and stress. This dissertation aims to understand, as a fundamental step toward their application, the response of two-dimensional crystals to such external perturbations imposed by supporting substrates.

First, the mechanical response of graphene supported on corrugated substrates is studied. I find that the structural evolution of graphene depends on the roughness of the substrate and the graphene thickness. On SiO₂ substrates decorated with a low-density of SiO₂ nanoparticles, adhesion dominates graphene elasticity and, hence, graphene conforms to the substrate. With increasing nanoparticle density, however, the elastic stretching energy is reduced by the formation of wrinkles. As the graphene

membrane is made thicker, graphene becomes stiffer and delaminates from the substrate.

Second, the effect of substrates on chemical reactivity of graphene is probed. Single-layer graphene on low charge-trap density boron nitride is not etched and shows little doping after oxygen treatment, in sharp contrast with oxidation under similar conditions of graphene on high charge-trap density SiO_2 and mica. Furthermore, bilayer graphene shows reduced reactivity compared to single-layer graphene regardless of its substrate-induced roughness. Together the observations indicate that graphene's reactivity is predominantly controlled by charge-inhomogeneity-induced potential fluctuations rather than by surface roughness.

Lastly, the oxidative reactivity of atomically thin molybdenum disulfide (MoS_2) on SiO_2 is studied. MoS_2 is etched by oxygen treatment. However, unlike graphene on SiO_2 , the density of etch pits barely depends on MoS_2 thickness, oxidation time, oxidation temperature, but varies significantly from sample to sample. The observations suggest that the oxidative etching of atomically thin MoS_2 is initiated at native defect sites on the basal-plane surface rather than activated by substrate effects such as charged impurities and surface roughness.

The findings provide insight into the mechanical and chemical properties of two-dimensional crystals and may have important implications for their applications.

TWO-DIMENSIONAL CRYSTALS ON SUBSTRATES: MORPHOLOGY AND
CHEMICAL REACTIVITY

By

Mahito Yamamoto

Dissertation submitted to the Faculty of the Graduate School of the
University of Maryland, College Park, in partial fulfillment
of the requirements for the degree of
Doctor of Philosophy
2013

Advisory Committee:
Professor Theodore L. Einstein, Chair
Professor Michael S. Fuhrer
Dr. William G. Cullen
Professor Ellen D. Williams
Professor John D. Weeks

© Copyright by
Mahito Yamamoto
2013

Dedication

To my parents, my wife Maki, and my coming baby.

Acknowledgements

I would like to thank my adviser, Professor Theodore Einstein for his support during my Ph.D. studies. He gave me many insightful feedbacks from the viewpoint of a theoretical physicist and motivated me to do further experimental research. He always made very careful and helpful corrections to my talk slides, manuscripts, and research proposals. I learned many things from Ted. One of the most important things is when I should or should not put a definite article before a noun (I am still sometimes confused with this issue, though).

I would also like to thank Professor Michael Fuhrer for advising me on this dissertation work. I was always amazed at the group meeting by his ability to understand quickly the implications of experimental results which I showed him. His broad knowledge and intuition always guided me in the right direction and helped me to produce more outputs than I expected. I feel very fortunate to have worked for Michael and to have found a scientist who I want to be like at Maryland.

I am grateful to Dr. Bill Cullen for his support throughout my graduate studies for five years. Bill was always available whenever I needed his help and welcomed me to ask any kind of questions, from equipment's troubleshooting to research direction to how to hit a softball. He was very patient with me and his answers were always very clear and succinct. I could not complete any of experiments present in this dissertation work without his great help.

I cannot thank my former advisor Professor Ellen Williams enough for generously letting me join the Williams group and motivating me to do this dissertation work. Literally, I could not be here in Maryland (and could not find my

wife and have a baby) without Ellen. Her remarkable insight, knowledge, and great personality made me decide to come to Maryland when I was a master student at Osaka University in Japan. Now I am very proud of myself for making this decision. Her decision-making speed always amazed me and her supervision always directed me to the right path. Even though I worked for her for only a couple years, it was one of the most precious experiences in my life.

I would like to thank Professor John Weeks for agreeing to serve as a Dean's Representative and sparing his time to read my dissertation. I am very lucky to have chance to get feedback from such a prestigious scientist.

I would also like to thank Dr. Olivier Pierre-Louis for his theoretical contributions to my work and for choosing a good wine for my wife the other day. He has incomparable insight into any kind of physics problems and I was very impressed when he made theoretical models very quickly and they fit to my experimental results. Without doubt, I could not complete my dissertation work without collaboration with Olivier.

I would like to thank Professor Teng Li for inspiring me to do relevant experimental work. I would also like to thank Professor Santiago Solares for allowing me to use his facilities. I also thank Dr. Daniel Ebeling and Babak Eslami for helping me to do experiments at the Solares lab. I thank Professor Janice Reutt-Robey for her insightful and fruitful feedbacks at the surface physics seminar.

I would like to thank the former members of Ellen's and Michael's groups. Especially, I would like to thank Professor Jianhao Chen for teaching me many experimental techniques at the early stage of my Ph.D. study and for being such a

nice office mate. I would also like to thank Professor Jia Huang, who has diverse knowledge in chemistry. I learned from him most of chemistry experimental techniques. I thank Professor Brad Conrad, Dr. Tracy Moore, Blake Riddick, Dr. Chaun Jang, Professor Jun Yan, and Dr. Shudong Xiao.

I am grateful to the current members, Michelle Groce, Kristen Burson, Liang Li, Jinglei Ping, Jacob Tosado, Harold Cai, Dr. Dohun Kim, Jack Hellerstedt, Dr. Wenzhong Bao, and Dr. Yilin Wang for being good labmates. They are all talented experimentalists and discussion with them always inspired me very much.

I would like to thank all the staff of the Physics Department and MRSEC. Especially, I would like to thank Margaret Lukomska, Jane Hessing, Donna Hammer, Julie Callis, Linda O'Hara, Paulina Alejandro, and Pauline Rirksopa.

I am deeply grateful to Professor Hiroshi Iwasaki and Professor Koichi Sudoh at Osaka University for motivating me to come to study at the University of Maryland.

I would like to extend my appreciation to those outside of physics. Especially, I thank Yu Izumi and Mio Izumi for being good friends. Without occasional chatting with Yu and Mio with beer, I could not survive my Ph.D. studies at Maryland. I would also like to thank Chizuru Nakano, Tetsuaki Nakano, Akira Omaki, Masaya Yoshida, Mike Hull, Shizuka Nakayama, Kenshi Funakoshi, Sayaka Funakoshi, Masaki Ishikawa, Momoko Ishikawa, Shota Monma, Ayaka Negishi, Naoki Yamamoto, Yasuyuki Nakajima, and Shingo Maruyama. I also thank Jen-Chien Chang.

Lastly, and most importantly, I would like to thank my wife Maki for her constant support and encouragement throughout my graduate career. Being with Maki

is the best way to relax and to cheer up all of the time. I could never complete this dissertation work without her.

Table of Contents

Dedication	ii
Acknowledgements.....	iii
Table of Contents	vii
List of Tables	x
List of Figures	xi
Chapter 1: Introduction	1
1.1 “Discovery” of graphene.....	1
1.2 Two-dimensional crystals beyond graphene.....	2
1.3 Two-dimensional crystals as “all-surface” materials.....	3
Chapter 2: Strain- and chemical-engineering of the electronic properties of two-dimensional crystals: Background	5
2.1 The band structure of graphene.....	5
2.2 Dirac fermions in graphene.....	8
2.3 Effects of strain on the electronic structures of graphene.....	9
2.4 Chemical functionalization of graphene	12
2.5 The electronic properties of MoS ₂	13
2.6 Chemical functionalization of MoS ₂	15
Chapter 3: Experimental techniques	17
3.1 Preparation of 2D crystals.....	17
3.2 Sample cleaning	20
3.3 Atomic force microscopy.....	20
3.4 Raman spectroscopy	22

Chapter 4: Raman spectroscopy of graphene and MoS ₂	25
4.1 Main Raman features of graphene	25
4.2 The dependence of the G' band on the thickness of graphene	27
4.3 Effect of doping on the Raman G mode	29
4.4 Determining the defect density in graphene through the Raman D mode	30
4.5 The Raman E _{2g} ¹ and A _{1g} modes of MoS ₂	31
Chapter 5: Morphological transitions of graphene on nano-patterned substrates.....	33
5.1 Morphology of graphene on substrates.....	34
5.2 Experimental details.....	34
5.3 Experimental results.....	36
5.4 Elastic analyses of structural transitions of graphene	39
5.4.1 Wrinkling of single-layer graphene	39
5.4.2 Delamination of graphene multilayers.....	44
5.5 Pseudomagnetic fields in graphene on nanoparticles	48
5.6 Statistical mechanical analyses of graphene wrinkling	53
5.6.1 Random wrinkling model	53
5.6.2 Percolation transition in the wrinkle network.....	56
5.7 Conclusions.....	59
Chapter 6: Oxidative reactivity of graphene on substrates	61
6.1 Chemical reactivity of graphene	61
6.2 Experimental details.....	63
6.3 Experimental results and discussion	66
6.4 Conclusions.....	77

Chapter 7: Oxidative reactivity of atomically thin MoS ₂ on SiO ₂	78
7.1 Oxidative reactivity of MoS ₂	78
7.2 Experimental details.....	79
7.3 Experimental results and discussion	80
7.4 Conclusions.....	91
Chapter 8: Conclusions and outlook	93
Appendix A: Scaling analysis of the wrinkle length	96
Bibliography	99

List of Tables

Table 6.1: The RMS roughness σ , the characteristic length l , the estimated curvature σ/l^2 , and strain $(\sigma/l)^2$ of SLG on hBN, mica, SiO ₂ , and SiO ₂ nanoparticles (NPs) and BLG on NPs	64
---	----

List of Figures

Figure 2.1: The honeycomb lattice and Brillouin zone of single-layer graphene	6
Figure 2.2: The band structure of graphene	6
Figure 2.3: The uniaxially stretched honeycomb lattice of graphene	9
Figure 2.4: Covalent functionalization of graphene	12
Figure 2.5: The crystal structure of 2H-MoS ₂	14
Figure 2.6: The band structure of single-layer MoS ₂ for the first Brillouin zone.....	15
Figure 3.1: The procedure of mechanical exfoliation of a 2D crystal	18
Figure 3.2: Optical images of mechanically exfoliated 2D crystals on SiO ₂	19
Figure 3.3: A schematic of the principle of AFM.....	21
Figure 3.4: Tip-sample force F as a function of tip-sample distance z for tapping mode AFM	22
Figure 3.5: Rayleigh and Raman scattering in electronic states	23
Figure 4.1: The Raman spectrum of graphene with defects	25
Figure 4.2: The Raman G, D, and G' modes of graphene	26
Figure 4.3: The dispersive behaviors of the D and G' modes	27
Figure 4.4: The G' band of bilayer graphene	28
Figure 4.5: The G' band of single- and few-layer graphene.....	29
Figure 4.6: The Raman spectra of atomically thin MoS ₂	31
Figure 5.1: AFM images of SiO ₂ -nanoparticle-decorated SiO ₂ substrates.....	35
Figure 5.2: Height distribution of SiO ₂ nanoparticles on SiO ₂ substrates	36
Figure 5.3: AFM images of single-layer graphene on SiO ₂ nanoparticles/SiO ₂ substrates for various nanoparticle densities.....	37

Figure 5.4: AFM images of graphene layers on SiO ₂ with nanoparticles with the density of $160 \pm 24 \mu\text{m}^{-2}$	38
Figure 5.5: AFM height and phase images of a delaminated graphene multilayer on nanoparticles	39
Figure 5.6: An AFM image of a wrinkle formed between two nanoparticles	40
Figure 5.7: Schematics of a wrinkle	41
Figure 5.8: The deflection of a wrinkle	43
Figure 5.9: The distribution of lengths of the wrinkles	44
Figure 5.10: The conformed area and the characteristic length of delaminated graphene on nanoparticles.....	45
Figure 5.11: A schematic of graphene on a single nanoparticle	46
Figure 5.12: Strain-induced pseudomagnetic fields in graphene on an isolated nanoparticle.....	50
Figure 5.13: The cyclotron radius for Dirac fermion as a function of carrier density for $B = 300 \text{ T}$	51
Figure 5.14: The density of wrinkles as a function of nanoparticle density	53
Figure 5.15: Particle-particle correlation functions of covered- and uncovered-nanoparticles	54
Figure 5.16: The number of wrinkles propagating from single nanoparticles.....	55
Figure 5.17: Percolation transition in the wrinkle network	56
Figure 5.18: Percolation analyses of the wrinkle network.....	57
Figure 5.19: The orientations of wrinkles.....	58
Figure 6.1: Optical images of graphene on various substrates	62

Figure 6.2: AFM images of graphene supported on various substrates.....	63
Figure 6.3: AFM images of SLG supported on various substrates after oxidation at 500 °C for 2 hours.....	65
Figure 6.4: Raman spectra of SLG on various substrates before and after oxidation at 500 °C for 2 hours.....	66
Figure 6.5: Non-dispersive behavior of the Raman E_{2g} mode of BN	67
Figure 6.6: The Raman G band energies of oxidized graphene on substrates as functions of temperature and graphene thickness	68
Figure 6.7: Oxidation of graphene on SiO_2 and BN at 450 °C for 5 hours	69
Figure 6.8: An AFM phase image of pristine graphene on SiO_2	70
Figure 6.9: A series of Raman spectra of oxidized SLG on SiO_2 and BN	71
Figure 6.10: The Raman G' modes of oxidized graphene on various substrates	72
Figure 6.11: An AFM image of water islands trapped between SLG and mica.....	73
Figure 6.12: Raman spectra of oxidized graphene on SiO_2 nanoparticles.....	74
Figure 7.1: Atomically thin MoS_2 on SiO_2 after H_2 annealing.....	78
Figure 7.2: Atomically thin MoS_2 on SiO_2 after O_2 annealing	79
Figure 7.3: AFM images of triangular etch pits on atomically thin MoS_2	79
Figure 7.4: Schematic drawings of hexagonal lattice of the MoS_2 structure with triangular pits	80
Figure 7.5: The depth of the triangular pits	81
Figure 7.6: An AFM image of atomically thin MoS_2 on SiO_2 after O_2 annealing at 320 °C for 3 hours.....	81

Figure 7.7: A series of AFM images of single- and bi-layer MoS ₂ oxidized at 320 °C	82
Figure 7.8: The growth rate of the triangular pits.....	83
Figure 7.9: AFM images of MoS ₂ samples of various thicknesses after oxidation at 320 °C for 2 hours.....	83
Figure 7.10: AFM images of single- and bi-layer MoS ₂ oxidized at various temperatures.....	84
Figure 7.11: Histogram of the density of pits formed on single- and few-layer MoS ₂ oxidized at various temperatures	85
Figure 7.12: Raman spectra of oxidized atomically thin MoS ₂	87
Figure 7.13: An AFM image and a Raman spectrum of thick MoS ₂ oxidized at a high temperature	88
Figure 7.14: The Raman E _{2g} ¹ and A _{1g} modes of oxidized single-layer MoS ₂	89
Figure 7.15: The Raman E _{2g} ¹ and A _{1g} modes of oxidized single- and few-layer MoS ₂	90

Chapter 1: Introduction

1.1 “Discovery” of graphene

Graphene, a one-atom-thick sheet made of carbon atoms arranged in honeycomb lattice, was first theoretically considered by Wallace to understand the electronic properties of graphite, the stack of graphene layers, nearly 70 years ago [1, 2]. In the 1980's, graphene with its “massless” dispersion near Dirac points was highlighted as a condensed matter counterpart of quantum electrodynamics [1, 3], triggering further theoretical studies with a renewed interest. However, no compelling evidence for the presence of graphene had been reported until 2004. In 2004, Andre Geim and Kostya Novoselov at the University of Manchester isolated, for the first time, thin graphite (or few-layer graphene) from bulk graphite on SiO₂ by using a strikingly simple technique, the so called “Scotch tape method”, and demonstrated an ambipolar field effect device based on graphene [4]. The exfoliated graphene flakes are amazingly stable even at room temperature, defect-free at the micrometer scale, and show high crystal quality. These have all propelled, in addition to the simplicity of the isolation technique and the fabrication of field-effect devices, a surge of experiments on graphene with a great emphasis on transport measurement. In particular, the observation of Dirac fermions in single-layer graphene in 2005 paved the way for a new realm of condensed matter physics [5, 6]. As a first truly 2D material, graphene has been extensively studied, demonstrating many unusual properties including extraordinary mechanical strength [7] and ultrahigh thermal conductivity [8].

1.2 Two-dimensional crystals beyond graphene

After the first isolation of graphene in 2004 [4], Novoselov *et al.* applied a mechanical exfoliation method to other layered materials such as boron nitride (BN), molybdenum disulfide (MoS_2), niobium diselenide (NbSe_2), and $\text{Bi}_2\text{Sr}_2\text{CaCu}_2\text{O}_x$ [9]. Initially, these materials have drawn little attention, compared to graphene, likely because they show, at a glance, less remarkable electronic properties than graphene. However, the study of 2D materials beyond graphene has been spurred recently by several important observations. First, in 2010, Dean *et al.* reported a technique for transferring graphene onto BN and demonstrated high-quality graphene devices of which carrier mobility is an order of magnitude higher than typical SiO_2 -supported graphene devices [10]. This result emphasizes the importance of BN as a graphene support but also opens up the possibility of creating unconventional van der Waals heterostructures based on 2D materials [11-13].

Other inspiring observations are high-carrier mobility [14] and strong photoluminescence of single-layer MoS_2 [15]. These observations have important implications for a wide variety of applications of 2D transition metal dichalcogenides in electronics and optoelectronics [16]. Furthermore, more recently, two groups independently demonstrated control of valley polarization in single-layer MoS_2 by optical pumping [17, 18], pointing out the possibility of novel electronics exploiting the valley degree of freedom of matter — valleytronics. As frontiers beyond graphene, 2D materials such as BN and transition metal dichalcogenides and their heterostructures are of increasing interest in condensed matter physics and for applications [19].

1.3 Two-dimensional crystals as “all-surface” materials

One of the most interesting aspects of 2D materials is, obviously, that they are truly 2D electron systems and could provide unusual phenomena hidden in quasi-2D systems such as semiconductor inversion layers. However, another unique feature of 2D crystals is that they consist entirely of surfaces. This “all-surface” aspect of 2D materials contributes to the exceptional sensitivity of their properties to external influences. For example, the width and the edge structures of a 2D crystal nanostructure determine the size of the band gap [20]. Disorder modifies significantly the electric and thermal conductivities [21, 22]. Point defects induce magnetism [23, 24], and strain mimics the effect of a magnetic field in single-layer graphene [25]. Furthermore, various properties such as work function [26], infrared reflectivity [27], and the amplitude and the wavelength of plasmons [28, 29] in graphene are widely tunable *via* electric fields. The extraordinary sensitivity (or tunability) of 2D crystals suggests a wide variety of electronic applications ranging from chemical sensors [30] to photodetectors [31, 32].

This dissertation concerns the all-surface aspect of 2D crystals, particularly, how their morphology and reactivity are affected by supporting substrates due to the all-surface nature. The substrate has two major effects on a 2D crystal; potential fluctuations due to trapped charged impurities [33, 34] and surface roughness caused by adhesion [35, 36], both of which are expected to modify the physical and chemical properties of a 2D crystal in various manners. For example, charged impurities are observed to limit the carrier mobility of graphene [37], and surface roughness is predicted to diminish graphene’s electric and thermal conductivity [21, 22, 38].

However, their effects on morphology and chemical reactivity have remained unclear, although the information is essential for mechanically- (or strain-) and chemically-tuning the electronic properties of 2D crystals.

In this dissertation, I experimentally explore (i) structures of graphene membranes supported on surfaces of varying roughness, (ii) oxidative reactivity of graphene on various substrates with different surface roughnesses and charged impurities, and (iii) oxidative reactivity of atomically thin MoS₂ on SiO₂. This dissertation is organized as follows. Chapter 2 introduces the electronic, mechanical, and chemical properties of graphene and MoS₂ and how they are coupled to each other. Chapter 3 describes experimental techniques used in this work. Chapter 4 reviews the Raman spectroscopy of graphene and MoS₂. Chapter 5 presents the study of morphology of graphene supported on rough substrates. Chapter 6 discusses the impact of substrates on chemical reactivity of graphene. Chapter 7 investigates the chemical reactivity of single- and few-layer MoS₂ supported on SiO₂. Lastly, Chapter 8 summarizes this dissertation and provides some outlook on future work.

Chapter 2: Strain- and chemical-engineering of the electronic properties of two-dimensional crystals: Background

Due to their “all-surface” nature, two-dimensional (2D) crystals exhibit exceedingly tunable electronic properties *via* external influences such as electric/magnetic fields, light, structural defects, chemical adsorbates, and mechanical deformations. In this chapter, I review how strain and chemical species affect and, hence, can be used to engineer the electronic properties of graphene and atomically thin MoS₂. In Sections 2.1 and 2.2, I introduce the unusual electronic properties of single-layer graphene. Then, I discuss how its electronic structures can be modified by mechanical strain in Section 2.3 and chemical treatment in Sections 2.4. In Section 2.5, I review the electronic structures of single-layer MoS₂ and show potential applications of chemical functionalization of MoS₂ in Section 2.6

2.1 The band structure of graphene

I begin this chapter by reviewing the electronic properties of graphene. Graphene is made of carbon atoms arranged in a honeycomb lattice as shown in Fig. 2.1a. The honeycomb lattice consists of two triangular A and B sublattices described by two unit vectors $\mathbf{a}_1 = (3a/2, \sqrt{3}a/2)$ and $\mathbf{a}_2 = (3a/2, -\sqrt{3}a/2)$, where $a = 1.42 \text{ \AA}$ is the spacing between the nearest neighbor carbon atoms. The lattice constant of the unit cell is $\sqrt{3}a \approx 2.46 \text{ \AA}$. Figure. 2.1b shows Brillouin zone of graphene with the first Brillouin zone depicted by shaded area. The unit vectors in momentum space are given by $\mathbf{b}_1 = (2\pi/3a, 2\pi/\sqrt{3}a)$ and $\mathbf{b}_2 = (2\pi/3a, -2\pi/\sqrt{3}a)$. Among the three high

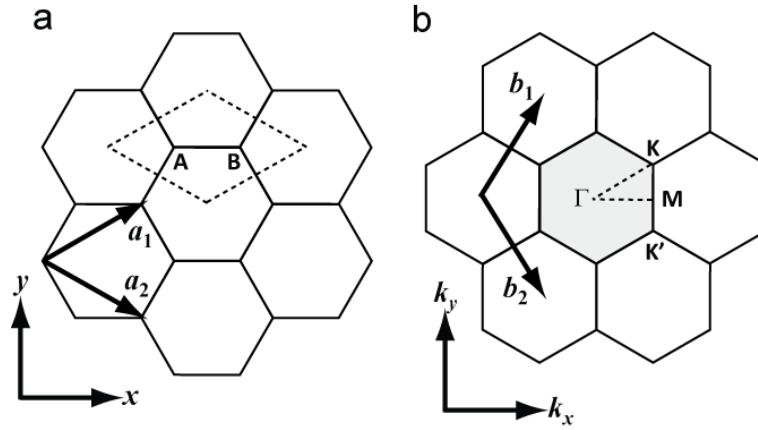


Figure 2.1: The honeycomb lattice and Brillouin zone of single-layer graphene. (a) The unit cell is represented by dashed lines. (b) The first Brillouin zone is represented by the shaded area.

symmetric points Γ , K , and M in momentum space, $\mathbf{K} = (2\pi/3a, 2\pi/3\sqrt{3}a)$ and $\mathbf{K}' = (2/3a, -2\pi/3\sqrt{3}a)$ are particularly called Dirac points because electrons behave as massless Dirac fermions near the points as shown below.

In the tight-binding language, π electrons at atomic sites “hop” to neighboring atomic sites with hopping energies. When only nearest neighbor hopping is

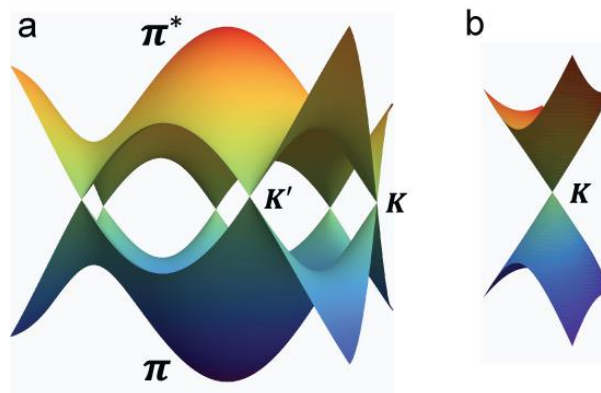


Figure 2.2: The band structure of graphene. (a) The energy spectrum for the first Brillouin zone and (b) the linear energy dispersion, “Dirac cone”, near a K point.

considered, the tight-binding Hamiltonian for π electrons can be approximately described as $H = -t \sum_{i,j} a_i^\dagger b_j + \text{H.c.}$, where $a^\dagger(a)$ is the creation (the annihilation) operator for the A sublattice, b (b^\dagger) is the annihilation (the creation) operator for the B sublattices, and $t \approx 2.8$ eV is the energy for nearest-neighbor hopping [21]. From this Hamiltonian, the energy band of graphene can be derived as

$E(\mathbf{k}) = \pm t |1 + e^{ik \cdot a_1} + e^{ik \cdot a_2}|$ [3, 21, 39], where the positive energy corresponds to an antibonding π^* band (particle band) and the negative energy corresponds to a bonding π band (hole band) [21, 39]. Figure 2.2 shows the energy spectrum of graphene for the first Brillouin zone. As shown in Fig. 2.2a, the valence and the conduction bands touch each other at K and K' points. Hence, graphene is a zero-band-gap semiconductor or a semimetal.

The zero energy gap of graphene critically hinders its applications in electronics. Opening the band gap of graphene is, thus, of central interest. An approach is to create a narrow graphene strip with a width of < 100 nm (graphene nanoribbons) so that electrons are confined in quasi-one-dimension. The band gap in a graphene nanoribbon depends on its width and the edge terminations [20, 40]. Furthermore, first-principles calculation predicts that uniaxial strain along zigzag directions of the graphene lattice breaks sublattices symmetry and opens the energy gap which increases nearly linearly with increasing magnitude of the strain [41]. Another theoretical prediction is that when graphene is commensurately deposited onto BN, the inequivalence of two A and B carbon atoms results in a computed gap of 53 meV [42]. For bilayer graphene, an electric field perpendicular to the plane can

create a tunable band gap due to the lowering of the symmetry [43, 44]. Furthermore, chemical functionalization can be used to control the band gap of graphene as described in Section 2.4.

2.2 Dirac fermions in graphene

Since the Fermi energy intersects $E(\mathbf{k})$ at the K and K' points, the electrons around the points determine the low-energy electronic properties of graphene. By expanding $E(\mathbf{k})$ around a point $\mathbf{k} = \mathbf{K} + \mathbf{q}$ with $|\mathbf{q}| \ll |\mathbf{K}|$, the energy dispersion can be written as $E(\mathbf{q}) = \pm \hbar v_F |\mathbf{q}|$, where $v_F = 3ta/2\hbar \approx 1.0 \times 10^6$ m/s is the Fermi velocity [21]. This linear energy dispersion near K (K') points is similar to the energy spectrum of ultrarelativistic particles which are described by the massless Dirac equations and are, thus, called Dirac cones as depicted in Fig. 2.2b. Indeed, by expanding the electron operators a and b around K and K' points, the tight-binding Hamiltonians are also described as massless Dirac Hamiltonians:

$$H_K = \hbar v_F \begin{pmatrix} 0 & k_x - ik_y \\ k_x + ik_y & 0 \end{pmatrix} = \hbar v_F \boldsymbol{\sigma} \cdot \mathbf{k} \quad (2.1)$$

around K and

$$H_{K'} = \hbar v_F \begin{pmatrix} 0 & k_x + ik_y \\ k_x - ik_y & 0 \end{pmatrix} = \hbar v_F \boldsymbol{\sigma}^* \cdot \mathbf{k} \quad (2.2)$$

around K' with eigenenergies being $E(\mathbf{k}) = \pm \hbar v_F \mathbf{k}$ [21].

The Dirac-fermions in single-layer graphene were experimentally confirmed by the observations of a half-integer quantum Hall effect, Berry's phase, and cyclotron mass which depends on the square root of carrier density [5, 6]. Furthermore, experimental studies have shown that graphene exhibits various unusual

properties such as ballistic transport with a mean free path of up to $1 \mu\text{m}$ [4, 45, 46], Klein tunneling [47, 48], and a half-integer quantum Hall effect at room temperature [49] due to the nature of the Dirac fermions.

2.3 Effects of strain on the electronic structures of graphene

As illustrated in the previous section, graphene shows many peculiar electronic properties due to the Dirac fermion-like behavior of low-energy electrons. Of particular interest is that non-uniform strain in graphene can mimic the effect of a magnetic field on the electronic structure, suggesting the possibility of “strain-engineering” of the electronic properties. In this section, I review how strain could perturb graphene’s Dirac fermions.

Strain changes local carbon-carbon distances as shown in Fig. 2.3, leading to modification of hopping energy t between neighboring p_z orbitals on lattice sites \mathbf{R}_i and $\mathbf{R}_j = \mathbf{R}_i + \boldsymbol{\delta}$ ($\boldsymbol{\delta}_{ab}$ is the nearest neighbor vector and $\boldsymbol{\delta}_{aa}$ is the next-nearest neighbor vector) to $t' = t + \delta t_{ij}$. Therefore, the tight-binding Hamiltonian is also modified to

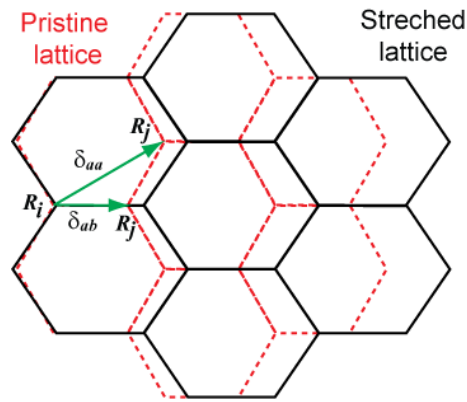


Figure 2.3: The uniaxially stretched honeycomb lattice of graphene. The pristine and stretched graphene lattices are represented by the red dashed and the black solid lines, respectively.

$$H' = H + \sum_{i,j} \left[\delta_{ij}^{(ab)} (a_i^\dagger b_j + \text{H.c.}) + \delta_{ij}^{(aa)} (a_i^\dagger a_j + b_i^\dagger b_j) \right], \quad (2.3)$$

where the superscripts (ab) and (aa) correspond to the nearest-neighbor and the next-nearest-neighbor hopping, respectively [21]. By expanding the electron operators around the Dirac points K and K' in analogy with the approach in the previous section, the Dirac Hamiltonian can be obtained as

$$H_K = \hbar v_F \begin{pmatrix} 0 & k_x - ik_y \\ k_x + ik_y & 0 \end{pmatrix} + \begin{pmatrix} \Phi & A_x - iA_y \\ A_x + iA_y & \Phi \end{pmatrix} \quad (2.4)$$

around K and

$$H_{K'} = \hbar v_F \begin{pmatrix} 0 & k_x + ik_y \\ k_x - ik_y & 0 \end{pmatrix} + \begin{pmatrix} \Phi & -A_x + iA_y \\ -A_x - iA_y & \Phi \end{pmatrix} \quad (2.5)$$

around K' , with

$$A(r) = \sum_{\delta_{ab}} \delta_{ab}^{(ab)}(r) e^{-i\delta_{ab} \cdot \mathbf{K}} \quad (2.6)$$

and

$$\Phi(r) = \sum_{\delta_{aa}} \delta_{aa}^{(aa)}(r) e^{-i\delta_{aa} \cdot \mathbf{K}}. \quad (2.7)$$

Here $\Phi(r) = \Phi^*(r)$ due to the inversion symmetry of the two triangular sublattices, while $A(r)$ is complex because of a lack of inversion symmetry for nearest-neighbor hopping. These Dirac Hamiltonians indicate that low-energy electrons in strained graphene behave as if they were subject to both scalar Φ and vector $A = A_x + iA_y$ potentials, along with pseudomagnetic fields $\mathbf{B} = (c/v_F) \nabla \times \mathbf{A}$. On symmetry grounds, the vector and scalar potentials can be expressed by strain tensors u_{ij} [50, 51]:

$$\Phi(\mathbf{r}) = g_1(u_{xx} + u_{yy}), \quad (2.8)$$

$$A_x = g_2(u_{xx} - u_{yy}), \quad (2.9)$$

$$A_y = 2g_2u_{xy}, \quad (2.10)$$

where $\mathbf{u}(\mathbf{r}) = (u_x, u_y)$ is the in-plane displacements, with the x -axis being a zigzag direction, $g_1 \approx 3.0$ eV, and $g_2 \approx 2.3$ eV [52]. When the transverse displacement of graphene h is small [53], two-dimensional strain elements u_{ij} are approximated by

$$u_{xx} = \frac{\partial u_x}{\partial x} + \frac{1}{2} \left(\frac{\partial h}{\partial x} \right)^2, \quad (2.11)$$

$$u_{yy} = \frac{\partial u_y}{\partial y} + \frac{1}{2} \left(\frac{\partial h}{\partial y} \right)^2, \quad (2.12)$$

$$u_{xy} = \frac{1}{2} \left(\frac{\partial u_x}{\partial y} + \frac{\partial u_y}{\partial x} \right) + \frac{1}{2} \frac{\partial h}{\partial x} \frac{\partial h}{\partial y}. \quad (2.13)$$

By Eqs. (2.8)-(2.10), along with Eqs. (2.11)-(2.13), the effective scalar and vector potentials (or pseudomagnetic fields) can be directly related to strain fields u_{ij} or displacements of the lattice $\mathbf{u}(\mathbf{r}) = (u_x, u_y)$, implying that one could, in principle, tailor graphene's electronic structures by appropriately designing strain or, more simply, the associated morphology. Indeed, specific strain profiles are predicted to create confined states, quantum wires, and electron collimation in the electronic structure of graphene [54]. Additionally, a theoretical calculation has shown that when graphene is corrugated with triangular symmetry along the crystallographic directions, strain in graphene induces pseudomagnetic fields and creates energy gaps of greater than 100 K due to the quasi-Landau quantization [55].

Experimentally, strain-induced pseudomagnetic fields have been observed by scanning tunneling spectroscopy in graphene nanobubbles formed on Pt(111) [25] and suspended graphene deformed by a STM tip [56]. In the graphene nanobubbles, large triangular symmetric strain generates pseudomagnetic fields exceeding 300 T, resulting in Landau quantization of the energy levels [25]. In deformed suspended graphene, pseudomagnetic fields were found to confine electrons to quantum dots with charging energies and level spacings both of order 10 meV [56]. Theoretical proposals together with these observations signify that strain-engineering could be a promising approach for controlling graphene's electronic structures.

2.4 Chemical functionalization of graphene

Chemical functionalization is an approach to tailoring the physical and chemical properties of a material by either covalently or non-covalently bonding molecules or atoms to its surfaces or edges. Previous studies have shown that chemical modification is effective in engineering the electronic, thermal, and,

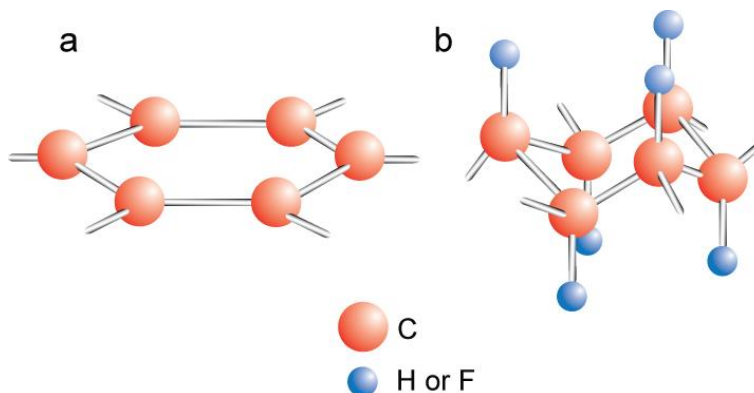


Figure 2.4: Covalent functionalization of graphene. (a) Graphene and (b) hydrogenated or fluorinated graphene which has deformed hexagonal lattices.

mechanical properties of carbon nanotubes – rolled-up graphene sheets [57]. Chemical functionalization of graphene has been of great interest for, in particular, engineering its energy band gap. As shown in Fig. 2.2, graphene has no energy gap due to A and B sublattices symmetry, limiting its device applications. Covalent functionalization of graphene changes the hybridization of carbon bonds from sp^2 to sp^3 , removes conducting π -electrons, and, thus, opens the band gap. Indeed, semi-metallic graphene was found to transform into an insulator by hydrogenation [58] or fluorination [59, 60], which are schematically represented in Fig. 2.4. Additionally, the optical band gap [61] as well as transport band gap [62] have been observed in graphene covalently-functionalized with aryl group.

In addition to the band-gap engineering, chemical functionalization can be used to induce unique properties in graphene. For example, fluorination leads to spin-half paramagnetism in graphene [63], and graphene doped with alkali metals is theoretically predicted to show superconductivity [64]. Alternatively, non-covalent functionalization of graphene has great potential for a wide range of applications such as chemical- and bio-sensing devices [65].

2.5 The electronic properties of MoS_2

Now I focus on atomic layers of molybdenum disulfide (MoS_2). MoS_2 is a layered material, of which neighboring layers are coupled by van der Waals interactions with an interlayer spacing of 0.65 nm. Each layer consists of a partially-ionically-bonded S-Mo-S sandwich structure with S atoms arranged in two hexagonal planes and a plane of Mo atoms in between, as shown in Fig. 2.5 [16, 66]. Figure 2.5a

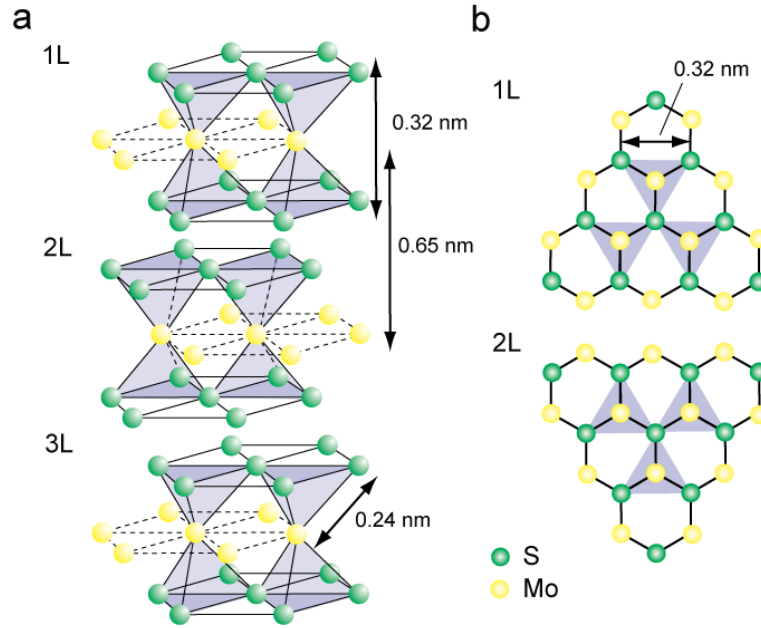


Figure 2.5: The crystal structure of 2H-MoS₂. (a) Three consecutive S-Mo-S layers coupled by van der Waals interaction and (b) top view of the first and second hexagonal lattices, of which triangular lattices (shaded in blue) are 180°-inverted relative to each other.

is the most stable crystal structure of 2H-MoS₂, where trigonal prisms of adjacent layers are 180°-inverted relative to each other and, hence, two layers is a repeat unit.

Bulk MoS₂ is a semiconductor with an indirect gap of 1.2 eV, where the conduction band minimum is at the midpoint along Γ -K symmetry lines and the valence band maximum is at the Γ point [68]. However, single-layer MoS₂ has a direct band gap of 1.9 eV at the K point. The transition from the indirect- to direct-band gap with decreasing thickness is due to quantum confinement and change in the electronic states at the Γ point, which is the combination of p_z orbitals on the S atoms and the d orbitals on the M atoms [15, 16]. Due to its direct-band gap, single-layer MoS₂ emits strong photoluminescence [15].

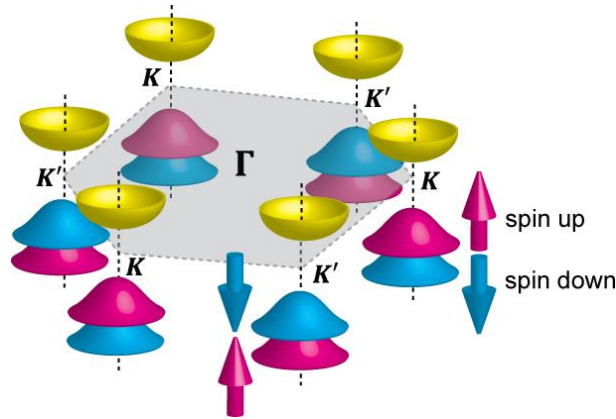


Figure 2.6: The band structure of single-layer MoS₂ for the first Brillouin zone. The conduction bands are represented in yellow. The valence bands are decoupled into two bands due to the spin-orbit coupling [67]. The pink and blue bands correspond to the spin-up and -down states, respectively.

Figure 2.6 shows the band structure of single-layer MoS₂. The valence band has two inequivalent valleys at the K (or K') points because of strong spin-orbit coupling [67, 68]. The two split valleys correspond to two spin states, where the directions of the spins are opposite for different valleys as represented in pink (spin-up) and blue (spin-down) in Fig.2.6. Furthermore, the spin directions are opposite for the K or K' points. Recent experimental studies have demonstrated that electrons at a particular valley (or spin) can be populated selectively by optical pumping [17, 18], opening up the possibility of “valleytronics” [67].

2.6 Chemical functionalization of MoS₂

Chemical functionalization of single- and few-layer MoS₂ has yet to be investigated in detail either experimentally or theoretically, compared to graphene. In this section, I point out a couple potential applications of chemical treatment for MoS₂-based electronics, lubricants, and catalysts.

Atomically thin MoS₂ is a nonmagnetic semiconductor as shown in the previous section. Recent first-principles calculations have shown that single-layer MoS₂ could exhibit magnetism when its surface is functionalized with atoms of 3*d* transition metals, silicon, or germanium [69]. Carrier transport in atomically thin MoS₂ is very sensitive to chemical adsorbates, making it a candidate for chemical sensor applications. So far, single-layer MoS₂ has been demonstrated to be a sensor for nitric oxide gas [70] and triethylamine vapor [71]. Chemical functionalization could open the further possibility of MoS₂-based sensing devices such as biomolecule detectors.

In addition to the electronic and optical properties, MoS₂ has attracted much attention as a solid lubricant [72] and a catalyst for hydrogen evolution reaction ($2\text{H}^+ + 2\text{e}^- \rightarrow \text{H}_2$) [73]. The tribological and catalytic properties of MoS₂ strongly depend on its surface and edges structures. Hence, surface and edge functionalization could enhance the tribological properties and catalytic activity of atomically thin MoS₂ [69].

Chapter 3: Experimental techniques

This chapter outlines experimental techniques used in this dissertation work. In Section 3.1, I explain the preparation method of 2D crystals and, in Section 3.2, I show how to clean the prepared samples. In Sections 3.3 and 3.4, I review the principles of atomic force microscopy (AFM) and Raman spectroscopy.

3.1 Preparation of 2D crystals

The most common method to produce a 2D crystal is mechanical exfoliation [4, 9], where atomically thin crystals are exfoliated from bulk either by pressing an adhesive tape covered with thin flakes onto a substrate or by rubbing thin flakes against the substrate. Mechanical exfoliation yields high-quality crystals for graphene, as clearly demonstrated by observations of a half-integer [5, 6, 49] and fractional [74, 75] quantum Hall effect. However, the method has major drawbacks for practical applications: the low yield of single-layer crystals (likely, less than 10 %) and the small sizes of the samples (at most $\sim 1.0 \times 10^4 \mu\text{m}^2$ in area). An alternative approach for high-yield production of 2D crystals is liquid-phase exfoliation [76-78], where a pristine or intercalated bulk crystal is dispersed in organic solvents and is exfoliated by sonication. This method leads to a high density of atomically thin crystals in suspensions and the suspensions can be drop-cast on an arbitrary substrate. However, the sizes of the chemically exfoliated flakes are typically $< 1 \mu\text{m}^2$ in area. An approach to consistently creating single-layer graphene is graphitization of Si-terminated SiC(0001) in an Ar atmosphere, which results in a large domain size of $\sim 1.0 \times 10^2 \mu\text{m}^2$ [79]. A more versatile route to large-size and high-quality 2D crystals

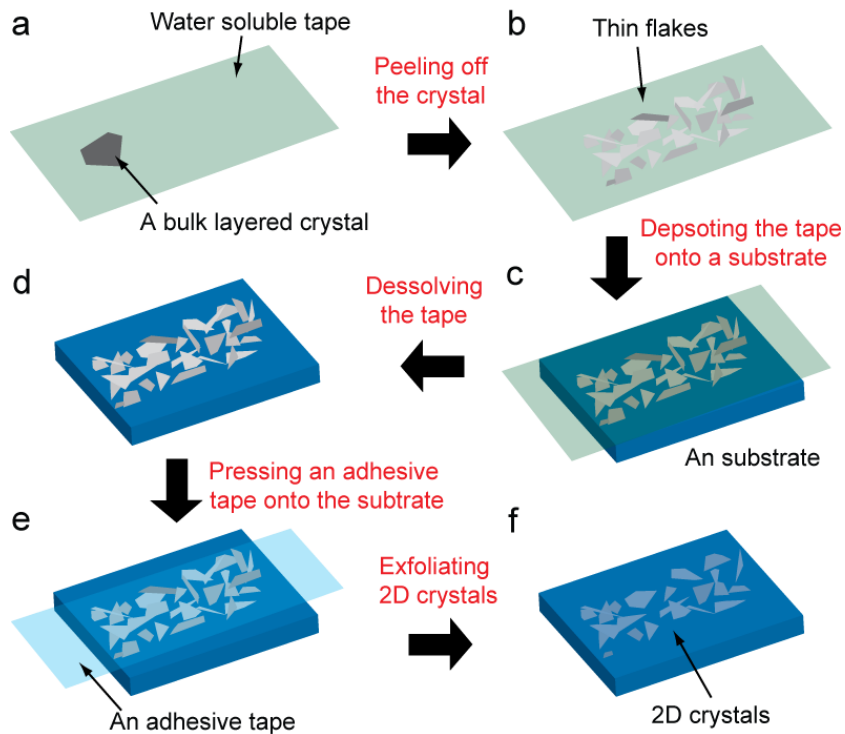


Figure 3.1: The procedure of mechanical exfoliation of a 2D crystal. (a) and (b) Peeling off the bulk crystal into thin flakes by water soluble tape. (c) Deposition of the tape covered with the thin flakes onto a substrate. (d) Dissolution of the tape. (e) and (f) Exfoliation of thin flakes by adhesive tape.

is chemical vapor deposition (CVD). It has been reported that CVD can yield large single-layers of graphene [80-82], BN [83], and MoS₂ [84, 85], and, furthermore, these samples show high sample quality, nearly comparable to mechanically exfoliated crystals [86, 87].

Although various methods have been developed for the production of 2D crystals, mechanical exfoliation has remained the most commonly used technique since the first isolation of thin graphite [4] despite its low-yield. This is mainly because a mechanically exfoliated flake usually shows higher crystal quality than samples obtained by the other methods. Thus, in this work, I used the mechanical

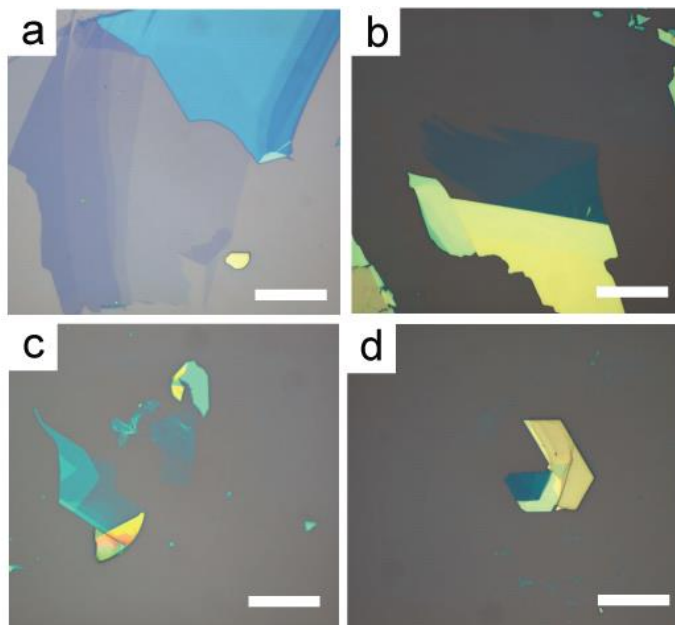


Figure 3.2: Optical images of mechanically exfoliated 2D crystals on SiO₂. (a) Graphene, (b) MoS₂, (c) BN, and (d) WSe₂. Scale bars are 20 μm.

exfoliation method to prepare samples. To enhance the productivity of 2D crystals, I developed an exfoliation method, as described below.

Figure 3.1 summarizes the procedure of the modified mechanical exfoliation. First, a layered bulk material is peeled off by a water soluble tape (3MTM, Water Soluble Solder Tape 5414), as shown in Figs. 3.1a and b. Then, the tape covered with thin flakes is pressed onto a substrate (Fig. 3.1c). The tape is dissolved in boiling water, leaving a large number of thin flakes on the substrate (Fig. 3.1d). Then, the substrate-supported flakes are further exfoliated by an adhesive tape (Figs. 3.1e and f). The last procedure leaves some ultrathin flakes on it.

Figures 3.2a-d are typical optical images of various 2D crystals exfoliated by this method on SiO₂; (a) single- and few-layer graphene films obtained from Kish graphite, (b) single- and bi-layer MoS₂ from a single crystal geologic specimen of

molybdenite, (c) atomically thin BN from BN powder (Momentive, PolarTherm grade PT110), and (d) WSe₂. The sizes of the 2D crystals depend on the initial size of the bulk crystals, but this method yields consistently single-layers of graphene with an area of $\sim 1.0 \times 10^3 \mu\text{m}^2$. In principle, this method can be used for any layered material and on any hydrophobic substrate.

3.2 Sample cleaning

The exfoliation method used here introduces more adhesive residue on the surfaces of 2D crystals than the usual method. Removing the residue is, thus, essential for investigating their morphology and chemical reactivity. In this research, I cleaned graphene samples by annealing in either H₂/Ar mixture or vacuum. Hydrogen annealing was found to be effective to remove a typical electron-beam resist of poly(methyl methacrylate) (PMMA) on graphene [35] and is widely used as a final step of the device fabrication as well as after transfer of a 2D crystal from one substrate to another [10]. In vacuum, graphene is stable and can be heated to the higher temperature of 500 °C. MoS₂ samples were annealed in H₂/Ar at 350 °C before investigating their reactivity. This annealing causes no disorder or chemical modification in MoS₂ as shown later in Chapter 6. The flow rates of Ar and H₂ were 1.7 L/min and 1.8 L/min, respectively.

3.3 Atomic force microscopy

In this research, I used ambient atomic force microscopy (AFM) in tapping mode to characterize the surfaces of graphene and MoS₂. In this section, I briefly review the principle of AFM, in particular, tapping mode AFM. Figure 3.3 depicts

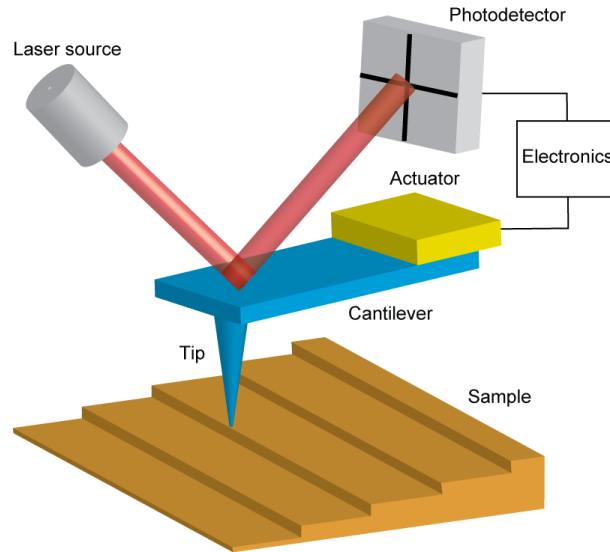


Figure 3.3: A schematic of the principle of AFM.

schematically the principle of AFM. To image a surface of interest, AFM uses forces exerted between the sample surface and a sharp tip. The forces range from van der Waals interactions to electrostatic forces. The tip is attached to a cantilever beam made of typically silicon or silicon nitride, and the response to the forces is measured through the change in deflection or oscillation of the oscillating cantilever. The deflection or the oscillation is detected by using a photodetector which collects reflected laser from the back of the cantilever. The collected information is fed back to the z-direction piezo control to actuate the cantilever at a set point value. The difference between the set point and measured values is translated into the height at a given position [88].

In tapping mode (or intermittent contact mode), the cantilever is oscillated near its resonance frequency with an amplitude of ~ 100 nm. When the tip gets close to the surface (“taps” the surface), the tip-sample forces change the amplitude of the oscillations (Fig. 3.4). Then, the z piezo is modulated such that the amplitude of the

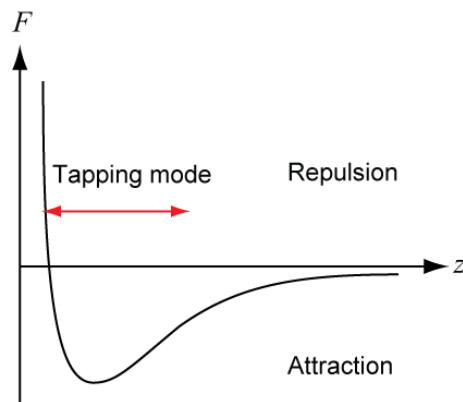


Figure 3.4: Tip-sample force F as a function of tip-sample distance z for tapping-mode AFM. The tapping mode is operated in a range across repulsive and attractive regime as indicated by the double arrow.

cantilever remains a set point value. The tapping mode is a more moderate technique than contact mode, where the tip is in continuous contact with a surface. Thus, it is especially effective for soft samples such as biomolecules or membranes.

In this research, I used mainly Digital Instruments Multimode AFM and silicon cantilevers with a nominal tip radius of < 10 nm (Nanoworld, NCH-20 or Olympus, OMCL-AC160TS).

3.4 Raman spectroscopy

Raman spectroscopy provides information on chemical and physical structures of a matter. In this dissertation work, I used Raman spectroscopy to identify the thickness of graphene and atomically thin MoS_2 films and to characterize their chemical reactivity. In this section, I introduce the principle underlying Raman spectroscopy and, therefore, the Raman spectrum of graphene and MoS_2 will be discussed in detail in Chapter 4.

When a material is illuminated by light, the incident photon interacts with electrons in the material in various manners. For example, the photon can be virtually absorbed by the material by shaking the electrons. The excited electrons scatter the energy back to another photon, emitting light with the same energy as the incident light. This elastic process is called Rayleigh scattering (Fig. 3.5a). However, if the excited electrons involve the vibrations of atoms at their natural vibration frequencies, the electrons scatter the photon energy back to another photon with either lower or higher energy than incident photon by the vibration energy. This inelastic scattering process with creation or annihilation of a phonon is called Raman scattering (Fig. 3.5b). When the photon loses energy by creating a phonon, this is called a Stokes process, while when it gains energy by absorbing a phonon, it is called an anti-Stokes process [89].

In the Raman process, the incident and scattered photons have different

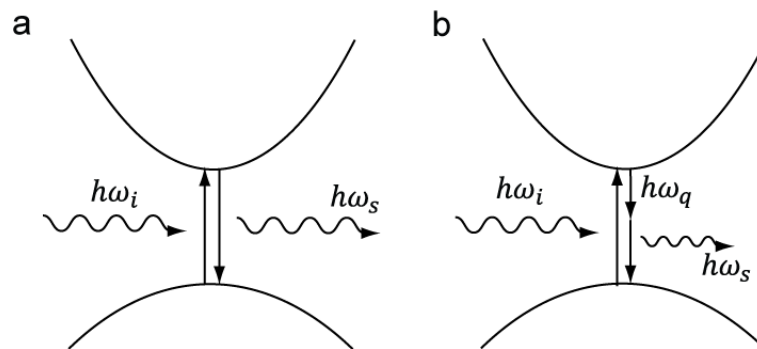


Figure 3.5: Rayleigh and Raman scattering in electronic states. (a) In the Rayleigh scattering process, incident light with an energy $h\omega_i$ is elastically scattered by electrons, emitting light with an energy $h\omega_s = h\omega_i$. (b) In the Raman scattering process, the incident light creates a phonon with energy $h\omega_q$, is, thus, inelastically scattered, resulting in light with an energy $h\omega_s = h\omega_i - h\omega_q$.

frequencies by the frequency of the phonon normal mode; $h\omega_s - h\omega_i = h\omega_q$, where $h\omega_s$ and $h\omega_i$, are the energies of scattered and incident photons and $h\omega_q$ is the energy of the phonon normal mode. Since the normal mode is uniquely related to chemical and physical structures of a material, one can probe the chemical and physical properties by measuring the energy difference $h\omega_q = h\omega_i - h\omega_s$. The Raman spectrum plots the scattered intensity as a function of $h\omega_q$ in units of cm^{-1} , exhibiting peaks at Raman active modes of a material (1 cm^{-1} corresponds to approximately 0.124 meV).

In this research, I mainly used an H-J-Y Raman microscope with excitation laser wavelengths 532 and 633 nm.

Chapter 4: Raman spectroscopy of graphene and MoS₂

As described in the previous chapter, Raman spectroscopy is a technique to characterize non-destructively chemical and physical properties of a material through light-matter interaction. In this chapter, I highlight prominent Raman features of graphene and MoS₂ and show how they can be used to determine their thickness or to estimate the density of defects and the carrier density in single-layer crystals.

4.1 Main Raman features of graphene

Figure 4.1 shows the Raman spectrum of graphene with defects. Pristine graphene shows two marked Raman features; the G band at $\sim 1580\text{ cm}^{-1}$ and the G' band at $\sim 2700\text{ cm}^{-1}$ [89]. Additionally, when defects are present in graphene, a mode appears at $\sim 1350\text{ cm}^{-1}$ as shown in Fig. 4.1, which is called the D band after “defects” or “disorder” [89]. The G band is the first order Raman mode associated with in-plane C-C bond stretching (Fig. 4.2a), which creates the doubly degenerate

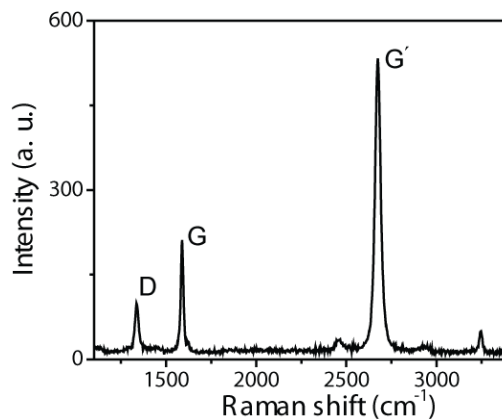


Figure 4.1: The Raman spectrum of graphene with defects. The excitation energy is 1.9 eV.

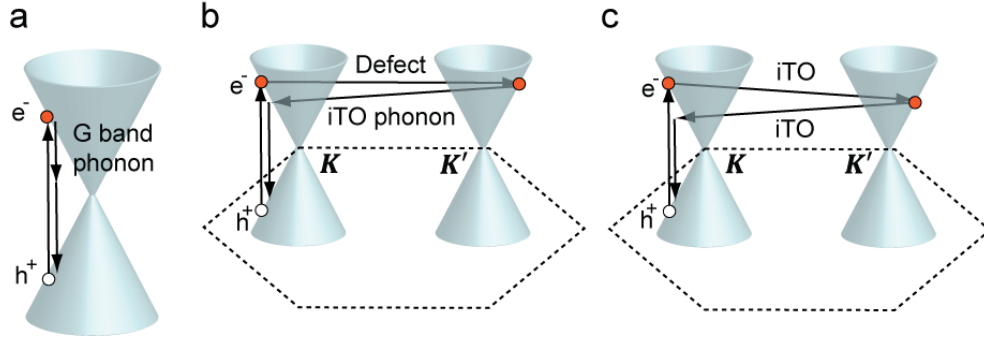


Figure 4.2: The Raman G, D, and G' modes of graphene. (a) The G band is the first order process. (b) The D band is the second-order process, which involves the defect scattering and phonon emitting. (c) The G' band is the second-order process, involving two phonons.

in-plane transverse optical (iTO) and longitudinal optical (LO) phonons at the Γ point [90]. In contrast, the G' and D bands are the second-order processes [90]. In the double resonance process of the D band, the photo-excited electrons at a K point are first elastically scattered by a defect to a K' point (Fig. 4.2b). Then, the scattered electrons are inelastically scattered back to the K point by emitting an iTO phonon by electron-hole recombination (Fig. 4.2b) [90]. For the G' band, the photo-excited electrons are inelastically scattered by an iTO phonon and are scattered back by an iTO phonon (Fig. 4.2c).

Figure 4.3a shows the Raman spectra of graphene for excitation energies of 1.9 eV (black line) and 2.3 eV (red line). Whereas the G band is insensitive to change in the excitation energy, the D and G' bands upshift with increasing laser energy. In Fig. 4.3b, the frequencies of the D and G' bands are plotted as functions of the excitation energy. The slopes are $\sim 50 \text{ cm}^{-1}/\text{eV}$ for the D band and $\sim 100 \text{ cm}^{-1}/\text{eV}$ for the G' band. These dispersive behaviors are due to the nature of the double resonance

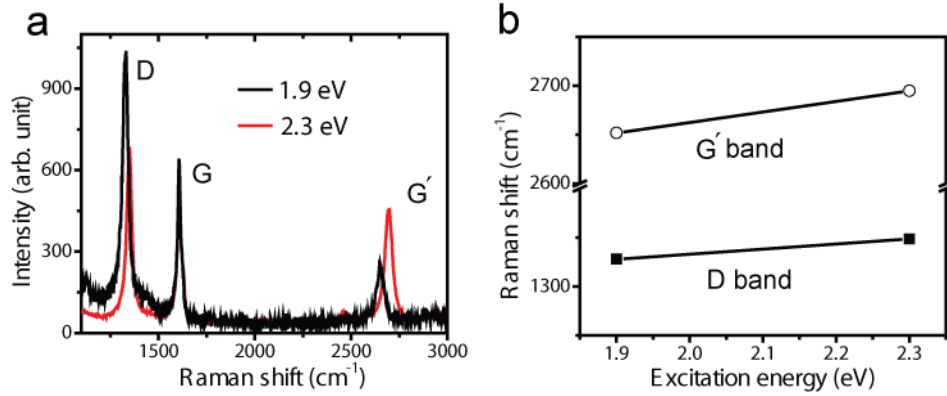


Figure 4.3: The dispersive behaviors of the D and G' modes. (a) The Raman spectra of graphene for excitation energies of 1.9 and 2.3 eV. (b) The frequencies of D and G' bands as functions of the excitation energy.

process, where phonons are coupled by the electronic states [90]. In the following sections, I highlight each Raman mode of graphene in more detail.

4.2 The dependence of the G' band on the thickness of graphene

As explained in the previous section, the G' mode shows dispersive behavior, depending on graphene's electronic structures. Since graphene shows markedly different electronic structures for different thicknesses, the G' band energy varies, depending on the number of layers of graphene. For example, bilayer graphene has two conduction bands and two valence bands, resulting in four double-resonance processes for the G' mode, as shown in Figs. 4.4a-d [91]. Thus, the G' band of bilayer graphene consists of the superposition of the four modes (2641, 2676, 2695, and 2710 cm^{-1}) as shown in Fig. 4.4e. Similarly, the G' band of trilayer graphene is calculated to consist of fifteen different modes [90].

Figure 4.5 shows the Raman G' bands of single-, bi-, tri-, 4-, and 5-layer graphene. The shape of the peak is significantly different for different number of

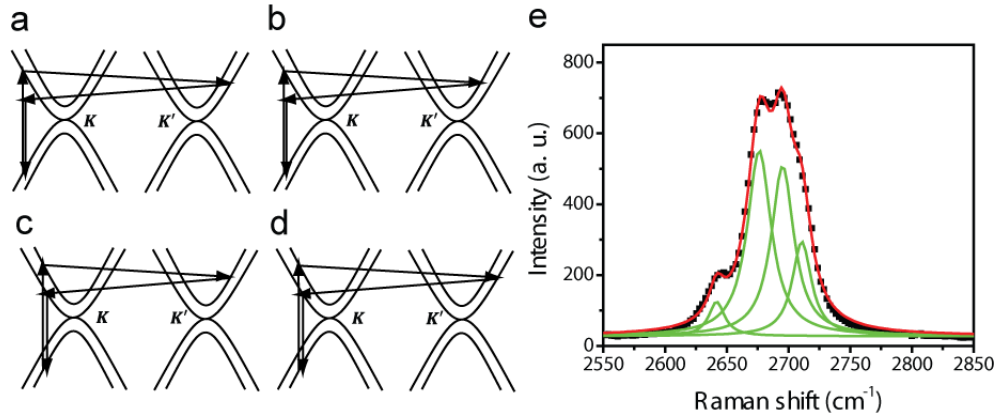


Figure 4.4: The G' band of bilayer graphene. (a)-(d) Four different resonance processes. (e) The G' band of bilayer graphene. The black dots are experimental results. The green curves are multi-peak fits of the experimental results. The red curve is fit obtained by the superposition of the four curves. The excitation energy is 2.3 eV.

graphene layers. Thus, together with the optical contrast of graphene supported on a substrate, the G' band can uniquely determine the thickness of graphene.

Additionally, the Raman G' band can be also used to identify the stacking order in few-layer graphene [89]. The stacking is an important degree of freedom of graphene, which directly determines its electronic structures. For example, Bernal- (ABA-) stacked trilayer graphene is semimetallic, while rhombohedral- (ABC-) stacked trilayer graphene is semiconducting [92-94]. Distinguishing the stacking order is, thus, essential. Recent Raman spectroscopy studies have demonstrated the identification of the stacking order in few-layer graphene using the Raman G' band and have revealed that a proportion of mechanically exfoliated few-layer graphene has rhombohedral stacking rather than energetically-favorable Bernal stacking [95, 96].

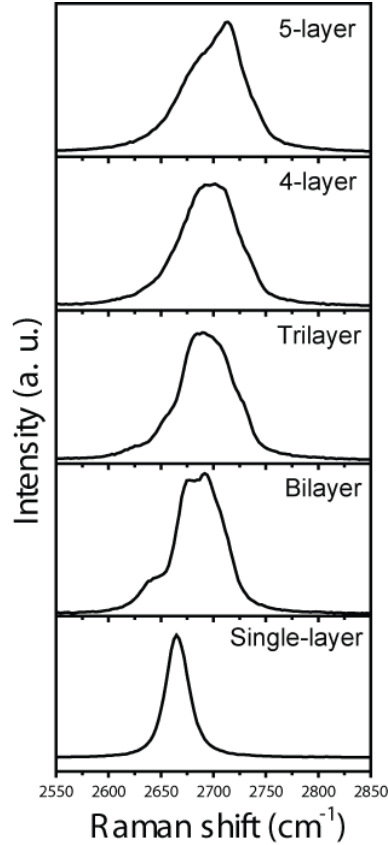


Figure 4.5: The G' band of single- and few-layer graphene. From the bottom to the top, single-layer, bilayer, trilayer, 4-layer, and 5-layer graphene.

4.3 Effect of doping on the Raman G mode

In a metal, atomic vibrations are partially screened by the conduction electrons. The screening changes rapidly for phonons with a wave vector \mathbf{q} such that $\mathbf{q} \sim 2\mathbf{k}_F$ (\mathbf{k}_F is a Fermi wavevector) and softens of the phonons. This anomalous behavior of the phonon dispersion is called the Kohn anomaly [97]. In graphene, the Kohn anomaly occurs for $\mathbf{q} = \Gamma$ and $\mathbf{q} = \mathbf{K}$ (see Fig. 2.1), where the phonons for the Γ and \mathbf{K} points are associated with the Raman G and G' bands, respectively. When graphene is doped and, hence, the Fermi surface changes, the Kohn anomaly is induced away from $\mathbf{q} = \mathbf{0}$, resulting in the stiffening of the Raman G band [98]. The

effect of doping on the Raman G band has been investigated through in-situ Raman spectroscopy of graphene with tunable carrier density *via* gate voltage [99-101]. The Raman G band energy is observed to increase linearly with increasing carrier density due to the electron-phonon coupling. The shift in frequency is symmetric relative to the Dirac point due to the particle-hole symmetry of graphene's electronic structure. The experimental results provide phenomenological relation between the frequency shift of the Raman G band and the doping level in single-layer graphene.

4.4 Determining the defect density in graphene through the Raman D mode

As explained in Section 4.1, when defects or disorder are introduced in graphene, the Raman D peak appears at $\sim 1350 \text{ cm}^{-1}$. In a simple picture, the intensity of the D band I_D is proportional to the total number of defects on the area illuminated by the laser; $I_D \propto (L_L / L_D)^2$, where L_D is a characteristic length between neighboring defects and L_L is the laser spot size. The G band intensity I_G is proportional to the total area probed by the laser, $I_G \propto L_L^2$. Therefore, the intensity ratio I_D / I_G is proportional to the density of defects $I_D / I_G \propto 1 / L_D^2$. This simple relation agrees well with the observations for low-defect density regime ($L_D \geq 10 \text{ nm}$) [102, 103]. Thus, using experimentally determined constant for $I_D / I_G \propto 1 / L_D^2$ and considering the dispersive behavior of the Raman D peak, the density of defects in graphene n_D can be determined as a function of I_D / I_G as follows;

$$n_D = \frac{(1.8 \pm 0.5) \times 10^{22}}{\lambda_L^4} \left(\frac{I_D}{I_G} \right), \quad (4.1)$$

where λ_L is the wavelength of excitation laser and the defect density is in units of cm^{-2} [103].

4.5 The Raman E_{2g}^1 and A_{1g} modes of MoS_2

In this section, I review the main Raman features of MoS_2 and introduce how these modes can be used to determine the MoS_2 thickness and they are influenced by doping. MoS_2 shows two prominent Raman features; the in-plane E_{2g}^1 mode at $\sim 385 \text{ cm}^{-1}$ (Fig. 4.6a) and the out-of-plane A_{1g} mode at $\sim 405 \text{ cm}^{-1}$ (Fig. 4.6b). These two modes are sensitive to the number of MoS_2 layers as shown in Fig. 4.6c. The A_{1g} mode upshifts, while the E_{2g}^1 mode downshifts with increasing thickness, as shown in Fig. 4.6d. The frequencies of the modes reach those of bulk MoS_2 at \sim six layers

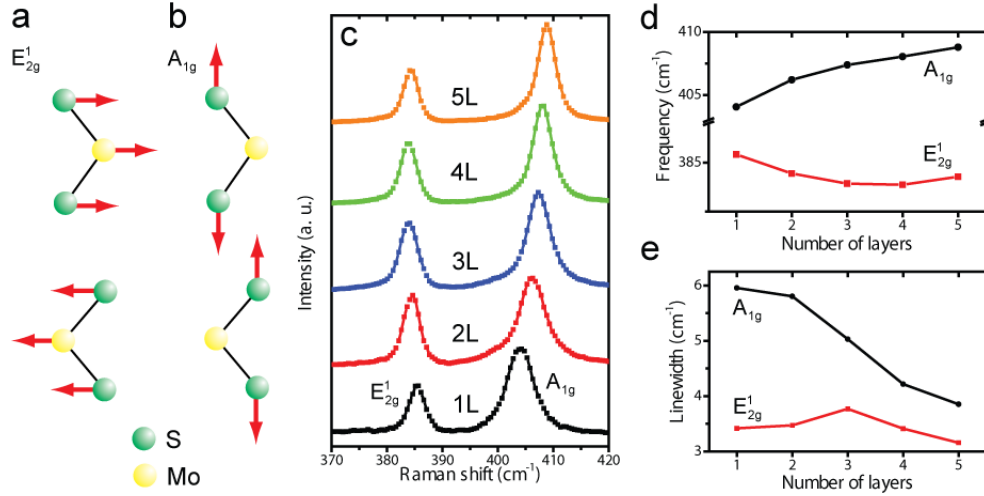


Figure 4.6: The Raman spectra of atomically thin MoS_2 . (a) and (b) Vibrations of S and Mo atoms for the E_{2g}^1 and A_{1g} modes. (c) Raman spectra of single- (1L-), bi- (2L-), tri- (3L-), four- (4L-), and five- (5L-) layer MoS_2 . (d) The frequencies of the E_{2g}^1 and A_{1g} modes as functions of the number of layers. (e) The linewidths of the E_{2g}^1 and A_{1g} modes as functions of the number of layers.

[104]. The stiffening of the A_{1g} mode with thickness can be explained qualitatively by the effect of the interlayer van der Waals attractions. However, the anomalous softening of the E_{2g}^1 mode may be due to long-range Coulomb interlayer interactions [104]. Figure 4.6e shows the linewidths of the E_{2g}^1 and A_{1g} modes as functions of the number of layers. The linewidth of the A_{1g} mode decreases with increasing thickness, while that of E_{2g}^1 is nearly independent of thickness. Thus, the frequencies of the Raman E_{2g}^1 and A_{1g} modes, along with the linewidth of the A_{1g} mode, can be used to determine the thickness of atomically thin MoS_2 .

Next, I discuss the effect of doping on the Raman modes of MoS_2 . Previous Raman measurement of single-layer MoS_2 using electrolyte gating, combined with the density functional theory calculations, have revealed that the Raman A_{1g} mode downshifts and its linewidth increases with increasing electron density due to electron-phonon interactions [105]. The results relate the carrier concentrations n in single-layer MoS_2 to the change in the frequency of the A_{1g} mode $\Delta\omega$ (in cm^{-1}) by $n = -4.5 \times \Delta\omega \cdot 10^{12} \text{ cm}^{-2}$. Thus, the A_{1g} mode can be used to estimate dopant concentrations in MoS_2 . In contrast, the E_{2g}^1 phonon is insensitive to carrier density in MoS_2 .

Chapter 5: Morphological transitions of graphene on nano-patterned substrates^{*}

A first step toward strain-engineering is to regulate the morphology of graphene. The most feasible approach to control of graphene's morphology is to use a patterned substrate. Graphene tends to adhere to an underlying substrate due to van der Waals interaction; hence, the substrate features largely determine graphene's morphology. However, graphene's elasticity is expected to act to hinder it from deforming because the mechanical deformation is energetically unfavorable, restricting the structure of graphene on a substrate.

In this chapter, I explore the extent to which graphene's morphology can be controlled through graphene-substrate adhesion. I use support substrates of varying roughness to probe the morphological response of graphene to substrate features and show that graphene's morphology evolves from adhered to wrinkled to delaminated geometries with increasing magnitude of roughness or graphene thickness. The morphological transitions are described within a continuum elastic model and by statistical physical approaches. The findings, together with the theoretical models, offer an effective strategy to manipulate the strain of graphene *via* adhesion to patterned substrates.

^{*} Adapted from “‘The Princess and the Pea’ at the nanoscale: Wrinkling and delamination of graphene on nanoparticles” by Mahito Yamamoto, Olivier Pierre-Louis, Jia Huang, Michael S Fuhrer, Theodore L. Einstein, and William G. Cullen (*Physical Review X*, **2**, 041018, 2012)

5.1 Morphology of graphene on substrates

The morphology of graphene on a substrate is governed by two competing effects: graphene-substrate adhesion and graphene's elasticity. Since graphene is an exceptionally flexible material with a bending rigidity $\kappa \approx 1$ eV [106], it can adhere conformally to substrates ranging from atomically flat mica [107] and BN [108, 109] to nanoscopically rough SiO₂ [35, 36, 110]. However, graphene also shows extraordinary in-plane stiffness, with a tensile rigidity $E_{2D} \approx 2.12 \times 10^3$ eV/nm² [7], leading to an effective mechanical thickness $t_{\text{eff}} = (12\kappa/E_{2D})^{1/2}$ of less than 1 Å [111]. Therefore, graphene is expected to undergo a transition from conformal to relaxed morphologies under stress on a substrate [112-115]. Indeed, graphene on a PMMA surface shows wrinkling under compressive stress induced by thermal cycling [116]. Additionally, graphene is observed to delaminate from uniaxially periodically corrugated surfaces with increasing graphene thickness [117, 118]. However, morphological behaviors of graphene on nano-patterned substrates have yet to be fully understood. In this chapter, we investigate systematically the morphological responses of graphene membranes to nanoscale rough features of substrates.

5.2 Experimental details

Rough substrates are prepared by placing SiO₂ nanoparticles randomly onto SiO₂ substrates. SiO₂-nanoparticle colloidal dispersions (Nissan Chemical America Corp., Snowtex-O) are diluted to various concentrations of 0.5–3.0 wt% by deionized water (Fisher Scientific, Water HPLC Grade). The diluted suspensions are sonicated for 30 min in a water bath to break agglomerations before spin coating the nanoparticles onto a substrate. Spin coating is performed on Si substrates with a 300-

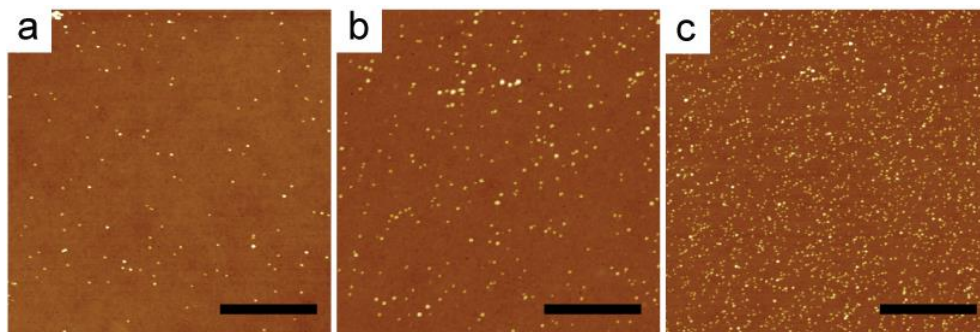


Figure 5.1: AFM images of SiO₂-nanoparticle-decorated SiO₂ substrates. The density of nanoparticles are (a) 6, (b) 36, and (c) 91 μm^{-2} . The scale bars are 3 μm . nm-thick oxide layer at 4000 rpm for 30 sec. The density of nanoparticles on substrates ranges from 2 to 258 μm^{-2} , depending on the concentrations of the nanoparticle dispersions (Fig. 5.1). After spin coating, the samples are completely dried on a hotplate at 150 °C for 2 h. The mean diameter of nanoparticles is 7.4 ± 2.2 nm as shown in Fig. 5.2.

Graphene flakes are mechanically exfoliated from Kish graphite onto SiO₂ substrates covered with the SiO₂ nanoparticles as described in Chapter 3. Thicknesses of graphene films are identified with an optical microscope, atomic force microscopy

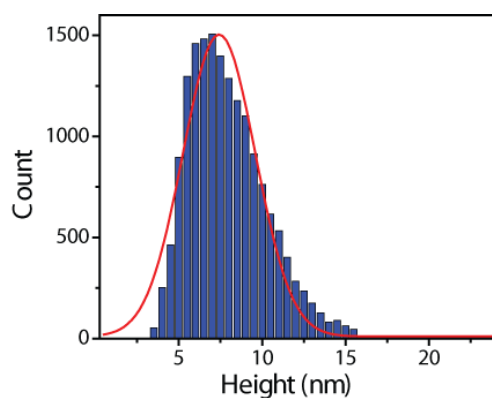


Figure 5.2: Height distribution of SiO₂ nanoparticles on SiO₂ substrates. The red curve is a Gaussian fit with a mean value of 7.4 ± 2.2 nm and a standard deviation of 4.8 nm^2 .

(AFM), and/or Raman spectroscopy (see Chapter 4 for details). The sizes of graphene sheets are typically more than $10\ \mu\text{m} \times 10\ \mu\text{m}$, which is much larger than an estimated distance between nanoparticles of approximately 700 nm at the smallest nanoparticle density of $2\ \mu\text{m}^{-2}$. Thus, we rule out the possibility of finite size effects in the following analyses. The samples are annealed at $500\ ^\circ\text{C}$ in vacuum for more than 5 h in order to remove any adhesive tape residue and to achieve equilibrium structures. After the annealing procedure, we observe surfaces of graphene membranes of various thicknesses in air using AFM in the tapping mode (see Chapter 3 for details).

5.3 Experimental results

Figure 5.3 shows typical AFM images of single-layer graphene supported on

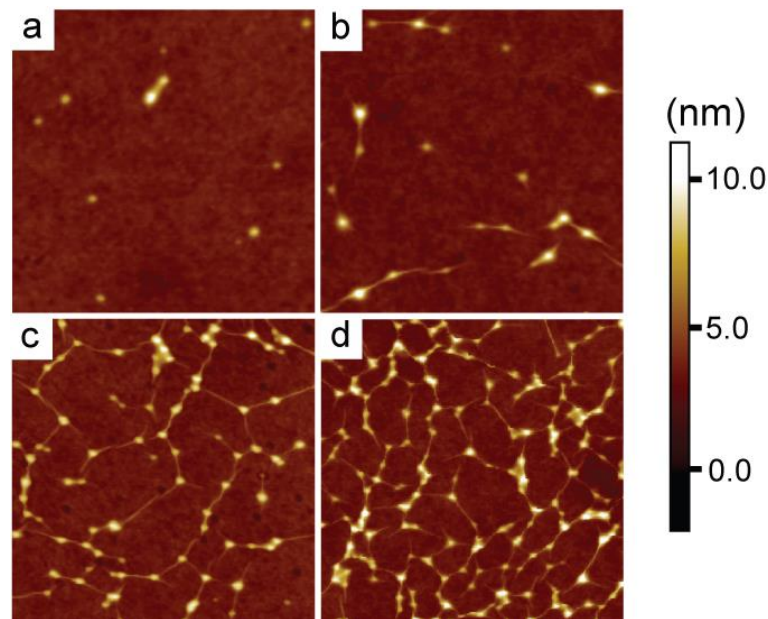


Figure 5.3: AFM images of single-layer graphene on SiO₂ nanoparticles/SiO₂ substrates for various nanoparticle densities. The nanoparticle densities are (a) 11 (b) 22 (c) 49, and (d) 170 μm^{-2} . The image sizes are $1\ \mu\text{m} \times 1\ \mu\text{m}$.

nanoparticles for various densities ρ_{np} . At $\rho_{\text{np}} = 11 \mu\text{m}^{-2}$ (Fig. 5.3a), graphene adheres conformally to the substrate, as noted previously [35, 36, 107-110], with predominantly isolated protrusions at the nanoparticle locations. At $\rho_{\text{np}} = 22 \mu\text{m}^{-2}$ (Fig. 5.3b), some nanoparticle-induced protrusions are linked by wrinkles. Additional wrinkles with one free termination are also observed. With a further increase in nanoparticle density, the wrinkles connecting the protrusions proliferate (Fig. 5.3c), and ultimately a wrinkle network spans the sample (Fig. 5.3d).

Next, we investigate morphology of graphene supported on nanoparticles as a function of graphene thickness. Figure 5.4 shows typical AFM images of single- and multi-layer graphene supported on nanoparticles of density $\rho_{\text{np}} = 160 \pm 24 \mu\text{m}^{-2}$. In Fig. 5.4a, wrinkles are formed in single-layer graphene. With increasing thickness,

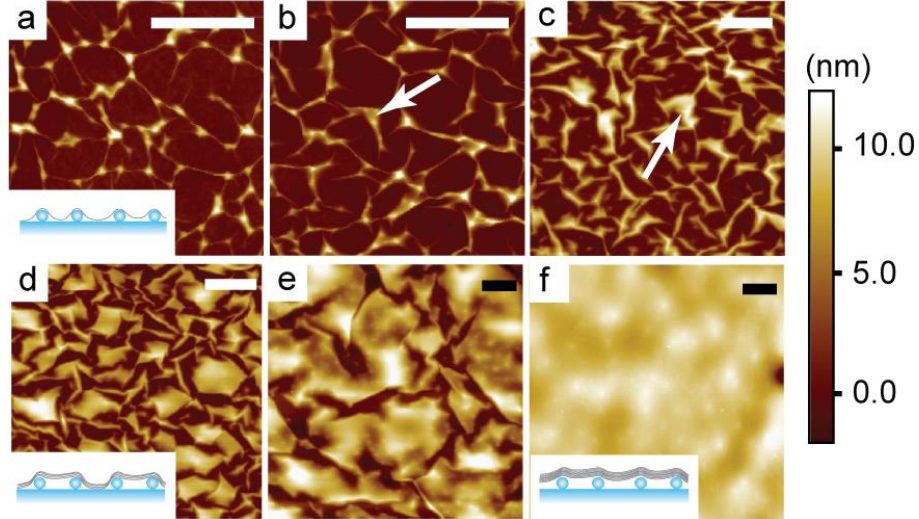


Figure 5.4: AFM images of graphene layers on SiO_2 with nanoparticles of the density of $160 \pm 24 \mu\text{m}^{-2}$. (a) Single-, (b) tri-, (c) 7-, (d) 10-, (e) 14-, and (f) 18-layer graphene. The scale bar in each image is 400 nm. The insets in (a), (d), and (f) are corresponding schematics of graphene supported on nanoparticles to the AFM images.

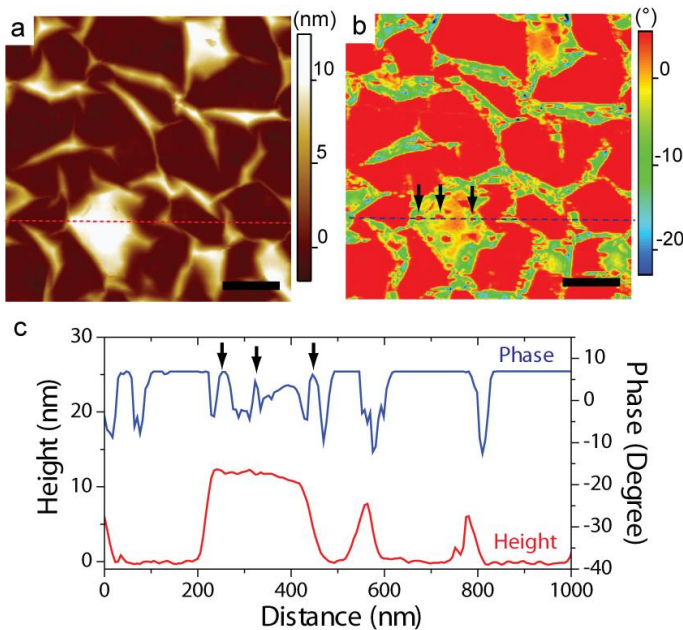


Figure 5.5: AFM height and phase images of a delaminated graphene multilayer on nanoparticles. (a) Height and (b) phase images ($1 \times 1 \mu\text{m}^2$) of 4-layer graphene delaminated from the nanoparticle-decorated substrate. The scale bars are 200 nm. (c) Line profiles of the height and phase along the dashed red and blue lines shown in (a) and (b), respectively. The arrows correspond to those in (b), showing the locations of nanoparticles beneath graphene.

graphene is partially suspended over regions where the nanoparticles are dense, as indicated by arrows in Figs. 5.4b and c. The delaminated areas increase with further increase in the number of graphene layers (Figs. 5.4d and e), and, ultimately, graphene is completely delaminated from the substrate for 18-layers (Fig. 5.4f). The insets in Figs. 5.4a, d and e depict schematically the wrinkling, the partial delamination, and the global delamination of graphene.

We confirm that graphene is indeed suspended over isolated nanoparticles by using AFM phase imaging (Fig. 5.5). The phase image records the varying phase angle of the (oscillating) AFM cantilever as it interacts with an inhomogeneous

sample surface. The phase angle increases with increasing local sample stiffness [120], allowing detection of the hidden nanoparticles under the flat graphene membrane. Figure 5.5b is an AFM phase image of graphene suspended over nanoparticles (Fig. 5.5a is a corresponding height image). The phase image of 4-layer graphene discriminates between rigid supported regions (larger phase) and flexible suspended regions (smaller phase). The high, flat regions in the topography show small, roughly circular regions of a large phase, indicating the locations of the nanoparticles (arrows) that support the surrounding suspended graphene (small phase). Figure 5.5c shows profiles along the dashed lines in the AFM images in Figs. 5.5a and b, clearly demonstrating the positions of the nanoparticles as indicated by arrows.

We found that graphene membranes supported on nanoparticle-decorated substrates show structural transitions from conformal to wrinkled to delaminated geometries with increasing nanoparticle density or graphene thickness. Below, I present detailed analyses of the critical behaviors of graphene morphology within an elastic model and by using statistical approaches.

5.4 Elastic analyses of structural transitions of graphene

5.4.1 Wrinkling of single-layer graphene

Our observations indicate the presence of a critical distance X_c between nanoparticles, below which wrinkling is induced. In this section, we analyze the critical nanoparticle separation X_c within a continuum elastic model, allowing for the graphene-substrate adhesion. The ridge running along the wrinkle between two nanoparticles of diameters d separated by X follows a catenary-like profile with a deflection ζ_0 in the middle as shown in Fig. 5.6 (see also Fig. 5.7a). Additionally, as

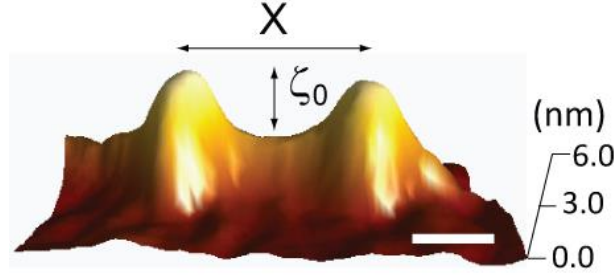


Figure 5.6: An AFM image of a wrinkle formed between two nanoparticles. The spacing between the nanoparticles is X and the deflection in the middle is ζ_0 . The scale bar is 20 nm.

represented in Fig. 5.7b, the profile of the ridge along the transverse (y -) direction can be characterized with the dihedral angle θ and the curvature radius $C_0(x)^{-1}$. The contour of the wrinkle results from the balance between elasticity and adhesion. Assuming that the opening angle θ is independent of x as validated in Ref. [121], the width of the deformed region and the deflection can be expressed by $w(x) = (\pi - \theta) C_0(x)^{-1}$ and $\zeta(x) = [1/\sin(\theta/2) - 1] C_0(x)^{-1}$, respectively, within the effective one-dimensional model. Furthermore, the stretching strain in the y -direction is irrelevant according to Ref. [121]. Then, the stretching strain is also given in one dimension (in the x -direction) by $\varepsilon_x = [1 + (\partial_x \zeta)^2]^{1/2} - 1 \approx (\partial_x \zeta)^2 / 2$. We find the stretching energy E_s and the bending energy E_b ;

$$\begin{aligned}
 E_s &= \frac{E_{2D}}{2} \int dx w(x) \varepsilon_x^2 \\
 &= \frac{E_{2D}}{2} (\pi - \theta) \left[\frac{1}{\sin(\theta/2)} - 1 \right]^{-1} \int dx \zeta (\partial_x \zeta)^4,
 \end{aligned} \tag{5.1}$$

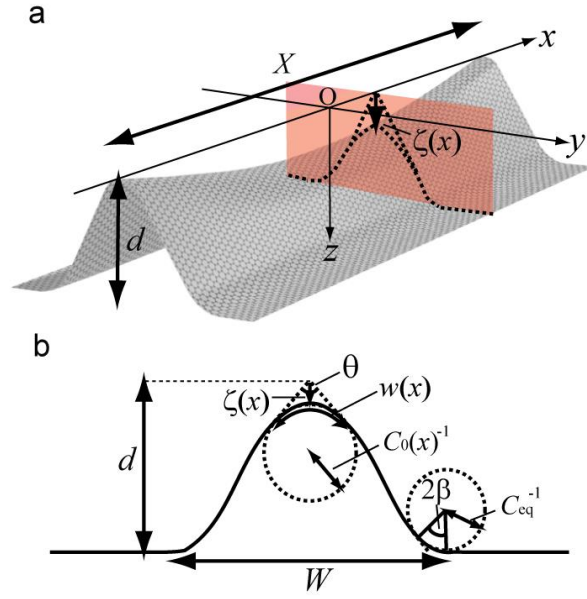


Figure 5.7: Schematics of a wrinkle. (a) A wrinkle is formed between two nanoparticles with diameter d . (b) The wrinkle profile along the transverse direction as represented by shaded area in (a).

$$\begin{aligned}
 E_b &= \frac{\kappa}{2} \int dx w(x) C_0(x)^2 \\
 &= \frac{\kappa}{2} (\pi - \theta) \left[\frac{1}{\sin(\theta/2)} - 1 \right] \int dx \zeta^{-1}.
 \end{aligned} \tag{5.2}$$

The adhesion energy cost is proportional to the area of the substrate uncovered by graphene:

$$E_\Gamma = \Gamma \int dx W = 2\Gamma X d \tan(\theta/2), \tag{5.3}$$

where Γ is the graphene-SiO₂ adhesion energy per area and W is the base of the wrinkle profile as illustrated in Fig. 5.7b. In addition, bending and adhesion at the foot of the wrinkle cost bending energy E_b and adhesion energy E_Γ :

$$E_b = 2 \frac{\kappa}{2} \int dx \int dy C_{eq}^2 = X \left(\frac{\Gamma \kappa}{2} \right)^{1/2} (\pi - \theta), \tag{5.4}$$

$$E_{\Gamma} = 2\Gamma X C_{\text{eq}}^{-1} \tan \beta = X (2\Gamma \kappa)^{1/2} \tan\left(\frac{\pi - \theta}{4}\right), \quad (5.5)$$

where 2β and C_{eq} are the angle and the curvature of the curved region as shown in Fig. 5.7b.

At equilibrium, $\delta E_{\text{tot}}/\delta \zeta = 0$, where $E_{\text{tot}} = E_s + E_b + E_{\Gamma} + E_b + E_{\Gamma}$, leading to

a differential equation for deflection ζ :

$$\zeta^2 \left[3(\partial_x \zeta)^4 + 12\zeta (\partial_x \zeta)^2 \partial_{xx} \zeta \right] + \frac{4\kappa}{E_{2D}} \left[\frac{1}{\sin(\theta/2)} - 1 \right]^2 = 0 \quad (5.6)$$

with the two boundary conditions $\zeta(\pm X/2) = 0$. We anticipate ζ to be symmetric with respect to x , so that $\partial_x \zeta$ should vanish at $x = 0$. However, Eq.(5.6) indicates that if $\partial_x \zeta$ vanishes at $x = 0$, either ζ or $\partial_{xx} \zeta$ should diverge. Since the solution with

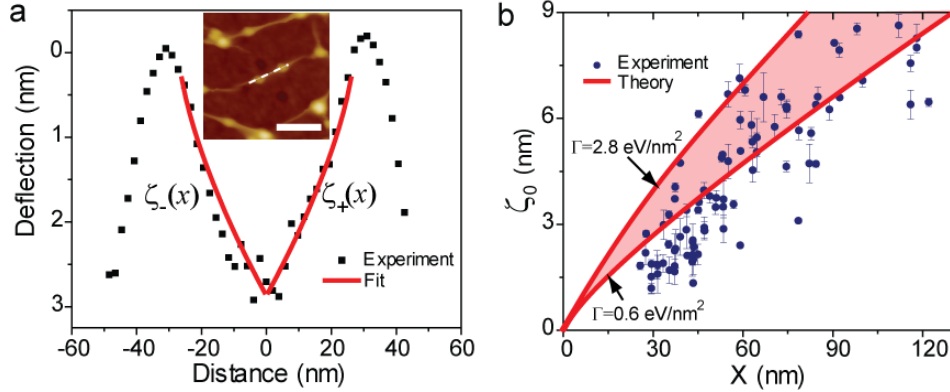


Figure 5.8: The deflection of a wrinkle. (a) A profile of the wrinkle along the white dotted line in the AFM image shown in the inset. The scale bar in the inset is 50 nm. The solid red lines are theoretical expectations. (b) The maximum deflection ζ_0 as a function of the wrinkle length. The error bar indicates the uncertainty of ζ_0 due to the height difference between the protrusions. The area shaded in red is the theoretical prediction for the scaling of ζ_0 with $\Gamma = 0.6\text{-}2.8 \text{ eV/nm}^2$.

diverging ζ is physically inconceivable, $\partial_{xx}\zeta$ should diverge. This indicates a discontinuity of the slope at $x = 0$. Physically this singularity would be regularized at small scales either by bending along the x -direction or by stretching along the y -direction. These contributions are expected to be small. As a result, we obtain a simple solution for the deflection on both sides of the center of the wrinkle:

$$\zeta_{\pm}(x) = \left(\frac{27\kappa}{4E_{2D}} \right)^{1/6} \left[\frac{1}{\sin(\theta/2)} - 1 \right]^{1/3} \left(\frac{X}{2} \mp x \right)^{2/3}. \quad (5.7)$$

Figure 5.8a shows the line profile along a wrinkle formed between two protrusions. As shown by the red lines in Fig.5.8a, the observed deflection is well fitted by $\zeta_{\pm}(x) \sim (X/2 \mp x)^{2/3}$ with a prefactor of $0.32 \text{ nm}^{1/3}$. The opening angle θ can be related to X by minimizing numerically the total energy E_{tot} with respect to θ for a given X . Then, using the obtained relation between θ and X and Eq. (5.7), we find the maximum deflection $\zeta_0 \equiv \zeta(0)$ as shown in Fig. 5.8b. The maximum deflection ζ_0 monotonically increases with X , which is in good agreement with the observations (blue dots). Here, we used $d = 7.4 \pm 2.2 \text{ nm}$, $E_{2D} = 2.12 \times 10^3 \text{ eV/nm}^2$ [7], $\kappa = 1 \text{ eV}$ [106], and $\Gamma = 0.6\text{-}2.8 \text{ eV/nm}^2$ [35, 110, 122]. The theoretical model for a deflection is based on the assumption that a wrinkle is formed between two sharp peaks. The finite sizes of the nanoparticle-induced protrusions may be a cause of the decrease of the deflection below the theoretically expected range in Fig. 5.8b. Furthermore, we attribute the most likely source of uncertainty to the observed dispersion in nanoparticle sizes.

Since a wrinkle is geometrically suppressed if $\zeta(0) > d$, the maximum length of the wrinkle can be determined by a condition that $\zeta(0) = d$. From Eq. (5.7), we find

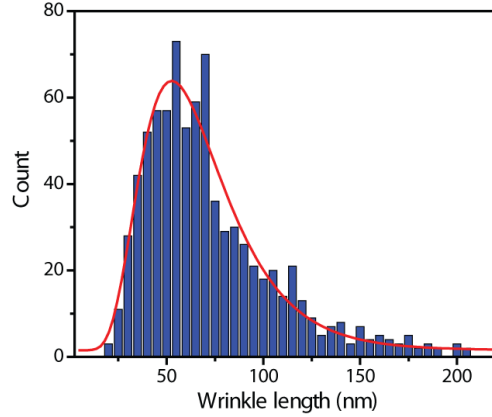


Figure 5.9: The distribution of lengths of the wrinkles. The density of nanoparticles ranges from 18 to $34 \mu\text{m}^{-2}$, where the wrinkles start forming. The red line is a log-normal fit as used for analyses of the distribution of the ridge lengths in a crumpled sheet of paper [123-125].

the maximum length $X_c = 104\text{-}65 \text{ nm}$ along with $\theta = 35^\circ\text{-}14^\circ$ for the adhesion energy $\Gamma = 0.6\text{-}2.8 \text{ eV/nm}^2$ [35, 110, 122], respectively, in rough agreement with the observed maximum wrinkle length of approximately 200 nm (Fig. 5.9). The discrepancy between the theoretical predictions and the observations is likely due to the fluctuations in the nanoparticle sizes d , which strongly influence the wrinkle length X_c (see Appendix A).

5.4.2 Delamination of graphene multilayers

In this section, we investigate morphological transitions which occur in multilayer graphene, shown in Fig. 5.4. Here, we use two quantities to characterize “conformity” of graphene to the substrate geometries; the areal fraction ϕ of graphene in contact with the substrate and the characteristic length l of the delaminated regions. Figure 5.10a shows a typical AFM image of 6-layer graphene delaminated partially from a substrate, where the contact areas are surrounded by orange dashed lines and a

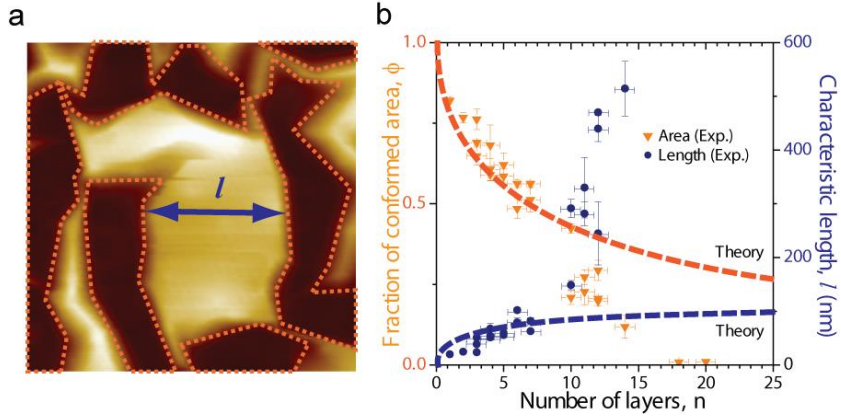


Figure 5.10: The conformed area and the characteristic length of delaminated graphene on nanoparticles. (a) An AFM image of 6-layer graphene on nanoparticles. The graphene film is in contact with the substrate in areas surrounded by orange dashed lines. The delaminated regions can be characterized with a length l . (b) The fractional area ϕ in contact with a substrate and the characteristic length l as functions of number of graphene layers n .

characteristic length is represented by a double arrow. In Fig. 5.10b, we show the fractional area ϕ and the characteristic length l as functions of number of graphene layers n . As n increases, a first transition occurs around $n = 10$, where l increases rapidly (see Fig. 5.4d, partial delamination); second, ϕ decreases and becomes negligibly small above $n = 15$ (see Fig. 5.4f, complete delamination).

Surface-roughness-induced delamination of graphene has been studied theoretically [112-115] and experimentally [118, 119, 126]. Models assume the elastic energy is dominated either by bending [112] or stretching [115]. Here we consider each regime, and assume that the adhesion energy between SiO_2 and n -layer graphene Γ_n is independent of n for $n > 1$ and has the value 1.9 eV/nm^2 [122]. In the bending-dominated model [112], delamination is controlled by a single dimensionless parameter $\alpha = (2\Gamma_n / \kappa_n)^{1/4} / [2\pi(\rho_{\text{np}}d)^{1/2}]$, where κ_n is the bending rigidity of n -layer

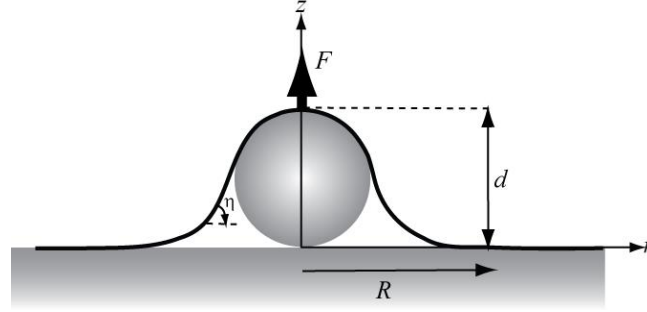


Figure 5.11: A schematic of graphene on a single nanoparticle. The diameter of the nanoparticle is d . The detachment length is R . The graphene membrane is pushed by the nanoparticle by a force F . The angle of the rotation is η .

graphene for $n > 1$. Without interlayer sliding [127], continuum plate elasticity [53] gives $\kappa_n = Et^3 n^3 / [12(1 - \nu_g^2)]$, where $t = 0.335$ nm is the interlayer spacing, $E \approx 0.96$ TPa is Young's modulus, and $\nu_g \approx 0.165$ is Poisson's ratio of single-layer graphene [7]. The threshold for partial delamination is predicted at $0.8 \leq \alpha \leq 1.3$, or $3 \leq n \leq 6$, with complete delamination at $0.55 \leq \alpha \leq 0.75$, corresponding to $7 \leq n \leq 10$ [112]. Thus, the bending-dominated model underestimates the critical value of n for delamination. The one-dimensional character of the bending model limits its ability to make quantitative predictions. Furthermore, given the small radii of curvature in our experiment, the bending energy might well be reduced by partial interlayer sliding. Perfect sliding would give $\kappa_n = n\kappa$, leading to an delamination threshold for n a hundredfold larger; hence, interlayer sliding is extremely effective in relieving bending stress.

We then consider a stretching-dominated model as described below. The simplest model would be a power-law solution of Schwerin's equation for a membrane pushed by a point force [128]. However, in this model, the bending

rigidity only contributes as boundary-layer effects at the attachment lines [129]. Consequently, the Schwerin solution does not match tangentially to the substrate and the nanoparticle. Assuming that the nanoparticle diameter d is much smaller than the radius R of the detachment zone (see Fig. 5.11 for the definition), the angle of rotation and the vertical distance can be obtained from the substrate by using Schwerin's solution as $\eta(r) = [8F/(9\pi E_{2D}r)]^{1/3}$ and $Z = [3R^2 F/(\pi E_{2D})]^{1/3}$ [128, 129], where F is the force exerted at the apex. However, the above solution does not match the boundary conditions as noted above, and a better approximate numerical solution is $Z = g(\nu_g)(R^2 F/E_{2D})^{1/3}$, where $g(\nu_g) = 1.0491 - 0.1462\nu_g - 0.15827\nu_g^2$ [129]. For graphene, $\nu_g = 0.165$ and $g(\nu_g) \approx 1.029$ is very close to $(3/\pi) \approx 0.984$ so that we can use directly Schwerin's solution.

The elastic-stretching energy can be calculated from a gedanken experiment, where the height Z is increased with the constant R :

$$E(Z) = \int_0^Z dz F(z) = \frac{\pi E_{2D}}{3R^2} \int_0^Z dz z^3 = \frac{\pi E_{2D} Z^4}{12R^2}. \quad (5.8)$$

Assuming that the apex height is equal to the diameter d of the nanoparticle, we have $Z = d$, and the total energy reads

$$E(d) = \frac{\pi E_{2D} d^4}{12R^2} + \Gamma \pi R^2. \quad (5.9)$$

Minimizing the total energy with respect to R , we find $2R = d(4E_{2D}/3\Gamma)^{1/4}$ as suggested in Ref. [115].

Therefore, the diameter of the detachment zone in n -layer graphene around a protrusion is given by $2R \approx d(4nE_{2D}/3\Gamma_n)^{1/4}$, where nE_{2D} is the tensile rigidity of n -

layer graphene. The detached area around each protrusion is πR^2 , while the detached areas produced by the wrinkles are assumed to be negligible. Therefore, the typical length of the delaminated regions l is simply estimated to be $2R$. The adhered-area fraction is equivalent to the probability of having no nanoparticle in a domain of an area of πR^2 , leading to $\phi = \exp(-\pi R^2 \rho_{\text{np}})$. As shown in Fig. 5.10b, these predictions reproduce well the observed thickness dependence of ϕ and l below $n \approx 10$, indicating that the stretching-dominated model for isolated protrusions accurately describes the small- n limit where $\rho_{\text{np}} \ll l^2$. However, l increases and ϕ decreases much more rapidly than these predictions for $n > 10$, indicating that collective effects have become important. In order to understand the collective delamination in the high-nanoparticle-density regime $\rho_{\text{np}} > l^2$, we may need to solve full elastic membrane equations, i.e., the Föppl–von Kármán equations [53] allowing for multiple nanoparticles.

5.5 Pseudomagnetic fields in graphene on nanoparticles

Wrinkles and sharp points (i.e. conical singularities) are expected to affect markedly the electronic properties of graphene [130]. In this section, we discuss how inhomogeneous strain present in the protrusions and the wrinkles affects the electronic properties of graphene.

We first evaluate the pseudomagnetic field generated by strain gradients in the absence of wrinkling, corresponding to the case of small thickness or small nanoparticle density. In this case, the elastic behavior of graphene on nanoparticles is

predominantly determined by stretching, resulting in significant strain. At $0 < r < R$, the radial strain ε_r and the circumferential strain ε_φ are given by [129]:

$$\varepsilon_r = \frac{3 - \nu_g}{4} \left(\frac{4\Gamma}{9E_{2D}} \right)^{1/3} \left(\frac{d}{r} \right)^{2/3}, \quad (5.10)$$

$$\varepsilon_\varphi = \frac{1 - 3\nu_g}{4} \left(\frac{4\Gamma}{9E_{2D}} \right)^{1/3} \left(\frac{d}{r} \right)^{2/3}. \quad (5.11)$$

Under axisymmetric strain, the strain-induced gauge fields Eqs. (2.8)-(2.10) can be rewritten as

$$A_r \approx \frac{\Phi_0 \beta}{a} (\varepsilon_r - \varepsilon_\varphi) \cos 3\varphi, \quad (5.12)$$

$$A_\varphi \approx \frac{\Phi_0 \beta}{a} (\varepsilon_r - \varepsilon_\varphi) \sin 3\varphi, \quad (5.13)$$

where $\Phi_0 = 10^{-15}$ Wb is the flux quantum, $\beta \approx 2$ is the change in the hopping amplitude between the neighboring atomic sites due to the lattice deformation [51], $a = 0.142$ nm is the lattice constant, and φ is the azimuthal angle, with $\varphi = 0$ in the zigzag direction [55]. Then, the strain-induced pseudomagnetic field is given by

$$B_{\text{eff}} = \frac{1}{r} \frac{\partial A_r}{\partial \varphi} - \frac{\partial A_\varphi}{\partial r} - \frac{A_\varphi}{r}. \quad (5.14)$$

Thus, from Eqs. (5.10)-(5.14), the pseudomagnetic field in graphene supported on an isolated nanoparticle is given by

$$B_{\text{eff}} = -\frac{(1 + \nu_g) \Phi_0 \beta}{a} \left(\frac{500\Gamma d^2}{243E_{2D}} \right)^{1/3} r^{-5/3} \sin 3\varphi. \quad (5.15)$$

Figure 5.12 plots B_{eff} induced in a graphene protrusion formed on a nanoparticle with a diameter $d = 7.4$ nm. Here, $\Gamma = 2.8$ eV/nm², $E_{2D} = 2.12 \times 10^3$ eV/nm², $\nu_g = 0.165$. The origin corresponds to the apex of the protrusion, and the x -

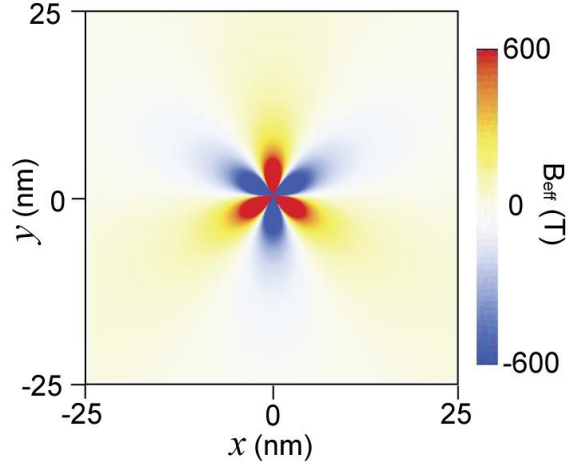


Figure 5.12: Strain-induced pseudomagnetic fields in graphene on an isolated nanoparticle. The diameter of the nanoparticle is 7.4 nm. The x -axis is in the zigzag direction.

axis is along the zigzag direction of graphene. As shown in Fig. 5.12, the strain in graphene induces threefold-symmetric pseudomagnetic field profiles with maximum fields along the armchair directions. The pseudomagnetic field pattern is similar to an experiment, in which suspended graphene was deformed by a sharp tip [56]. The predicted pseudomagnetic field exceeds 600 T near the apex of the protrusion, which is likely overestimated due to the divergence of theoretical strain near $r = 0$. The divergence is cut off by the finite radius of the nanoparticles; thus, the maximum pseudomagnetic field is expected to appear at a radius comparable to the nanoparticle radius. Therefore, the maximum pseudomagnetic field B_{eff} is estimated to be of order 300 T for $r = d/2$, which is significantly greater than the value in Ref. [56], suggesting that the impact on electronic properties may be even more profound.

Now we consider a trajectory of an electron subject to the strain-induced pseudomagnetic fields. The cyclotron radius r_c for Dirac fermion is given by

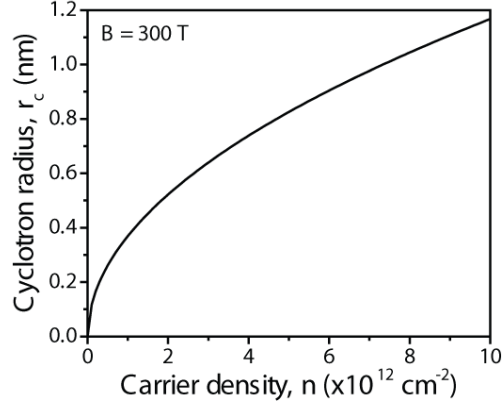


Figure 5.13: The cyclotron radius for Dirac fermion as a function of carrier density for $B = 300$ T.

$$r_c = \frac{\varepsilon_F}{ev_F B} = \frac{\hbar\sqrt{\pi n}}{eB}, \quad (5.16)$$

where $\varepsilon_F = \hbar v_F \sqrt{\pi n}$ is the Fermi energy with n being the carrier density, $v_F \approx 10^6$ m/s is the Fermi velocity, and B is the magnetic field [131]. In Fig. 5.13, we plot the cyclotron radius r_c as a function of n for $B = 300$ T. At a low carrier density, the cyclotron radius is of order 1 Å, which is much smaller than the width of the region in which pseudomagnetic fields exceed 300 T in the graphene protrusion (see Fig. 5.12). We further consider the magnetic length $l_B = \sqrt{\hbar/eB}$ which roughly corresponds to the radius of a state in the $n = 0$ Landau level (in the symmetric gauge) [21]. For $B = 300$ T, we find $l_B = 1.5$ nm. This is approximately the length scale over which the pseudomagnetic field is 300 T as shown in Fig. 5.12. The above analysis suggests that Landau quantization effects due to pseudomagnetic fields may be observable in our strained graphene structures. However, a detailed study of the electronic structure in such strongly inhomogeneous fields is necessary to fully understand the effects of strain on electronic properties.

Next, we evaluate strain and strain-induced pseudomagnetic fields in a wrinkle. Strain along a wrinkle is given by $\varepsilon_x \approx (\partial_x \zeta)^2$ and, thus, using Eq. (5.7), we find the strain distribution $\varepsilon_x \sim (\kappa/E_{2D})^{1/3} (X/2 \mp x)^{-2/3}$. The ridge direction (the x -direction in Fig. 5.7a) with respect to the lattice cannot be determined experimentally and, thus, an accurate analysis for the pseudomagnetic field in a wrinkle is hindered. However, the pseudomagnetic field in wrinkled graphene can be roughly estimated to be $B_{\text{eff}} \approx \Phi_0 \beta \varepsilon_x / (aW)$ [21, 115], where W is the typical wrinkle width as shown in Fig. 5.7b. In the strong adhesion limit $d(\Gamma/\kappa)^{1/2} \gg 1$, the wrinkle width W can be estimated to be $(\kappa/2\Gamma)^{1/2} \approx 1$ nm. Thus, in the middle of a wrinkle, the pseudomagnetic field has a broad minimum on the order of 10 T for $X = 100$ nm. 10 T is a large magnetic field compared to the disorder strength $1/\mu \sim 1$ T in typical graphene samples (μ being the electron mobility) and corresponds to an energy difference between zeroth and first Landau levels of approximately 1300 K. Hence, we expect pseudomagnetic-field effects due to wrinkles in graphene to be significant.

The pseudomagnetic field near nanoparticles in the wrinkled case will generally be more complicated, depending on the number of wrinkles terminating on the particle and their direction with respect to each other and the lattice. However, qualitatively we expect that since wrinkling reduces the in-plane strain around the nanoparticles, the pseudomagnetic field is also reduced. Recent results of molecular dynamics simulations [132] have indeed demonstrated that when nanoscale pillars supporting graphene are located far away from each other, graphene is detached only around the pillars and threefold-symmetric pseudomagnetic fields are induced around

each pillar. However, with decreasing distance between the pillars, graphene delaminates in regions between the pillars, resulting in complicated pseudomagnetic field profiles. The observations of wrinkling and delamination combined with a theoretical analysis based on a continuum-elastic model can be used to place limits on strain distributions and, thus, on pseudomagnetic field maxima attainable in single-layer graphene through adhesion to patterned surfaces.

5.6 Statistical mechanical analyses of graphene wrinkling

5.6.1 Random wrinkling model

In this section, we focus on statistical mechanical aspects of wrinkling of graphene on nanoparticles. Figure 5.14 shows the density of wrinkles ρ_w as a function of the nanoparticle density ρ_{np} and the number of wrinkles per protrusion ρ_w/ρ_{np} as a function of ρ_{np} (inset). The wrinkle density ρ_w is almost zero below $\rho_{np} \approx 25 \mu\text{m}^{-2}$ (arrow b) and then begins to increase rather linearly with ρ_{np} above $\rho_{np} \approx 50 \mu\text{m}^{-2}$

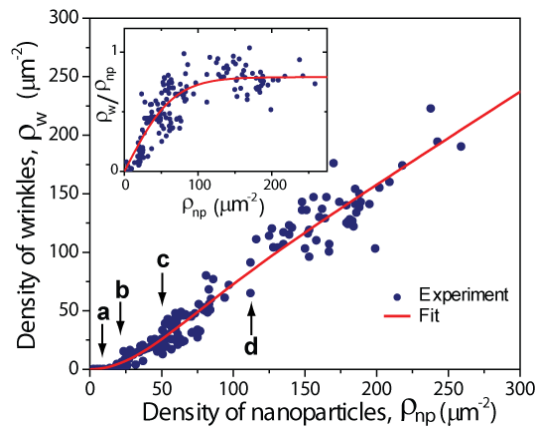


Figure 5.14: The density of wrinkles as a function of nanoparticle density. Each arrow corresponds to the AFM images shown in Fig. 5.3. The solid red lines are fits described in the text.

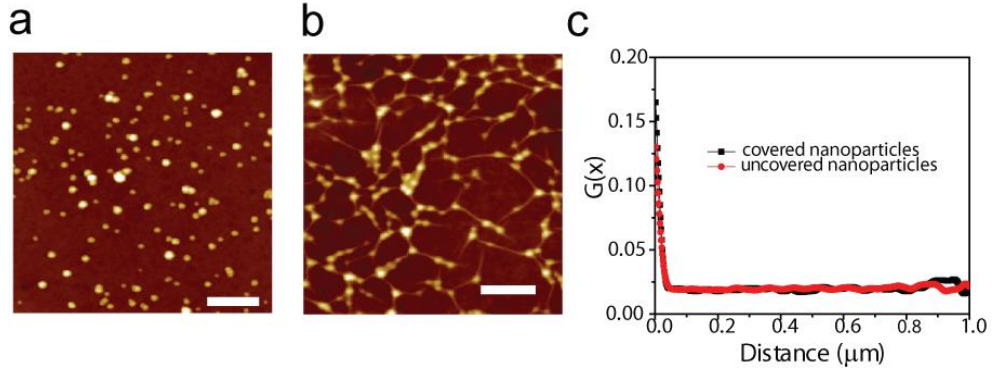


Figure 5.15: Particle-particle correlation functions of covered- and uncovered nanoparticles. (a-b) AFM images of (a) SiO₂ nanoparticles on SiO₂ and (b) graphene on SiO₂ nanoparticle-decorated SiO₂. (c) Particle-particle correlation functions for covered (black line) and uncovered (red line) nanoparticles.

(arrow c). We now analyze the behavior of the wrinkle density ρ_w versus the nanoparticle density ρ_{np} within a simple model.

First, we investigate whether nanoparticles are static or not upon graphene deposition by measuring particle-particle correlation functions for uncovered SiO₂ nanoparticles on SiO₂ and SiO₂ nanoparticles covered with graphene. Fig. 5.15c shows particle-particle correlation functions $G(x)$ defined as $G(x) = \langle z(x_0)z(x_0 + x) \rangle$, where $z(x) = 1$ if there is a nanoparticle at x_0 , and $z(x) = 0$ if not, for both uncovered and covered nanoparticles measured along a fast scan line in AFM images (see Figs. 5.15a and b). The density of nanoparticles is $160 \pm 24 \mu\text{m}^{-2}$, which corresponds to a mean spacing between neighboring nanoparticles of ~ 100 nm. We find no significant difference in the correlation functions between the covered and the uncovered nanoparticles around 100 nm, indicating the migration of the nanoparticles due to graphene is negligible.

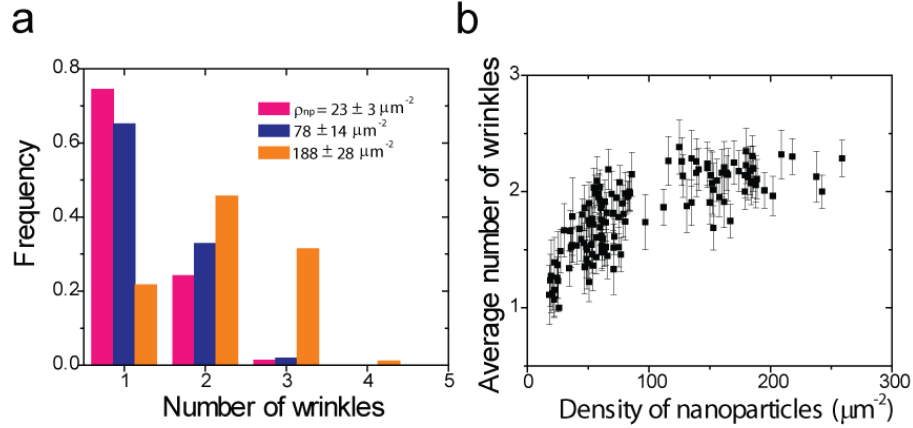


Figure 5.16: The number of wrinkles propagating from single nanoparticles. (a) The distribution of the number of wrinkles propagating from single nanoparticles for various nanoparticle densities. (b) The average number of wrinkles propagating from a single protrusion as a function of the density of nanoparticles.

We now consider a model in which nanoparticles are placed at random on the substrate beneath graphene. Then, graphene wrinkles are placed with a probability Ω_w between neighboring nanoparticles separated by less than a cutoff length X_c . With increasing nanoparticle density, the number of wrinkles propagating from single nanoparticles increases. However, as shown in Fig. 5.16, nanoparticles with more than three connected wrinkles are scarcely observed, even at a high nanoparticle density of more than $200 \mu\text{m}^{-2}$. Thus, we set three as the maximum number of wrinkles in our analysis. Employing the probability density $p_i(r)$ for a nanoparticle to have the i th nearest nanoparticle ($i=1, 2, \text{ and } 3$) at a distance r [133]

$$p_i(r) = \frac{2}{i!} (\pi \rho_{\text{np}})^{i+1} r^{2i+1} \exp(-\pi \rho_{\text{np}} r^2), \quad (5.17)$$

we find the density of wrinkles:

$$\begin{aligned}
\rho_w &= \frac{\rho_{np}\Omega_w}{2} \sum_{i=1}^3 \int_0^{X_c} dr p_i(r) \\
&= \frac{\rho_{np}\Omega_w}{2} \left[-\pi X_c^2 \rho_{np} \left(2 + \frac{1}{2} \pi X_c^2 \rho_{np} \right) e^{-\pi X_c^2 \rho_{np}} \right. \\
&\quad \left. + 3 \left(1 - e^{-\pi X_c^2 \rho_{np}} \right) \right] \tag{5.18}
\end{aligned}$$

The factor of 1/2 in ρ_w compensates for the double counting of each wrinkle (i.e., from the particles at each end). In the limit of small nanoparticle density $\rho_{np} \ll X_c^{-2}$, the density of wrinkles is $\rho_w = (1/2)\Omega_w \pi X_c^2 \rho_{np}^2$, while in the large-density limit $\rho_{np} \gg X_c^{-2}$, each nanoparticle has at least three neighboring nanoparticles within distance X_c , leading to $\rho_w = (3/2) \Omega_w \rho_{np}$. The red solid lines in Fig. 5.14 are fits to Eq. (5.18) with $\Omega_w = 0.54$ and $X_c = 120$ nm. The cutoff length is consistent with the observations (Fig. 5.9). Furthermore, the agreement with X_c predicted from the elastic analysis in Section 5.4.1 is good. The model indicates a significant increase of the wrinkle density for the nanoparticle density larger than $(\pi X_c)^{-2}$, but also suggests that ρ_w does not exhibit any singularity; i.e., wrinkling is a crossover phenomenon rather than a sharp transition.

5.6.2 Percolation transition in the wrinkle network

With increasing ρ_{np} , the connectivity of the wrinkle network increases, and we find a percolation transition at a threshold density ρ_c (of order X_c^{-2}) at which the wrinkle network spans the system (Fig. 5.17). The expansion of the network *via* wrinkling is a purely two-dimensional (2D) phenomenon. Thus, we analyze this behavior using a 2D percolation theory [134].

In Fig. 5.18a, we plot the probability P that a given protrusion belongs to the percolating cluster spanning a region of size $L \times L$, where L ranges from 1 to 3 μm .

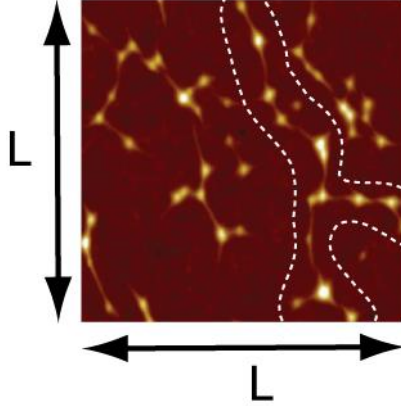


Figure 5.17: Percolation transition in the wrinkle network. An AFM image ($L \times L$ with $L = 1 \mu\text{m}$) of wrinkled graphene with a percolating cluster, which is represented by the dashed line.

Also plotted is the prediction from 2D percolation theory: $P \sim (\rho_{\text{np}} - \rho_c)^\beta$ for $\rho_{\text{np}} \geq \rho_c$ with $\rho_c = 87.5 \mu\text{m}^{-2}$ as determined below and the “magnetization” exponent $\beta = 5/36$ [134], which reproduces the observations well. In Fig. 5.18b, we show the probability Π that a cluster connects opposite sides of a region of size $L \times L$ ($L = 0.5, 1, 2,$ and $3 \mu\text{m}$). For an infinite system, $\Pi = 1$ for $\rho_{\text{np}} \geq \rho_c$, while $\Pi = 0$ for $\rho_{\text{np}} < \rho_c$ [134]. Indeed, Π displays a sharp transition around $\rho_c = 87.5 \mu\text{m}^{-2}$ for $L = 3 \mu\text{m}$, indicating ρ_c is in that vicinity. Next, we probe the width Δ of the transition region, which is expected to scale as $L^{-1/\nu}$, where $\nu = 4/3$ is the correlation-length exponent [134]. We define Δ as the difference in density for $\Pi = 0.9$ and $\Pi = 0.1$ in Fig. 5.18b. The inset of Fig. 5.18b shows that the data are well fitted with $\nu = 1.0 \pm 0.3$, which is consistent with the theoretical expectation.

Finally, we plot in Fig. 5.18c the mean size S of the clusters (excluding the percolation cluster) as a function of ρ_{np} with the theoretical prediction $S \sim |\rho_{\text{np}} - \rho_c|^{-\gamma}$,

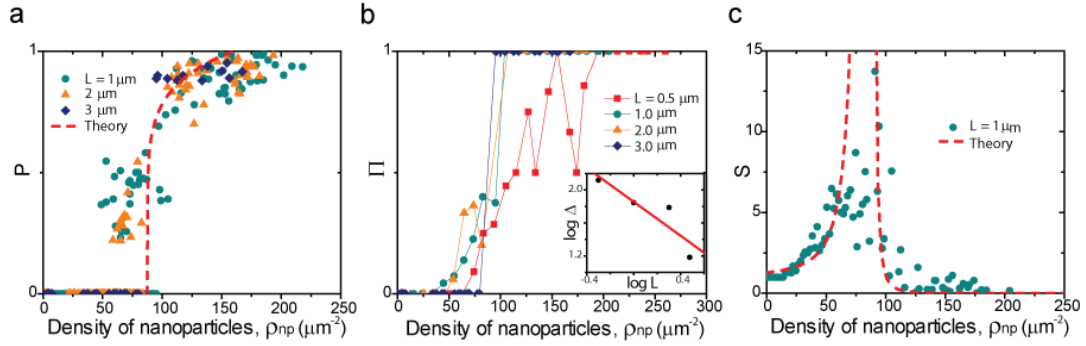


Figure 5.18: Percolation analyses of the wrinkle network. (a) P as a function of nanoparticle density for $L = 1, 2,$ and $3 \mu\text{m}$. (b) Π as a function of the density of nanoparticles for $L = 0.5, 1, 2,$ and $3 \mu\text{m}$. Points for $L = 0.5, 1,$ and $2 \mu\text{m}$ represent averages in a bin of $10 \mu\text{m}^{-2}$. The inset is a plot of $\log \Delta$ as a function of $\log L$; the red line indicates a best-fit power exponent of -1.0 . (c) The mean finite cluster size S as a function of the density of nanoparticles (points represent averages in a bin of $2 \mu\text{m}^{-2}$). The red dashed line is the theoretical expectation).

where $\gamma = 43/18$ is the “susceptibility” exponent [134]. Some Monte Carlo simulations predict a much larger prefactor for $\rho_{np} \leq \rho_c$ (e.g., a critical amplitude ratio of 50 ± 26 for a continuum model [135]), which is in reasonable agreement with the observed ratio of approximately 30. Thus, all measurements strongly support the existence of a 2D percolation transition at a critical density $\rho_c \approx 87.5 \mu\text{m}^{-2}$.

Since the only length scale is X_c , we obtain a universal number (i.e., independent of model parameters such as Γ , E_{2D} , or d) characterizing the wrinkle percolation transition: $\rho_c X_c^2 \approx 0.9$. In contrast, the simple continuum percolation of penetrable discs of diameter X_c leads to $\rho_c X_c^2 \approx 2.9$ [35]. This difference is a consequence of unique structures of the wrinkle network; the number of the wrinkles propagating from single nanoparticles is at most three as shown in Fig. 5.16 and the threefold wrinkle junctions have one angle smaller and two angles larger than 120° as

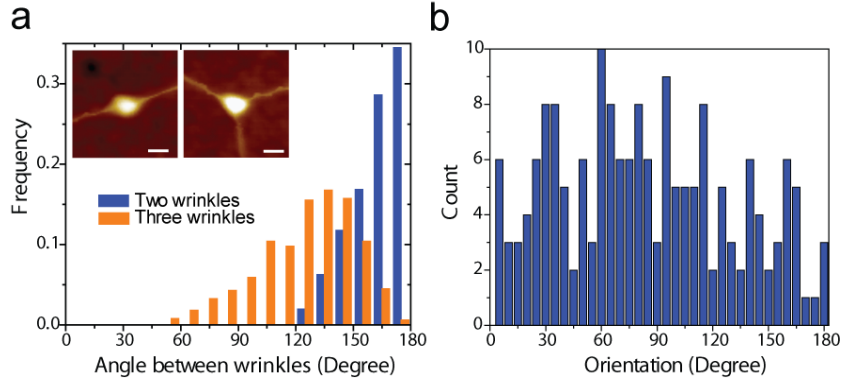


Figure 5.19: The orientations of wrinkles. (a) The distribution of opening angles produced by the neighboring wrinkles at single protrusions for the two (blue) and the three (orange) wrinkles as shown in the insets (more than four wrinkles are exceptionally rare). (b) The orientations of wrinkles.

shown in Fig. 5.19a. (We find no clearly dominant peaks in the orientations of wrinkles as shown in Fig. 5.19b, indicating that the directions of the wrinkles are not determined by the crystallographic directions of graphene.)

5.7 Conclusions

In this chapter, I have presented a systematic study of morphology of graphene membranes supported on SiO₂ substrates with randomly placed topographic perturbations produced by SiO₂ nanoparticles. At low nanoparticle density ρ_{np} , single-layer graphene largely conforms to the substrate except for small regions around the nanoparticles, where graphene is detached. Wrinkles form as ρ_{np} increases, connecting pairs of protrusions. Above a critical density, the wrinkles percolate to form a network spanning the entire sample. As the thickness of graphene increases, it stiffens and delaminates instead of wrinkling. These observations can be explained well within a continuum elastic model and by statistical physical approaches. Since the wrinkling acts to remove inhomogeneous in-plane elastic strains through out-of-

plane buckling, the results can be used to place limits on the possible in-plane strain magnitudes that may be created in graphene to realize strain-engineered electronic structures.

Chapter 6: Oxidative reactivity of graphene on substrates*

As described in Chapter 2, chemical functionalization is an approach to tailoring effectively electronic structures of graphene. A crucial step toward chemically engineering graphene's electronic properties is to understand its chemical reactivity. Graphene's reactivity is expected to be influenced significantly by a supporting substrate; charged impurities trapped in a substrate lead to potential fluctuations, while a non-flat substrate introduces a roughness into graphene as shown in the previous chapter. However, the impact of such substrate effects on graphene's reactivity has remained unclear.

In this chapter, I investigate oxidative reactivity of graphene membranes supported on substrates with various roughnesses and charged impurities and find that graphene's reactivity is predominantly controlled by potential fluctuations induced by charged impurities rather than surface roughness. The observations may point to new strategies for using substrates to control the chemical functionalization and doping of graphene, and therefore graphene's electronic properties.

6.1 Chemical reactivity of graphene

Pristine graphene is relatively inert chemically because of the absence of dangling bonds; in contrast, graphene nanoribbons [40] and graphene with defects [136] are reactive. Nonetheless, single-layer graphene (SLG) supported on SiO₂ shows anomalously large reactivity compared to thicker graphene [137-139]. One

* Adapted from "Charge inhomogeneity determines oxidative reactivity of graphene on substrates" by Mahito Yamamoto, Theodore L. Einstein, Michael S Fuhrer, and William G. Cullen (*ACS Nano*, **6**, 8335-8341, 2012)

possible explanation for this enhanced reactivity is Fermi energy fluctuations in space, *i.e.*, “electron-hole puddles” [33, 34], induced in graphene due to ionized impurities trapped on SiO₂, which limit the carrier mobility of graphene [37, 140, 141]. The electron-hole puddles locally increase the electron (hole) density responsible for electron transfer chemistry [138]. The magnitude of the potential fluctuations, and hence the charged impurity-assisted electron transfer chemistry, decreases with increasing graphene thickness because of (1) higher density of states in multilayer graphene [142], and (2) interlayer screening of charged impurities, where the screening length corresponds to the thickness of bi- to few- layer graphene [138, 143, 144].

Another plausible mechanism for the enhancement of the reactivity is topographic corrugations of graphene induced by coupling to the SiO₂ surface [138, 145]. Due to van der Waals adhesion, graphene deforms significantly on SiO₂, resulting in local curvature and strain [35, 110]. The curvature may lead to the rehybridization of sp^2 to sp^3 bonds [146] and the enhancement of reactivity. The impact of the structural deformations on the reactivity is also expected to attenuate with increasing graphene thickness because graphene layers become significantly stiffer and flatter over SiO₂ [147], with curvature and strain decreasing with thickness. Since SiO₂ induces both significant charge fluctuations [33, 34] and structural deformations in SLG [35, 110], either could account for the enhancement of reactivity of SLG on SiO₂ [138, 148]. In this chapter, we explore which is the major factor determining chemical reactivity of graphene.

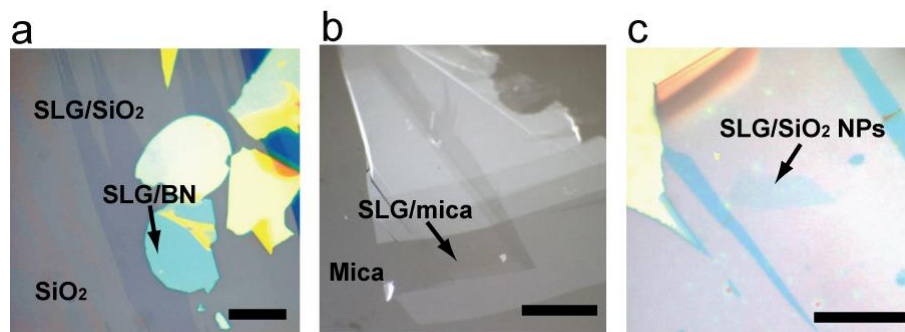


Figure 6.1: Optical images of graphene on various substrates. (a) Single-layer graphene (SLG) on SiO₂ and BN. (b) SLG on mica. (c) SLG on SiO₂ nanoparticles (NPs). The scale bars are 20 μm.

6.2 Experimental details

We employ various substrates with different surface roughnesses and charged impurity densities; hexagonal boron nitride (hBN), mica, thermally-grown SiO₂ on Si, and SiO₂ nanoparticle thin films (Fig. 6.1). Graphene supported on hBN is atomically flat [108, 109], has remarkably high carrier mobility [10], and shows significantly reduced charge inhomogeneity, presumably due to lower concentrations of substrate-trapped charge [108, 109]. Muscovite mica is expected to possess significant concentrations of K⁺ ions on its surface [149], and SLG on mica exhibits comparable carrier mobility to that of SiO₂-supported SLG [150], implying similar concentrations of substrate-trapped charge. Furthermore the cleavage of mica exposes a silicate face [149], chemically very similar to that of amorphous SiO₂. Thus, in common with SiO₂, graphene is supposedly non-reactive to the mica surface. However, graphene deposited on mica is exceedingly flat [107]. SiO₂ nanoparticles on a SiO₂ substrate produce a graphene support with significantly higher roughness than, but similar chemical properties to, thermally-grown SiO₂ on Si.

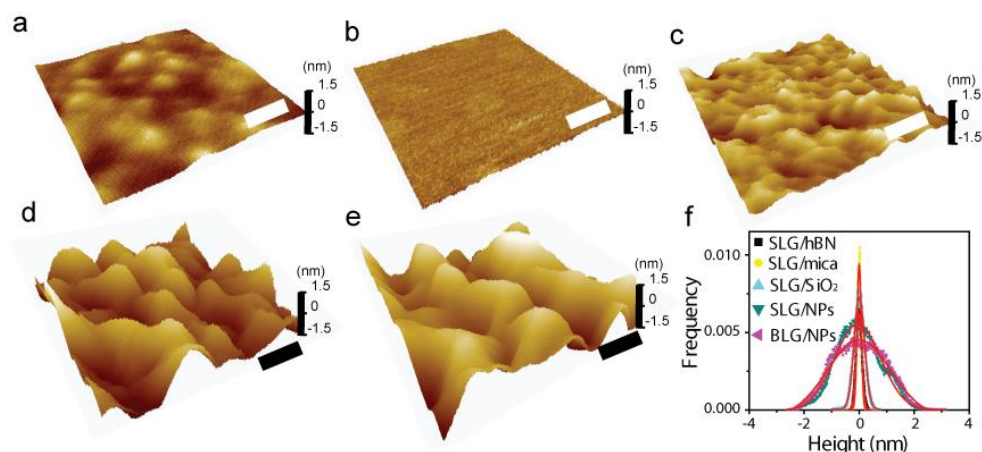


Figure 6.2: AFM images of graphene supported on various substrates. SLG on (a) hBN, (b) mica, (c) SiO₂, (d) a SiO₂ nanoparticles thin film, and (e) BLG on a SiO₂ nanoparticle thin film. The scale bars are 40 nm. (f) Height histograms of graphene surfaces for the images shown in (a)-(e). Solid red lines are Gaussian fits.

Figures 6.2a-d show typical AFM topographic images of SLG supported on (a) hBN (~ 9 nm thick supported on SiO₂), (b) mica, (c) SiO₂, (d) SiO₂ nanoparticles. Additionally, Fig. 6.2e shows an AFM image of bilayer graphene (BLG) on SiO₂ nanoparticles. These samples were annealed in Ar/H₂ flow at 400 °C for 6 hours to remove any adhesive residue and achieve equilibrium structures. Figure 6.2f shows the height histograms of the images in Figs. 6.2a-e; mica-supported graphene is the flattest, followed by graphene on hBN, SiO₂, and SiO₂ nanoparticles.

Table 6.1 summarizes the root mean square (RMS) roughness σ and the characteristic length l of graphene surfaces. We measure the RMS roughness and the characteristic length by employing the one-dimensional autocorrelation function for a uniformly rough surface, which is defined as $G(x_0) = \langle z(x)z(x+x_0) \rangle$, where $z(x)$ is the height of the surface at position x . The autocorrelation function is often assumed

	SLG/hBN	SLG/mica	SLG/SiO ₂	SLG/NPs	BLG/NPs
σ (nm)	0.14±0.04	0.05±0.02	0.23±0.01	1.29±0.12	1.30±0.11
l (nm)	24±11	1.7±0.6	13±2	21±5	22±4
σ/l^2 ($\times 10^{-4} \text{ nm}^{-1}$)	2.4±2.2	N/A	14±5	30±15	27±10
$10^{-5} \times (\sigma/l)^2$	3.2±3.5	N/A	31±11	389±208	352±145

Table 6.1: The RMS roughness σ , the characteristic length l , the estimated curvature σ/l^2 , and strain $(\sigma/l)^2$ of SLG on hBN, mica, SiO₂, and SiO₂ nanoparticles (NPs) and BLG on NPs.

to be $G(x_0) = \sigma^2 \exp(-x_0^2/l^2)$, where σ is the RMS roughness and l is the correlation length [151]. Thus, we determine σ and l by fitting the autocorrelation function obtained from a number of 200 nm \times 200 nm AFM images of graphene on each substrate to the theoretically expected form.

Since graphene on mica is exceedingly flat, we expect that the RMS roughness and the characteristic length reflect the AFM height resolution limit and AFM noise, respectively, as previously noted [107]. In order to quantitatively assess the deformations present in graphene, we roughly estimate curvature and strain by σ/l^2 and $(\sigma/l)^2$, as shown in Table 6.1. By relative comparison, we find much larger deformations in SLG and BLG on SiO₂ nanoparticles than in SLG on SiO₂. We note, however, that nanometer-scale roughness of a substrate may produce sharp mechanical deformations (conical singularities) in graphene, which would be unresolved by our tapping-mode AFM. These localized deformations are expected to significantly perturb local density of states of graphene near the apex [130] and as a result may contribute to reactivity of graphene.

BN flakes were exfoliated onto Si substrates with a 300 nm oxide layer from commercially available BN powder (Momentive, Polartherm grade PT 110) [152]. Muscovite mica was cleaved in a N₂ atmosphere to minimize the chance of a water layer on the mica surface [107, 153]. SiO₂ nanoparticle thin films were prepared by spin-coating SiO₂ nanoparticle dispersions (diameter 10-20 nm; Nissan Chemical America Corp., SNOWTEX-O) onto SiO₂ substrates. Graphene was mechanically exfoliated from Kish graphite using water-soluble tape as described in Chapter 3. In this study, we investigate oxidative reactivity of graphene on each substrate. Graphene oxidation was carried out by annealing graphene in an Ar/O₂ mixture for 2-5 hours at temperatures ranging from 350 to 600 °C. We employed atomic force microscopy (AFM) in ambient and Raman spectroscopy with a fixed laser wavelength of 532 nm, unless otherwise noted, to characterize the oxidative reactivity of graphene on substrates.

6.3 Experimental results and discussion

Figure 6.3 shows AFM images of SLG on (a) SiO₂, (b) BN, and (c) mica after oxidation at 500 °C for 2 hours. Oxidation results in circular etch pits in SLG in SiO₂

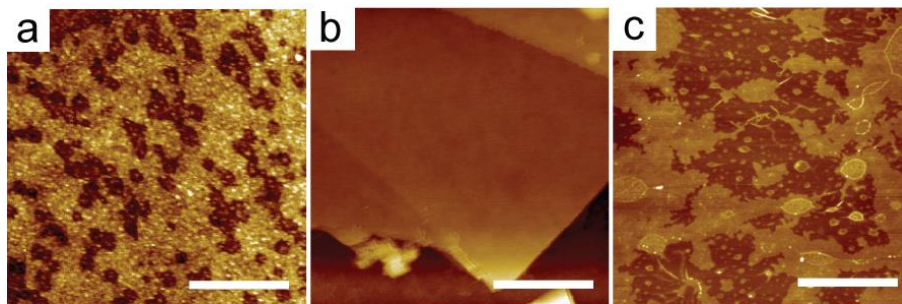


Figure 6.3: AFM images of SLG supported on various substrates after oxidation at 500 °C for 2 hours. (a) SiO₂, (b) BN, and (c) mica. The scale bars are 1 μm.

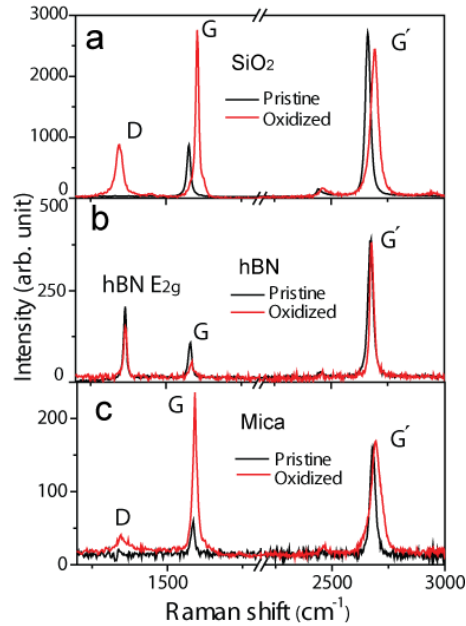


Figure 6.4: Raman spectra of SLG on various substrates before and after oxidation at 500 °C for 2 hours. (a) SiO₂, (b) hBN, and (c) mica. The Raman spectra are normalized to the G' peak intensities.

(Fig. 6.3a), as reported previously [138]. However, SLG on BN is non-reactive with oxygen molecules at the same temperature (Fig. 6.3b). SLG on mica is etched upon oxidation, as shown in Fig. 6.3c.

In Fig. 6.4, we show typical Raman spectra of graphene supported on SiO₂, hBN, and mica before (black solid lines) and after (red solid lines) oxidation at 500 °C for 2 hours. Previous studies of graphene oxidation have reported hole-doping and disorder in reaction with oxygen [138, 151]. On SiO₂, we find that the Raman G band upshifts from ~ 1582 to 1603 cm⁻¹ which roughly corresponds to a dopant concentration of ~ 2×10^{13} cm⁻² [137, 100, 101]. Additionally, the Raman D peak at ~ 1350 cm⁻¹ is activated after oxidation because of formation of etch pits (see Fig. 6.3a), as previously reported [137].

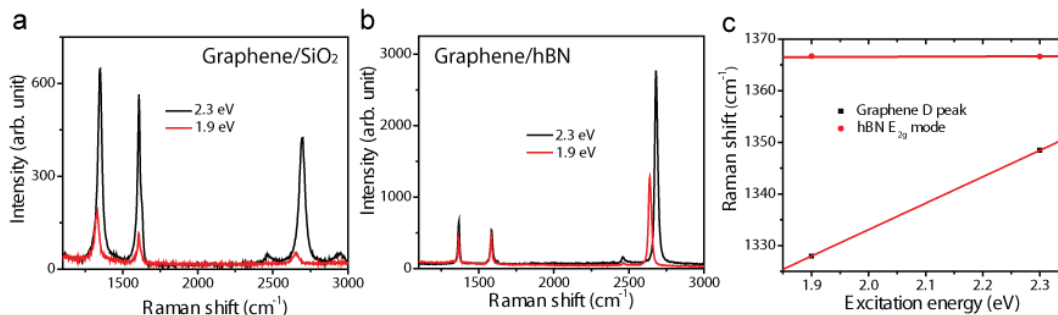


Figure 6.5: Non-dispersive behavior of the Raman E_{2g} mode of BN. (a) and (b) Raman spectra of SLG on (a) SiO_2 and (b) hBN after oxidation at 450°C for 5 hours. (c) The Raman D band energy of graphene and the hBN E_{2g} mode as a function of the laser excitation energy. The red solid line for the D band energy is a line fit with a slope of $\sim 51\text{ cm}^{-1}/\text{eV}$.

On hBN the upshift of the G band energy is minor (from 1580 cm^{-1} to 1585 cm^{-1}); furthermore, the Raman D peak is absent, indicating that doping in graphene is significantly suppressed and graphene is not etched, as can be seen in Fig. 6.3b. (hBN shows the E_{2g} Raman mode at $\sim 1360\text{ cm}^{-1}$ [154] but this non-dispersive mode can be distinguished from the dispersive graphene D mode by using longer-wavelength excitation as shown in Fig. 6.5.)

The suppression of the reactivity of graphene was consistently observed on hBN for all samples at oxidative temperatures below 550°C (we obtained no samples of hBN thickness $< 9\text{ nm}$). In contrast to hBN-supported SLG, SLG on mica is partly etched by oxidation as shown in Fig. 6.3c, which is also evidenced by the Raman D peak in Fig. 6.4c.

In Fig. 6.6a, we plot the Raman G band energies of SiO_2 -, hBN-, and mica-supported SLG graphene as functions of temperature. The relatively large G band energy of pristine SLG on mica results from hole doping by preexisting surface charges on the substrate [155]. The G band energies of SLG on SiO_2 and on mica

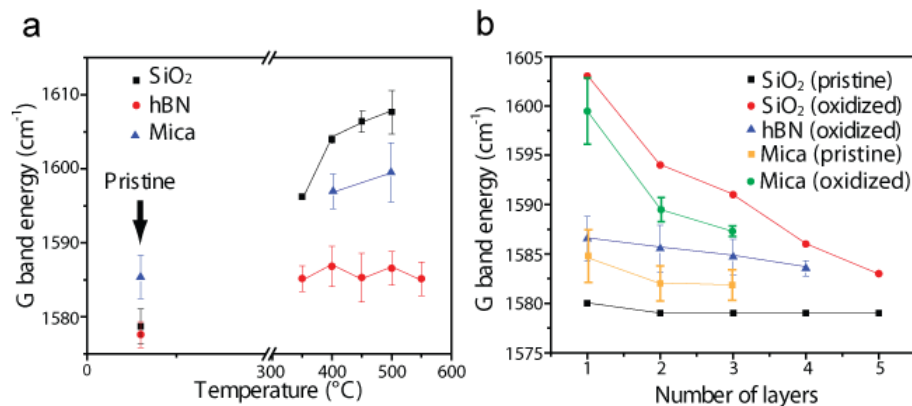


Figure 6.6: The Raman G band energies of oxidized graphene on substrates as functions of temperature and graphene thickness. (a) The Raman G band energies of SLG on SiO₂ (black square dots), hBN (red circular dots), and mica (blue triangular dots) as functions of oxygen treatment temperature. (b) The Raman G band energies of pristine graphene on SiO₂ (black square dots) and on mica (yellow square dots) and 500 °C-oxidized graphene on SiO₂ (red circular dots), on hBN (blue triangular dots), and on mica (green circular dots) as functions of number of graphene layers.

increase with increasing temperature, indicating doping due to reaction with oxygen molecules, while hBN-supported graphene shows a nearly constant G band energy of $\sim 1585 \text{ cm}^{-1}$ at 350-550 °C, indicating little doping.

We also examine the G band energy as a function of graphene thickness in Fig. 6.6b. On SiO₂ and on mica, SLG shows the largest G-band shift (largest doping). The G-band energies diminish with thickness, indicating larger reactivity of SLG compared to thicker graphenes, while the G-band shift for graphene on hBN does not depend on thickness. These observations suggest that on hBN SLG is comparable to thick graphene in terms of oxidative doping.

We now investigate the reactivity of graphene on hBN in terms of oxidative etching in detail. Figure 6.7a shows an optical image of SLG supported on BN and on

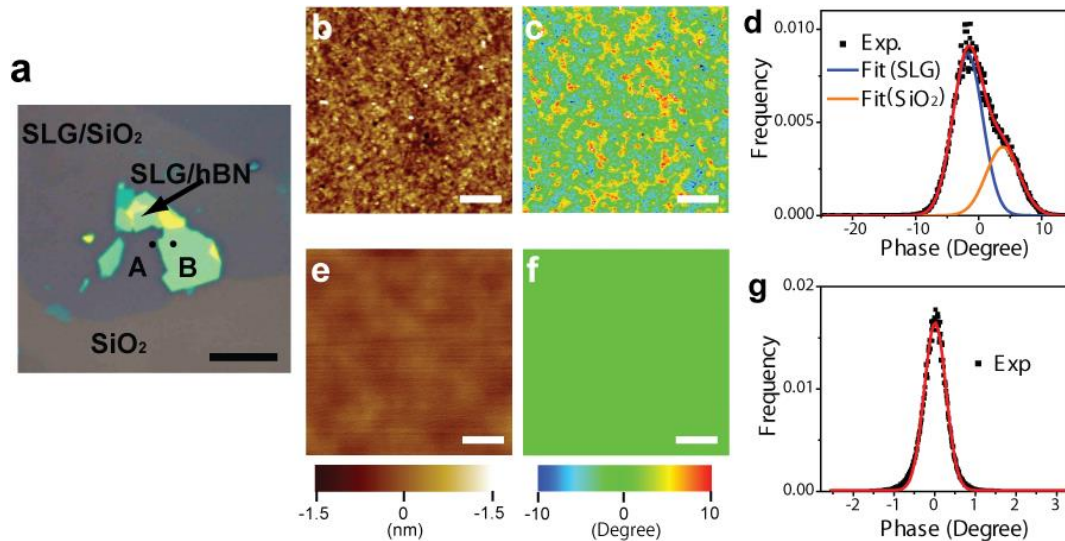


Figure 6.7: Oxidation of graphene on SiO₂ and BN at 450 °C for 5 hours. (a) An optical image of graphene on SiO₂ and BN before oxidation. (b-c) Typical AFM (b) height and (c) phase images of SLG on SiO₂ near point A in panel (a) after oxidation at 450 °C for 5 hours. The scale bars are 200 nm. (d) Histogram of phase variations in (c). The red solid line is multi peak Gaussian fit, consisting of two peaks derived from graphene (blue) and SiO₂ (orange) surfaces. AFM (e) height and (f) phase images of SLG on hBN after oxidation at 450 °C for 5 hours. The scale bars are 200 nm. (g) Phase histogram of the image in (f). The solid line is a Gaussian fit.

SiO₂. After oxidation of this graphene film at 450 °C for 5 hours, graphene strongly couples to SiO₂, making it difficult to distinguish graphene and uncovered SiO₂ from an AFM height image as shown in Fig. 6.7b. We therefore use AFM phase imaging to distinguish SLG from etched regions.

We first show that a phase image at edges of pristine SLG on SiO₂ discriminates clearly between graphene and the supporting SiO₂. Figures 6.8a and b show the AFM height and phase images of graphene on SiO₂ after H₂ annealing to remove tape residues on graphene. In Fig. 6.8b, we find a clear phase difference between pristine graphene and SiO₂. Figures 6.8c shows the phase histogram of the

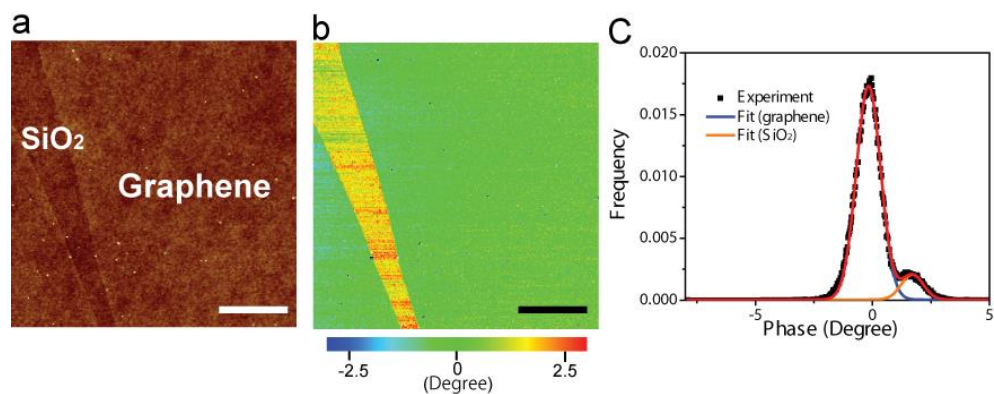


Figure 6.8: An AFM phase image of pristine graphene on SiO₂. (a-b) AFM (a) height and (b) phase images of graphene on SiO₂. The scale bars are 1 μm . (c) Histogram of phase variations in (b). The red solid line is a multi-peak Gaussian fit, consisting of two peaks derived from graphene (blue) and SiO₂ (orange) surfaces.

image in Fig. 6.8b. The histogram clearly consists of two components: graphene (blue solid curve) and SiO₂ (orange solid curve).

Now we show the phase image of oxidized SLG on SiO₂. The phase image clearly shows variations, indicating that the scanned region is compositionally inhomogeneous. Furthermore, the multi-peak Gaussian fit of the phase histogram in Fig. 6.7d consists of two components; the smaller peak corresponds to graphene, while the larger peak corresponds to uncovered SiO₂ where SLG has been etched. Figures 6.7e and f show AFM height and phase images of SLG on hBN, corresponding to point B in Fig. 6.7a after oxidation at 450 °C for 5 hours. In contrast to SiO₂-supported graphene (Figs. 6.7c and d), the phase image is homogeneous (see also the phase histogram in Fig. 6.7g), which indicates the absence of any etch pits in graphene and the significantly reduced reactivity of hBN-supported graphene.

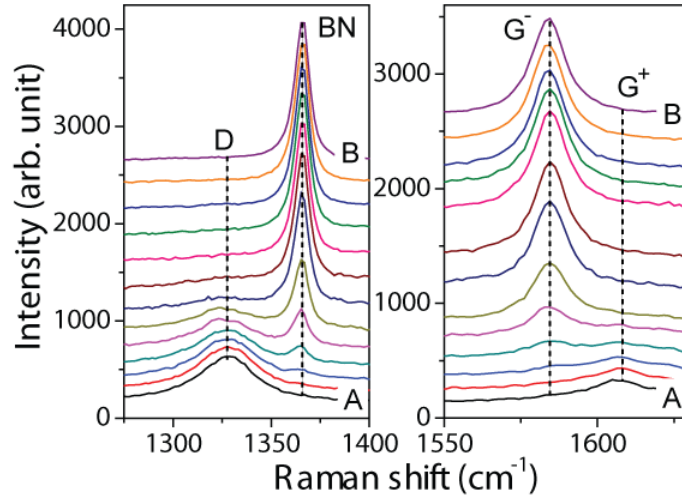


Figure 6.9: A series of Raman spectra of oxidized SLG supported on SiO₂ and BN. The Raman spectra from A (on SiO₂) to B (on hBN) shown in Fig. 6.7a. The spacing between points at which the Raman spectra are measured is 0.3 μm.

Figure 6.9 shows the Raman spectra of SLG oxidized at 450 °C for 5 hours at different positions between A and B represented in Fig. 6.7a. The spacing between neighboring points is 0.3 μm. Since the D band energy is dispersive with respect to the excitation energy of the laser and increases with the energy (see Fig. 6.5 and Chapter 4), we here used a laser wavelength of 633 nm to clearly distinguish the D peak of SLG and the peak derived from the hBN E_{2g} mode. On SiO₂ at point A, we see the graphene D peak, while on hBN at point B the graphene D peak is absent and the hBN E_{2g} mode is present, suggesting the absence of defects in SLG on hBN. The region of coexistence of the D peak and the hBN E_{2g} peak in the Raman spectra is of order 1 μm wide, comparable to the laser spot size, indicating that both SiO₂- and hBN-supported graphene are illuminated in this region. We also observe a splitting of the graphene G band into two peaks G⁻ (1583 cm⁻¹) and G⁺ (1610 cm⁻¹) in the same intermediate region, resulting from undoped graphene on hBN and highly doped

graphene on SiO₂, respectively. Splitting rather than shifting of the G peak again indicates an abrupt transition in doping from SiO₂-supported to hBN-supported graphene.

The observed reduced reactivity of SLG on hBN relative to SiO₂ can be explained by either hBN's flatness or its reduced charged inhomogeneity. To probe the impact of charge inhomogeneity on the oxidative reactivity, we further investigate the oxidation of graphene on mica, which is atomically flat (as shown in Fig. 6.2b) but presumably exhibits comparable charge inhomogeneity to SiO₂-supported graphene as described above [150].

As shown in Fig. 6.3c, in contrast to hBN-supported SLG, SLG on mica is partly etched by oxidation. Thus, the flatness of graphene alone does not suppress its

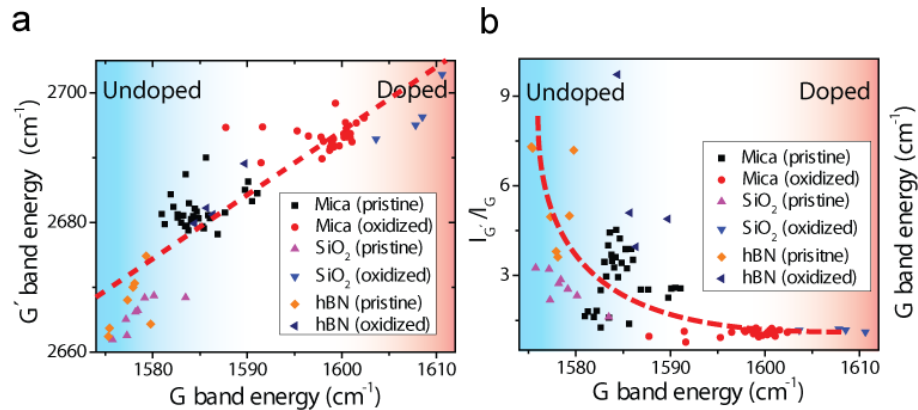


Figure 6.10: The Raman G' modes of oxidized graphene on various substrates. (a) The Raman G' band energies of SLG on mica, hBN, and SiO₂ before and after oxidation at 500 °C as functions of the Raman G band energy. The dashed line is a line fit with a slope of 0.98 ± 0.05 . (b) The intensity ratios of the Raman G' peak to the G peak of graphene on mica, hBN, and SiO₂ before and after oxidation at 500 °C as functions of the Raman G band energy. The dashed curved line is a guide to the eye.

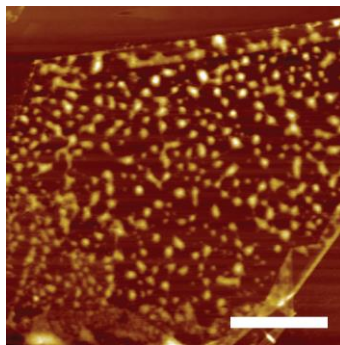


Figure 6.11: An AFM image of water islands trapped between SLG and mica. The scale bar is 2 μm .

reactivity. We further examine doping behaviors of graphene on mica before and after oxidation. It has been empirically demonstrated that the Raman G' band energy increases with increasing concentration of hole carriers, showing a nearly linear relationship with the G band energy [101]. Additionally, the relative intensity of the G' band to the G band characteristically decreases with carrier concentration [101].

Figure 6.10a displays the G' band energy of SLG on SiO_2 , hBN, and mica as a function of the G band energy before and after oxidation at 500 $^\circ\text{C}$ for 2 hours. Each data point is obtained from a different graphene flake on each substrate. With oxidation, the G' band energies of graphene on SiO_2 and on mica increase together with the G band energy. The nearly linear relationship between the G' and G band energies, with a slope of 0.98 ± 0.05 , is consistent with previous observations [101, 155], indicating hole-doping of graphene by oxidation. Graphene on hBN shows the lowest G and G' peak positions after oxidative treatment, consistent with low reactivity. Figure 6.10b shows the intensity ratio of the G' peak ($I_{G'}$) to the G peak (I_G) as a function of the G band energy. Each data point again corresponds to a different graphene sample. The significant decrease of $I_{G'}/I_G$ of graphene on mica and

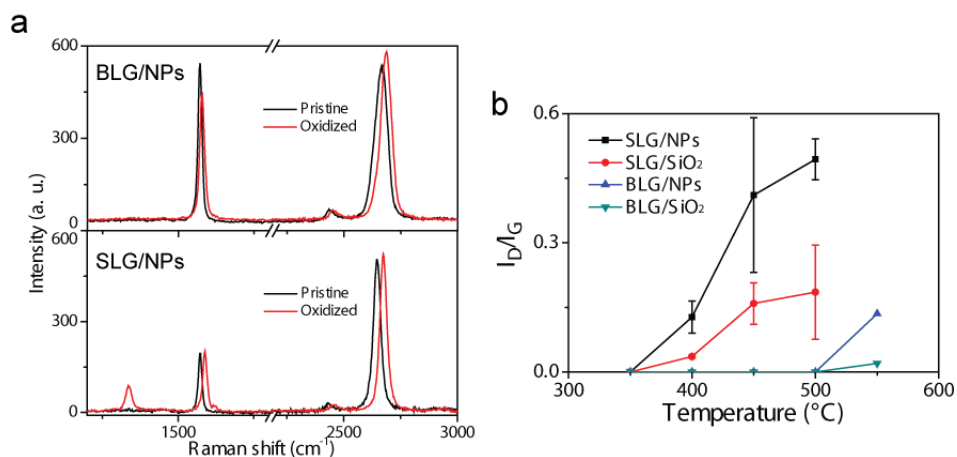


Figure 6.12: Raman spectra of oxidized graphene on SiO₂ nanoparticles. (a) Raman spectra of BLG (top) and SLG (bottom) on SiO₂ nanoparticles before and after oxidation at 500 °C for 2 hours. (b) The intensity ratios of the Raman D peak to G peak of SLG and BLG on SiO₂ and on SiO₂ nanoparticles as functions of oxygen treatment temperature.

SiO₂ after oxidation also strongly supports oxidative doping of these samples. In contrast, I_G/I_G for graphene on hBN shows no clear trend upon oxidation, and the higher values of I_G/I_G for graphene on hBN compared to mica or SiO₂ are consistent with low oxidative reactivity.

The large reactivity of SLG on mica and its diminution with thickness, as shown in Fig. 6.6b, indicates that flatness is not the reason for reduced reactivity of SLG on hBN, and we conclude that substrate charged impurities play the dominant role in controlling the reactivity of SLG on a substrate. Even though graphene is deposited onto freshly cleaved mica in a N₂ atmosphere, water layers are often trapped on mica (see Fig. 6.11). The water layers act to block charge transfer between charged impurities on mica and graphene [155]. The distinct morphology of mica-supported SLG after oxygen treatment in Fig. 6.3c is presumably because the regions

covering water layers in graphene are less reactive to oxygen molecules and so not etched.

Finally, we probe the oxidative reactivity of graphene supported on an extremely corrugated substrate of a SiO₂ nanoparticle thin film. Figure 6.12a shows typical Raman spectra of SLG and BLG on SiO₂ nanoparticles before and after oxidation at 500 °C for 2 hours. After oxidation, the D peak of SLG is activated but is absent for BLG. In Fig. 6.12b, we plot the intensity ratio of the D peak (I_D) to the G peak (I_G) of graphene on SiO₂ nanoparticles and, for comparison, on bare SiO₂ as a function of oxygen treatment temperature. On both thermally-grown SiO₂ and SiO₂ nanoparticle thin films, the D peaks of SLG are activated above 400 °C. In contrast, the D peaks of BLG are not activated below 500 °C regardless of substrate. Thus, the increased reactivity of SLG relative to BLG on SiO₂ is not caused by increased corrugation on the few-nanometer length scale (see Table 6.1: BLG on SiO₂ nanoparticles is rougher than SLG on SiO₂ in terms of curvature and strain). We cannot completely rule out the possibility that sharp conical singularities [130] undetected by AFM are playing a role in the reactivity; however that scenario would not explain the similar reactivity of flat graphene on mica which should not exhibit conical singularities. The results indicate that the differences in reactivity are due to the difference in electronic structure. The increased reactivity of SLG relative to BLG is consistent with charge disorder cause: SLG has significantly lower density of electronic states and therefore larger fluctuations in chemical potential for a given charged impurity concentration [142].

6.4 Conclusions

In this chapter, I have measured the oxidative reactivity of SLG supported on substrates with different surface roughnesses and charged impurities. SLG on flat hBN with low charged impurities shows reduced oxygen reactivity comparable to multilayer graphene, while SLG on flat mica shows reactivity similar to SLG on SiO₂, pinpointing charge disorder as the source of the increased reactivity of SLG. This is strongly supported by the observation that reactivity of graphene on SiO₂ depends on layer number (SLG *vs.* BLG) but not on graphene roughness (SiO₂ nanoparticle substrates *vs.* thermally-grown SiO₂). Furthermore, similar results have been reported by other groups [156]. These observations may offer an approach to control of the chemical functionalization and doping of graphene using a substrate.

Chapter 7: Oxidative reactivity of atomically thin MoS₂ on SiO₂*

In Chapter 6, I show that chemical reactivity of graphene on substrates is predominantly controlled by charge inhomogeneity rather than surface roughness. A natural question is whether other atomic crystals such as layered transition metal dichalcogenides show similar substrate-dependent reactivity. In this chapter, I explore oxidative reactivity of atomically thin MoS₂ supported on SiO₂. Oxygen exposure leads to etch pits on the basal plane surfaces of atomically thin MoS₂ on SiO₂. However, I find that, in striking contrast with graphene, the density of etch pits is independent of MoS₂ thickness, exposure time, and oxidation temperature but varies significantly from sample to sample. The observations indicate that oxidative etching of atomically thin MoS₂ is initiated at intrinsic defect sites in the crystal rather than being activated by substrate effects such as charged impurities and surface roughnesses. The results provide new insight into the reactivity of 2D transition metal dichalcogenides supported on substrates.

7.1 Oxidative reactivity of MoS₂

MoS₂ has attracted much attention as a solid lubricant due to its ultralow friction and wear [72, 157]. The tribological properties of MoS₂ are affected strongly by oxidation and, hence, oxidative reactivity of MoS₂ has been of central interest for a long time. Oxygen exposure to bulk MoS₂ results in molybdenum oxide (MoO₃) on

* Adapted from “Anisotropic etching of atomically thin MoS₂” by Mahito Yamamoto, Theodore L. Einstein, Michael S Fuhrer, and William G. Cullen (*submitted*)

its basal plane surface as well as edges and, hence, raises its friction and reduces lifetime as a lubricant [157-160]. However, oxidative reactivity of atomically thin MoS₂ has yet to be investigated.

7.2 Experimental details

Single- and few-layer MoS₂ were mechanically exfoliated onto 300 nm-thick SiO₂ from MoS₂ bulk crystals using adhesive tape (see Chapter 3). The thicknesses of the MoS₂ films were identified by optical contrast, atomic force microscopy (AFM), and Raman spectroscopy [104, 161]. To remove adhesive residue, all samples were annealed in an H₂/Ar mixture for 2 hours at 350 °C unless otherwise noted. The flow rates of Ar and H₂ are 1.7 L/min and 1.8 L/min, respectively. This hydrogen treatment leads to no chemical modification of the MoS₂ basal plane, as shown in an AFM image and Raman spectra in Fig. 7.1. After pre-annealing MoS₂ samples in H₂, they were exposed to an Ar/O₂ mixture at temperatures ranging from 27 to 400 °C. The flow rates of Ar and O₂ are 1.0 L/min and 0.7 L/min, respectively. The nanoscale

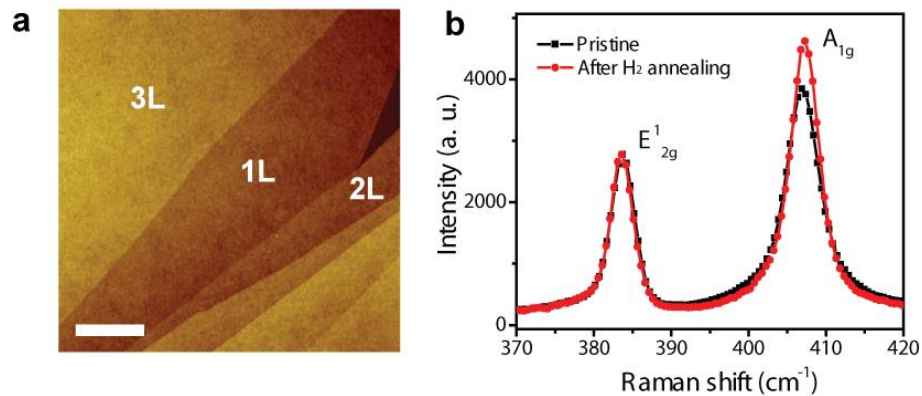


Figure 7.1: Atomically thin MoS₂ on SiO₂ after H₂ annealing. (a) An AFM image after H₂ treatment at 350 °C for 2 hours. The scale bar is 1 μm. (b) Raman spectra of atomically thin MoS₂ before (black line) and after (red line) H₂ annealing.

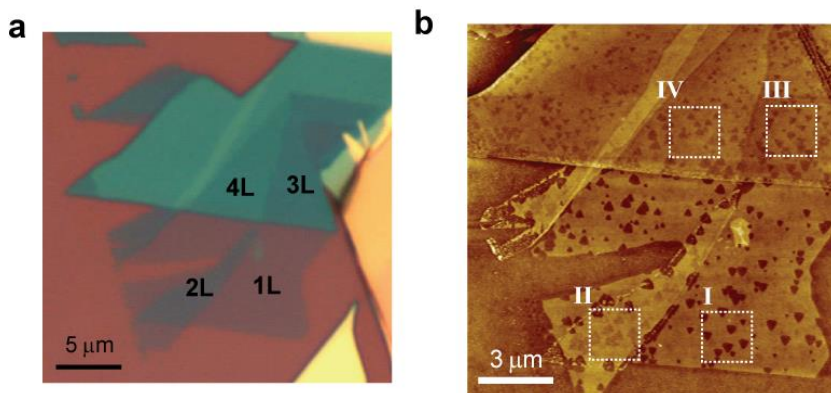


Figure 7.2: Atomically thin MoS₂ on SiO₂ after O₂ annealing. (a) An optical image of a pristine MoS₂ flake. (b) An AFM image of the MoS₂ flake after oxidation at 320 °C for 3 hours, showing etch pits on the surface.

structure of oxidized MoS₂ was characterized by AFM in tapping mode, and the composition and oxidation state were determined using Raman spectroscopy with a fixed excitation wavelength of 532 nm and 2400 gratings per mm.

7.3 Experimental results and discussion

Figure 7.2a is a typical optical image of atomically thin MoS₂ on SiO₂. Figure 7.2b shows an AFM image of this MoS₂ flake after oxygen annealing at 320 °C for 3 hours. The oxygen treatment results in etch pits on the surfaces of single- and few-

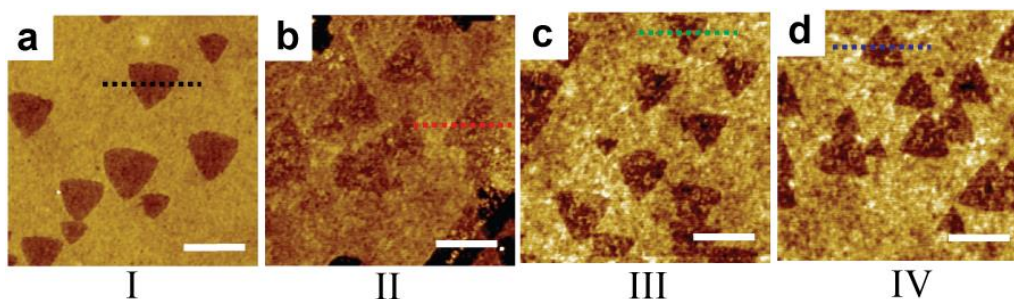


Figure 7.3: AFM images of triangular etch pits on atomically thin MoS₂. (a) single-, (b) bi-, (c) tri-, and (d) 4-layer MoS₂. I-IV correspond to areas shown in Fig. 7.2b. The scale bars are 500 nm.

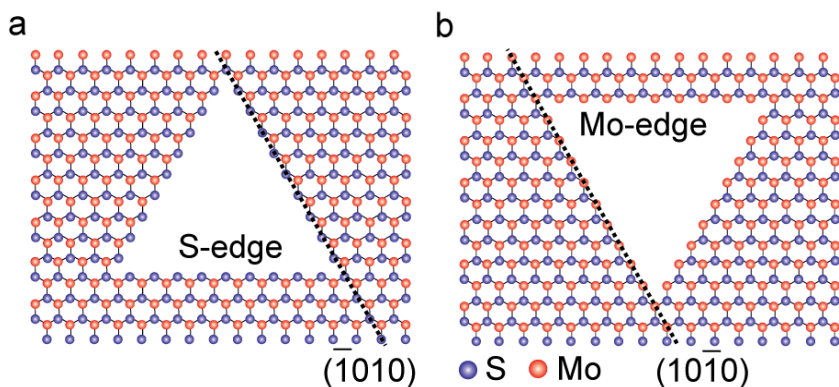


Figure 7.4: Schematic drawings of hexagonal lattice of the MoS₂ structure with triangular pits. A pit with (a) $(\bar{1} 0 1 0)$ S- and (b) $(1 0 \bar{1} 0)$ Mo-edge terminations.

layer MoS₂. Figures 7.3a-e magnify the areas I-IV in Fig. 7.2b, which are surrounded by white dashed lines. The shape of the pits is triangular and their orientations are identical over each atomically-flat terrace. These observations indicate that the triangular shapes of the pits reflect the lattice of the MoS₂ basal plane surface and that the edges of the pits are along the zigzag directions with only a single chemical termination, i.e. terminated on either the Mo-edge $(1 0 \bar{1} 0)$ or S-edge $(\bar{1} 0 1 0)$ (see Fig. 7.4). The observation of only three preferred edge orientations rules out armchair-oriented edges, for which there are six possible identical edges.

Our experiments are unable to resolve whether the preferred edge is the Mo-edge or S-edge; however, evidence from other studies points to Mo-edge $(1 0 \bar{1} 0)$ [162-165], though the exact structure of the reconstructed edge (and locations of additional sulfur atoms terminating the Mo-edge) likely depends on the chemical environment and substrate [163-165].

Control of edge structures is expected to lead to tunable properties of atomically-thin MoS₂ nanostructures [162-168]. The prismatic edges of semiconducting MoS₂ can exhibit metallic edge states [162, 167, 168] and magnetism

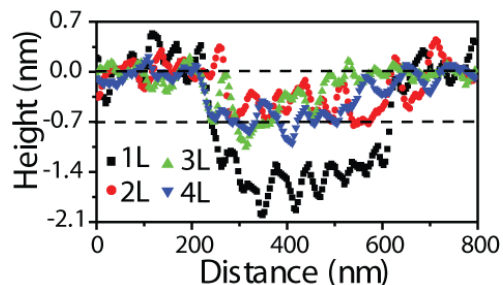


Figure 7.5: The depth of the triangular pits. Profiles of pits along the dashed lines in Figs. 7.3a-d.

[166-168], with the properties sensitively dependent on the edge orientation and atomic reconstruction [166, 167]. The edge structure [163, 165] and number of active edge sites [165, 169, 170] are also crucial for electrocatalytic activity of MoS₂. Our results may signify an approach to create MoS₂ nanostructures with atomically-well defined edges by oxidation. Further work using high-resolution transmission electron microscopy or scanning tunneling microscopy could determine the edge structures and also elucidate the electronic and magnetic properties of these edges.

Figure 7.5 shows the profiles of the pits along the dashed lines in Figs. 7.3a-d.

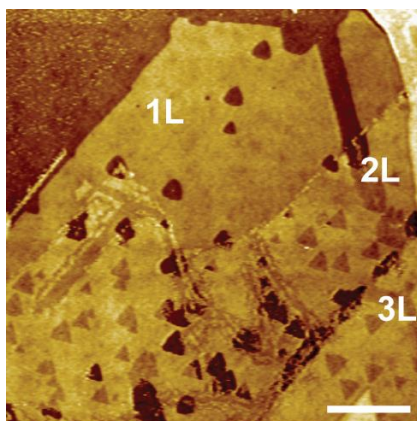


Figure 7.6: An AFM image of atomically thin MoS₂ on SiO₂ after O₂ annealing at 320 °C for 3 hours. The etch pits have the same orientations on single- and bi-layer parts. The scale bar is 2 μm.

The pits are mostly single-layer-deep (~ 0.7 nm) on single- and few-layer MoS₂, indicating a very high degree of anisotropy in etching along the basal plane *vs.* the *c*-axis, though we do occasionally observe double-layer-deep pits on few-layer MoS₂ samples (see Fig. 7.6). (The larger depth of the pits on single-layer MoS₂ in Fig. 7.3a is an artifact caused by the limitation of the tapping mode AFM to determine the thickness of an atomically thin membrane on rough SiO₂ [171].)

Our MoS₂ crystals are expected to have a 2H structure [16, 68], where the triangular lattices of adjacent layers are 180°-inverted relative to each other as shown in Fig. 2.5 in Chapter 2. Therefore, the triangular pits formed on the surfaces are also expected to have 180°-inverted orientations among even and odd numbers of layers. Such trends can be seen in Fig. 7.2b. However, we also observe the triangular pits with same orientations on even and odd layer-number-thickness regions, suggesting that it is the top surface which is continuous across the layer-number-thickness boundary. Figure 7.6 shows etch pits have the same orientations on both single-layer and bi-layer parts, but the orientation is 180°-inverted on tri-layer part. However, AFM is insufficient to determine whether the second layer lies above or below the

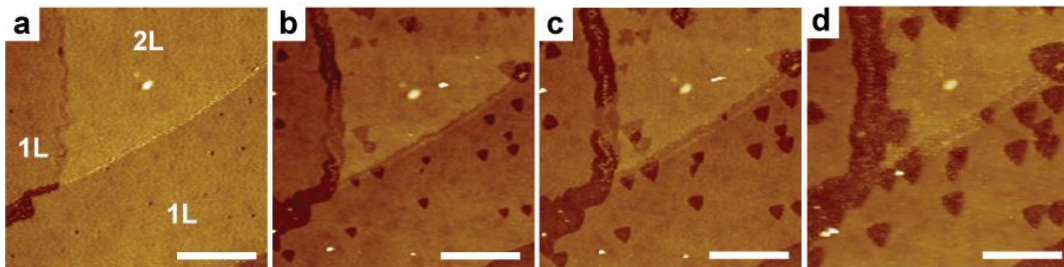


Figure 7.7: A series of AFM images of single- and bi-layer MoS₂ oxidized at 320 °C. The exposure times are (a) 1, (b) 3, (c) 4, and (d) 6 hours. The scale bars are 2 μ m.

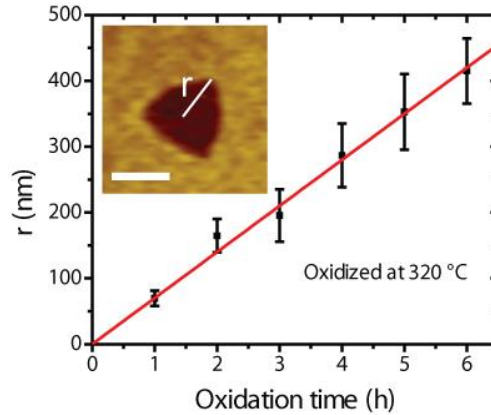


Figure 7.8: The growth rate of the triangular pits. The average distance r from the center to the apex of triangular pits as a function of oxidation time. The red line is fit. The inset is an AFM image of a typical triangular pit formed on single-layer MoS₂ after oxidation for 4 hours. The scale bar is 300 nm.

first layer. Because of this ambiguity, we cannot be certain of the correlation between the stacking order of MoS₂ layers and the orientations of the triangular pits; however, the observations of only a single etch-pit orientation within a single terrace, and the observation of opposite orientations for different layer thicknesses within a single crystal, suggests strongly that the termination is globally determined to be along only one of the Mo or S terminated zigzag edges.

In Figs. 7.7a-d, we show AFM images of a MoS₂ flake of single- and bi-layer

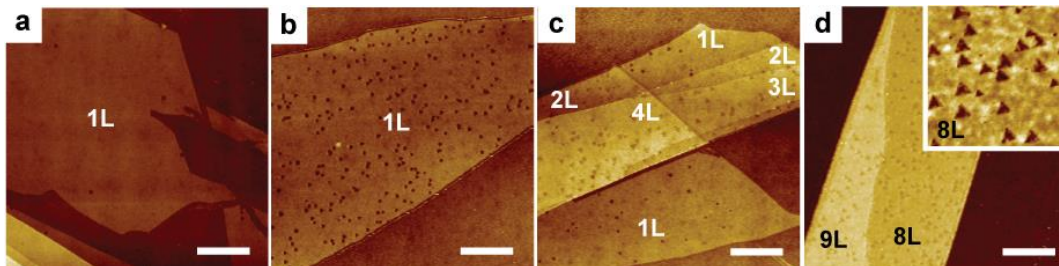


Figure 7.9: (a-d) AFM images of MoS₂ samples of various thicknesses after oxidation at 320 °C for 2 hours. The scale bars are 2 μm. The inset in (d) is a 1 μm × 1 μm area in the 8L region, showing triangular pits.

thickness after oxidation at 320 °C for 1, 3, 4, and 6 hours. After oxidation for an hour, etch pits with an average size of $6.3 \times 10^3 \text{ nm}^2$ are formed on the surfaces (Fig. 7.7a). Additional oxygen treatment leads to lateral growth of the triangular pits, as shown in Figs. 7.7b-d. The distance r from the center to the apex of the triangular pits increases monotonically with a growth rate of approximately 70 nm/h, as shown in Fig. 7.8, but the density of pits is nearly constant during the oxygen treatment, indicating that the oxidative etching is not initiated homogeneously but at specific sites on the surface of atomically thin MoS₂.

Figures 7.9a-d show AFM images of MoS₂ samples of various thicknesses after oxidation at 320 °C for 1 hour. In Fig. 7.9a, the density of etch pits formed on the single-layer MoS₂ film is $7.5 \times 10^6 \text{ cm}^{-2}$, while the pit density on single-layer MoS₂ in Fig. 7.9b is two orders of magnitude larger than that in Fig. 7.9a. Figure 7.9c shows a MoS₂ flake of single- to 4-layer thickness with etch pits on the surfaces. The density of pits on 4-layer MoS₂ is $3.5 \times 10^8 \text{ cm}^{-2}$, which is larger than the densities on surfaces of single-layer ($9.0 \times 10^7 \text{ cm}^{-2}$) and tri-layer ($2.7 \times 10^8 \text{ cm}^{-2}$) parts. Figure

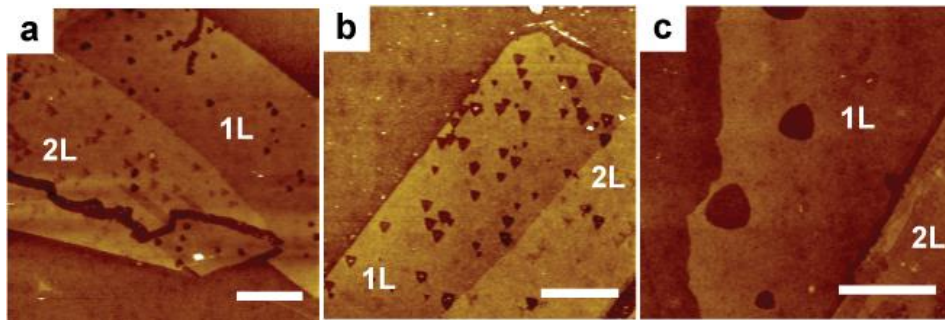


Figure 7.10: AFM images of single- and bi-layer MoS₂ oxidized at various temperatures. (a) 300 °C for 4 hours, (b) 320 °C for 3 hours, and (c) 340 °C for 2 hours. The scale bars are 2 μm.

7.9d shows an example of a large pit density of $\sim 10^9 \text{ cm}^{-2}$ observed on 8- and 9-layer MoS₂. These observations suggest that the density of pits formed upon oxidation has no obvious correlation with MoS₂ thickness but shows significant sample-to-sample variations.

Figures 7.10a-c show AFM images of single- and bi-layer MoS₂ after oxidation at 300 °C for 4 hours, 320 °C for 3 hours, and 340 °C for 2 hours, respectively. Higher-temperature oxygen annealing leads to larger etch pits on the surfaces. However, the density of pits on single-layer MoS₂ oxidized at 340 °C is one order of magnitude smaller than when oxidized at 300 °C and 320 °C. Hence, the density of pits exhibits no obvious simple correlation with the oxidation temperature.

The observed oxidative behaviors of atomically thin MoS₂ on SiO₂ are in sharp contrast with oxidation of graphene supported on the same SiO₂ surface. Oxygen treatment of graphene on SiO₂ results in circular etch pits on the surface [137]. However, unlike atomically thin MoS₂, the oxidative etching of SiO₂-supported graphene is strongly thickness-dependent, with single-layer being the most reactive. Furthermore, the etch pits in single-layer graphene on SiO₂ form homogeneously on

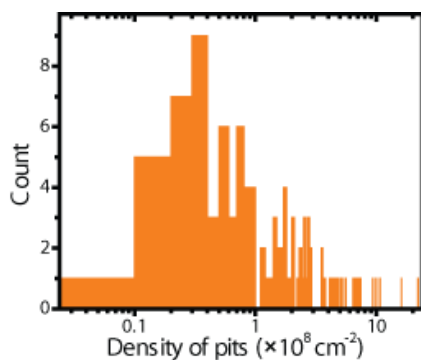


Figure 7.11: Histogram of the density of pits formed on single- and few-layer MoS₂ oxidized at various temperatures.

the surface, and the number of pits increases with oxidation time and temperature. The anomalous reactivity of single-layer graphene on SiO₂ is due to charge inhomogeneity induced by charged impurities in SiO₂ [156, 172]. The effect of the charged impurities is significantly reduced with increasing graphene thickness. Thus, for thicker graphene (or graphite), the etching is predominantly activated by native defects in the crystal, and the etch pits have nearly uniform lateral sizes and are mostly one-layer deep [173].

The oxidation of atomically thin MoS₂ appears similar in character to the oxidation of graphite crystal surfaces, rather than graphene on SiO₂. We thus suppose that the oxidative etching of atomically thin MoS₂ is similarly initiated at defect sites on the surfaces. In Fig. 7.11, we show histogram of the density of pits formed on single- and few-layer MoS₂ after oxidation at various temperatures. The pit density ranges from 10⁶ to 10⁹ cm⁻², which is comparable with the previously reported density of intrinsic vacancy defects and substitutional atoms such as tungsten and vanadium in the natural MoS₂ crystal [174, 175], indicating that such defects could be responsible for initiating etching.

Previous scanning probe microscopy [158] and X-ray photoemission measurements [159] have shown that high-temperature oxidation leads to the formation of thin MoO₃ films on the basal plane surface of bulk MoS₂. The Raman investigations of microcrystalline MoS₂ have revealed that oxygen exposure results in a peak at 820 cm⁻¹ that is a stretching mode of the terminal oxygen atoms (O-M-O) in MoO₃, and the normalized intensity of the mode increases with increasing oxidation temperature above 100 °C [160].

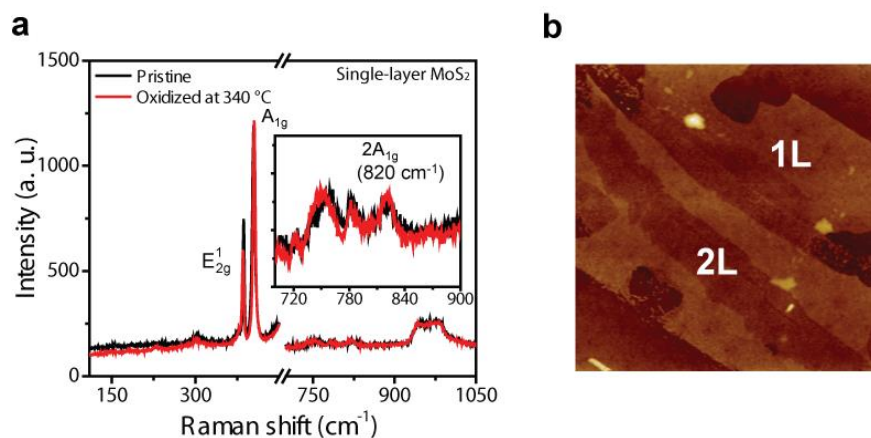


Figure 7.12: Raman spectra of oxidized atomically thin MoS₂. (a) Raman spectra of single-layer MoS₂ before (black line) and after (red line) oxidation at 340 °C for 2 hours. The inset on the right close-ups the Raman spectra near 820 cm⁻¹. (b) An AFM image of single-layer (1L) and bi-layer (2L) MoS₂. The scale bar is 1 μm.

We observe a peak at 820 cm⁻¹ in pristine single-layer MoS₂, as shown in Fig. 7.12a (black line). However, the peak intensity at 820 cm⁻¹ relative to the Si peak at ~520 cm⁻¹ rarely changes after oxygen treatment, even at 340 °C for 2 hours as shown in Fig. 7.12a (red line). Thus, the peak at 820 cm⁻¹ in oxidized MoS₂ is not the stretching mode in MoO₃ but rather the 2×A_{1g} mode of MoS₂ [176]. Hence, we conclude that no MoO₃ structure is produced in atomic layers of MoS₂ by oxygen treatment below 340 °C. This is also supported by the absence of other MoO₃-related peaks such as 285 cm⁻¹ and 995 cm⁻¹ in the Raman spectrum of oxidized MoS₂. Furthermore, we observe no signatures of MoO₃ films on the surface of atomically thin MoS₂ by AFM after oxidation below 340 °C, as shown in Fig. 7.12b.

We find that oxidation above 350 °C rapidly etches away single- and few-layer MoS₂. However, we find that high-temperature oxidation of thicker MoS₂ (> 40 nm in thickness) above 400 °C leads to significant structural and chemical modification. Figure. 7.13a is an AFM image of 40 nm-thick MoS₂ oxidized at

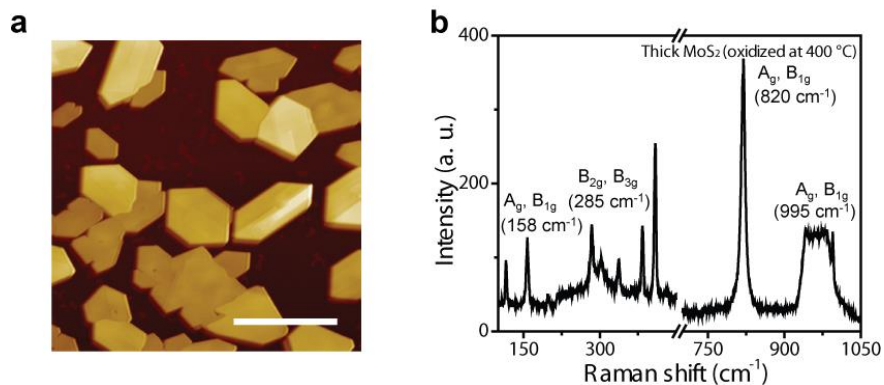


Figure 7.13: An AFM image and a Raman spectrum of thick MoS₂ oxidized at a high temperature. (a) An AFM image of oxidized thick MoS₂ crystals at 400 °C. The scale bar is 1 μm. (b) A Raman spectrum of thick MoS₂ oxidized at 400 °C for 10 minutes, showing MoO₃-related peaks.

400 °C for 10 min. The thick MoS₂ decomposes into smaller crystals with a lateral size of about 300 nm in length. The Raman spectrum of the crystal (Fig. 7.13b) shows MoO₃-related modes of 189, 285, 820, and 995 cm⁻¹ [160], corroborating that MoO₃ is formed by high-temperature oxidation of thick MoS₂

Oxygen treatment is expected to modify significantly the electronic properties of atomically thin MoS₂. Indeed, exposing few-layer MoS₂ FET devices to oxygen gas leads to considerable decrease in carrier density and conductivity [177, 178]. We investigate the effects of oxygen on the carrier concentrations in MoS₂ using Raman spectroscopy. Previous Raman measurement of single-layer MoS₂ using electrolyte gating, combined with density functional theory calculations, has revealed that the Raman A_{1g} mode downshifts and its linewidth increases with increasing electron density due to electron-phonon interactions [105]. In contrast, the E¹_{2g} phonon is less sensitive to electron concentration than the A_{1g} phonon. In Fig. 7.14a, we show the Raman E¹_{2g} and A_{1g} modes of single-layer MoS₂ before and after oxidation at

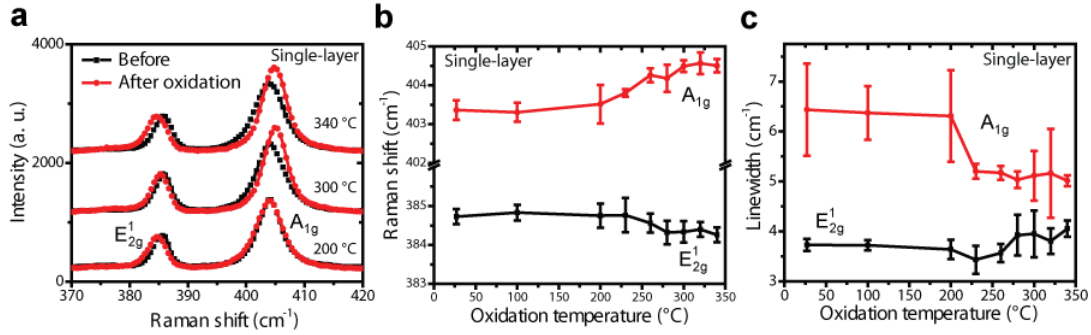


Figure 7.14: The Raman E_{2g}^1 and A_{1g} modes of oxidized single-layer MoS_2 . (a) The Raman E_{2g}^1 and A_{1g} modes of single-layer MoS_2 before (black) and after (red) oxidation at 200 °C, 300 °C, and 340 °C for 2 hours. (b-c) Frequencies (b) and linewidths (c) of the E_{2g}^1 and A_{1g} modes versus oxidation temperature.

temperatures of 200 °C, 300 °C, and 340 °C for 2 hour. Oxygen treatment above 200 °C results in the upshift of the frequency and the increase of the linewidth of the A_{1g} mode, indicating that electrons transfer from MoS_2 by oxygen treatment. Figures 7.14b and c show the frequencies and linewidths of the Raman E_{2g}^1 and A_{1g} modes as functions of the oxidation temperature. The positions of the E_{2g}^1 and the A_{1g} peaks do not shift measurably after oxygen annealing below 200 °C. However, above 200 °C, the E_{2g}^1 mode slightly decreases while the A_{1g} mode increases with temperature up to 404.5 cm^{-1} at 340 °C. Furthermore, as shown in Fig. 7.14c, the linewidth of the A_{1g} mode abruptly decreases above 200 °C, while the E_{2g}^1 mode shows nearly constant linewidth over temperature.

Although the cause of the shift in the E_{2g}^1 mode is unclear, these results suggest that below 200 °C the electron transfer upon oxidation is minor, but with increasing temperature there is sizable electron withdrawal by oxygen treatment. Using the results by Chakraborty *et al.* [105], we estimate the density of electrons withdrawn to be of order 10^{13} cm^{-2} for oxidation at 340 °C.

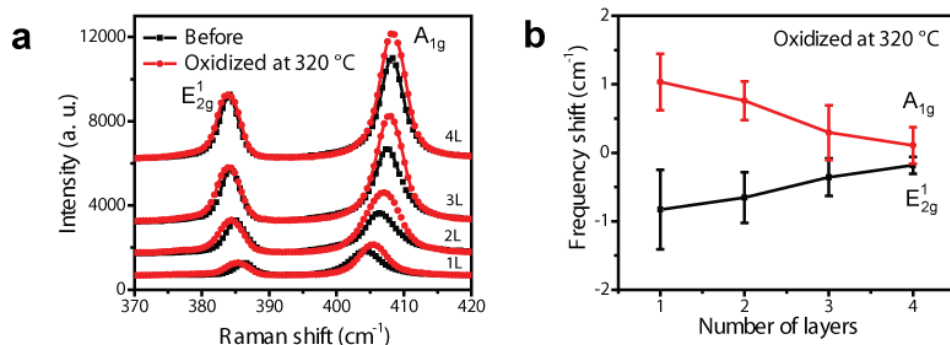


Figure 7.15: The Raman E_{2g}^1 and A_{1g} modes of oxidized single- and few-layer MoS₂. (a) Raman E_{2g}^1 and A_{1g} modes of single-layer (1L), bi-layer (2L), tri-layer (3L), and 4-layer (4L) MoS₂ after oxidation at 320 °C for 2 hours. (b) Shifts in the peak position of the E_{2g}^1 and A_{1g} modes as functions of thickness.

In Fig. 7.15a, we show the Raman E_{2g}^1 and A_{1g} modes of single-, bi-, tri-, and four-layer MoS₂ after oxidation at 320 °C for 2 hours. The oxidation results in upshift of the A_{1g} mode and downshift of the E_{2g}^1 mode of single- and few-layer MoS₂. However, as shown in Fig. 7.15b, the shifts of the E_{2g}^1 and A_{1g} modes decrease with increasing thickness. This indicates that electron transfer from atomically thin MoS₂ by oxygen treatment is a surface effect, which is consistent with observations that atomically thin MoO₃ is not formed upon oxidation below 340 °C.

7.4 Conclusions

In this chapter, we have investigated oxidative reactivity of atomically thin MoS₂ supported on SiO₂. We find that oxygen treatment of atomically thin MoS₂ results in triangular etch pits whose edges are along zigzag directions which other evidence suggest have Mo orientations. The pit density is uncorrelated with oxidation temperature, time, and MoS₂ thickness, indicating that the oxidative etching is initiated *via* intrinsic defects in MoS₂ rather than substrate effects such as charged

impurities, in contrast with graphene. The difference in reactivity between graphene and atomically thin MoS₂ is most likely because graphene is a semimetal with a linear energy dispersion but MoS₂ is an ordinary semiconductor.

We further find that oxygen exposure leads to sizable electron transfer from MoS₂ surfaces above 200 °C but produces no MoO₃ below 340 °C. Our results can provide insight into the oxidative reactivity of atomically thin MoS₂ on substrates.

Chapter 8: Conclusions and outlook

In this dissertation, I have explored experimentally how the morphology and chemical reactivity of 2D crystals are influenced by substrates.

In Chapter 5, I studied the morphology of graphene membranes supported on SiO_2 substrates decorated with SiO_2 nanoparticles. I found that when the nanoparticle density is small, graphene adheres conformally to the substrate. However, with increasing nanoparticle density, wrinkling is induced to connect the nanoparticle-induced protrusions. Above a critical nanoparticle density, the wrinkling network spans the entire sample. Furthermore, graphene delaminates from the nanoparticle-decorated substrates with increasing graphene thickness. These morphological transitions can be described within a continuum elastic model and by statistical mechanical approaches. The wrinkling and the delamination both act to remove in-plane strain in graphene. Therefore, the observations along with the theoretical results can be used to place upper limits on the magnitude of strain and, hence, pseudomagnetic fields attainable in graphene through adhesion to patterned surfaces.

There are some potentially important experiments which can be done by using nanoparticle-patterned substrates. As shown in Chapter 5, wrinkles and nanoscale-protrusions could produce sizable pseudomagnetic fields in graphene and could affect its electronic properties. To detect the signature of pseudomagnetic fields in such graphene nanostructures, we may use scanning tunneling spectroscopy [25].

Additionally, electronic transport measurements of graphene on nanoparticles are also interesting. Theoretical studies have predicted that microscopic corrugations (or ripples) of graphene could be scattering centers [38]. However, the carrier

scattering from ripples has yet to be experimentally determined and has remained controversial. The detailed investigations on the correlation between tuned roughness of graphene on nanoparticles and its electron mobility may lead to an answer to this controversial problem.

In Chapter 6, I investigated the impact of the substrates on oxidative reactivity of graphene by employing thermally-grown SiO_2 , SiO_2 nanoparticle thin films, hBN and mica as graphene supports. I found single-layer graphene on low charge-trap density hBN is not etched and shows little doping after oxygen treatment at temperatures up to 550 °C, in sharp contrast with oxidative etching under similar conditions of graphene on high charge-trap density SiO_2 and on mica. Furthermore, bilayer graphene shows reduced reactivity compared to single-layer graphene, regardless of its substrate-induced roughness. Together the observations indicate that graphene's reactivity is predominantly controlled by charge inhomogeneity-induced potential fluctuations rather than surface roughness.

The findings suggest a strategy to functionalize graphene or to manipulate dopant concentrations in graphene locally by using a patterned substrate. For example, when graphene is deposited onto SiO_2 with narrow strips of BN on it and is functionalized with oxygen molecules at a moderate temperature, graphene pnp junctions can be created. This method may be easier than fabricating top gates. Similarly, tunnel and Josephson junctions may be created by appropriate chemical functionalization of graphene on such a patterned substrate [58, 64].

Lastly, in Chapter 7, I investigated oxidative reactivity of atomically thin MoS_2 on SiO_2 . I found that exposure to oxygen at 300-340 °C results in triangular

etch pits with uniform orientation on the surfaces of atomically thin MoS₂, indicating anisotropic etching terminating on lattice planes. The triangular pits expand laterally with oxidation time. The density of pits scarcely depends on oxidation time, temperature, and MoS₂ thickness, but varies significantly from sample to sample. These observations indicate that etching is initiated at native defect sites on the basal plane surface rather than activated by substrate effects such as charged impurities, in contrast with graphene.

The results can offer insight into reactivity of atomically thin transition metal dichalcogenides. Future work will be to functionalize transition metal dichalcogenides with other chemical species such as transition metals and organic molecules. The observations of anisotropic etching suggest an approach to creating MoS₂ nanostructures with atomically well-defined edges *via* oxidation.

In conclusion, the present studies provide insight into the morphology and reactivity of 2D crystals supported on substrates and serve as an important first step toward strain- and chemical-engineering their electronic properties. A next step will be to create strain- and chemical-engineered electronic devices based on the results.

Appendix A: Scaling analysis of the wrinkle length

Here we show that X_c scales as $X_c \sim d(E_{2D}/\gamma)^{1/4}$, analogous to scaling for the diameter detachment zones surrounding a local protuberance as shown in Chapter 5. We design a scaling analysis, neglecting E_γ and E_b . The total energy is of the form

$$E_{\text{tot}} = \kappa^{-5/6} E_{2D}^{1/6} X^{1/3} [f_1(\theta) + \gamma d \kappa^{-5/6} E_{2D}^{-1/6} X^{2/3} f_2(\theta)], \quad (\text{A1})$$

where

$$f_1(\theta) = \frac{4}{3^{1/2}} (\pi - \theta) [1/\sin(\theta/2) - 1]^{2/3} \quad (\text{A2})$$

and

$$f_2(\theta) = 2 \tan \frac{\theta}{2} \quad (\text{A3})$$

The minimization of Eq. (A1) with respect to θ leads to

$$\partial_\theta f_1(\theta) + \gamma d \kappa^{-5/6} E_{2D}^{-1/6} X^{2/3} \partial_\theta f_2(\theta) = 0 \quad (\text{A4})$$

and as a consequence

$$\theta = f_3(\gamma d \kappa^{-5/6} E_{2D}^{-1/6} X^{2/3}) \quad (\text{A5})$$

As discussed in Chapter 5, the critical spacing X_c is given by a condition that $\zeta(0) = d$:

$$\begin{aligned} X_c &= d^{3/2} \frac{2^{3/2}}{3^{3/4}} \left(\frac{E_{2D}}{\kappa} \right)^{1/4} [1/\sin(\theta(X_c)/2) - 1]^{-1/2} \\ &= d^{3/2} \left(\frac{E_{2D}}{\kappa} \right)^{1/4} f_4(\theta) \\ &= d^{3/2} \left(\frac{E_{2D}}{\kappa} \right)^{1/4} f_4\left(f_3\left(\gamma d \kappa^{-5/6} E_{2D}^{-1/6} X_c^{2/3}\right)\right), \end{aligned} \quad (\text{A6})$$

where

$$f_4(\theta) = [1/\sin(\theta/2) - 1]^{-1/2}. \quad (\text{A7})$$

One can check by substitution that

$$X_c = d^{3/2} \left(\frac{E_{2D}}{\kappa} \right)^{1/4} f_6(\gamma d^2 / \kappa) \quad (\text{A8})$$

with $f_6(u) = f_5(u f_6(u)^{2/3})$ and $f_5(u) = f_4(f_3(u))$. We now define the elastic thickness $h_{el} = (\kappa/E_{2D})^{1/2}$ and the equilibrium contact curvature $C_{eq} = (2\gamma/\kappa)^{1/2}$. Letting $f_7(u) = f_6(u^2/2)$, we rewrite X_c as

$$X_c = \frac{d^{3/2}}{h_{el}^{1/2}} f_7(C_{eq} d), \quad (\text{A9})$$

which is the general scaling form of the solution.

We now consider two asymptotic limits; the strong adhesion limit $C_{eq} \gg 1$ and the weak adhesion limit $C_{eq} \ll 1$. In the strong adhesion limit, the opening angle of the wrinkle θ goes to zero. Then, one has $f_1(\theta) \sim \theta^{2/3}$ and $f_2(\theta) \sim \theta$. Hence $f_3(u) \sim u^{-3/5}$. Since $f_4(\theta) \sim \theta^{1/2}$, one has $f_5(u) = f_4(f_3(u)) \sim [f_3(u)]^{1/2} \sim u^{-3/10}$, and finally $f_6(u) \sim u^{-1/4}$.

Therefore, one has:

$$X_c \sim \frac{d^{3/2}}{h_{el}^{1/2}} (C_{eq} d)^{-1/2} \sim d (E_{2D} / \gamma)^{1/4} \quad (\text{A10})$$

and

$$\theta \sim (C_{eq} d)^{-1}, \quad (\text{A11})$$

which also confirms that the small θ limit corresponds to the large $C_{eq} d$ limit (strong adhesion limit).

Alternatively, setting $\Theta = \pi - \theta$, we redo the above scaling analysis in the weak adhesion limit $C_{eq} \ll 1$ with the argument of f_1, f_2 , and f_4 being Θ instead of θ . Then

$f_1(\Theta) \sim \Theta^{7/3}$, and $f_2(\Theta) \sim 1/\Theta$, so that $f_3(u) \sim u^{3/10}$. Also $f_4(\Theta) \sim 1/\Theta$, leading to $f_5(u) \sim u^{-3/10}$ and $f_6(u) \sim u^{-1/4}$. Consequently, we obtain

$$X_c \sim \frac{d^{3/2}}{h_{el}^{1/2}} (C_{eq}d)^{-1/2} \quad (\text{A12})$$

and

$$\theta \sim (C_{eq}d)^{1/2}. \quad (\text{A13})$$

This solution is consistent with the weak adhesion limit because $\Theta \ll 1$ implies $C_{eq}d \ll 1$.

Bibliography

1. A. K. Geim and K.S. Novoselov, *The rise of graphene*. Nature Mater. **6**, 183–191 (2007).
2. P. R. Wallace, *The band theory of graphite*. Phys. Rev. **71**, 622–634 (1947).
3. G. W. Semenoff, *Condensed-matter simulation of a three-dimensional anomaly*. Phys. Rev. Lett. **53**, 2449–2452 (1984).
4. K.S. Novoselov, A. K. Geim, S. V Morozov, D. Jiang, Y. Zhang, S. V Dubonos, I. V Grigorieva, and A. A. Firsov, *Electric field effect in atomically thin carbon films*. Science **306**, 666–669 (2004).
5. K.S. Novoselov, A. K. Geim, S. V Morozov, D. Jiang, M.I. Katsnelson, I. V Grigorieva, S. V Dubonos, and A. A. Firsov, *Two-dimensional gas of massless Dirac fermions in graphene*. Nature **438**, 197–200 (2005).
6. Y. Zhang, Y.-W. Tan, H.L. Stormer, and P. Kim, *Experimental observation of the quantum Hall effect and Berry's phase in graphene*. Nature **438**, 201–204 (2005).
7. C. Lee, X. Wei, J.W. Kysar, and J. Hone, *Measurement of the elastic properties and intrinsic strength of monolayer graphene*. Science **321**, 385–388 (2008).
8. A.A. Balandin, S. Ghosh, W. Bao, I. Calizo, D. Teweldebrhan, F. Miao, and C.N. Lau, *Superior thermal conductivity of single-layer graphene*. Nano Lett. **8**, 902–907 (2008).
9. K.S. Novoselov, D. Jiang, F. Schedin, T.J. Booth, V. V Khotkevich, S. V Morozov, and A. K. Geim, *Two-dimensional atomic crystals*. Proc. Natl. Acad. Sci. USA **102**, 10451–10453 (2005).

10. C.R. Dean, A. F. Young, I. Meric, C. Lee, L. Wang, S. Sorgenfrei, K. Watanabe, T. Taniguchi, P. Kim, K.L. Shepard, and J. Hone, *Boron nitride substrates for high-quality graphene electronics*. Nature Nanotechnol. **5**, 722–726 (2010).
11. C.R. Dean, L. Wang, P. Maher, C. Forsythe, F. Ghahari, Y. Gao, J. Katoch, M. Ishigami, P. Moon, M. Koshino, T. Taniguchi, K. Watanabe, K.L. Shepard, J. Hone, and P. Kim, *Hofstadter's butterfly and the fractal quantum Hall effect in moiré superlattices*. Nature **497**, 598-602 (2013).
12. L. A. Ponomarenko, R. V Gorbachev, G.L. Yu, D.C. Elias, R. Jalil, A. A. Patel, A. Mishchenko, A. S. Mayorov, C.R. Woods, J.R. Wallbank, M. Mucha-Kruczynski, B. A. Piot, M. Potemski, I. V Grigorieva, K.S. Novoselov, F. Guinea, V.I. Fal'ko, and A. K. Geim, *Cloning of Dirac fermions in graphene superlattices*. Nature **497**, 594-597 (2013).
13. B. Hunt, J.D. Sanchez-Yamagishi, A. F. Young, M. Yankowitz, B.J. Leroy, K. Watanabe, T. Taniguchi, P. Moon, M. Koshino, P. Jarillo-Herrero, and R.C. Ashoori, *Massive Dirac Fermions and Hofstadter Butterfly in a van der Waals Heterostructure*. Science **340**, 1427-1430 (2013).
14. B. Radisavljevic, A. Radenovic, J. Brivio, V. Giacometti, and A. Kis, *Single-layer MoS₂ transistors*. Nature Nanotechnol. **6**, 147–150 (2011).
15. S. Helveg, J. Lauritsen, E. Laegsgaard, I. Stensgaard, J. Norskov, B. Clausen, H. Topsøe, and F. Besenbacher, *Atomically thin MoS₂: A new direct-gap semiconductor*. Phys. Rev. Lett. **105**, 136805 (2010).

16. Q.H. Wang, K. Kalantar-Zadeh, A. Kis, J.N. Coleman, and M.S. Strano, *Electronics and optoelectronics of two-dimensional transition metal dichalcogenides*. Nature Nanotechnol. **7**, 699–712 (2012).
17. K.F. Mak, K. He, J. Shan, and T.F. Heinz, *Control of valley polarization in monolayer MoS₂ by optical helicity*. Nature Nanotechnol. **7**, 494–498 (2012).
18. H. Zeng, J. Dai, W. Yao, D. Xiao, and X. Cui, *Valley polarization in MoS₂ monolayers by optical pumping*. Nature Nanotechnol. **7**, 490–493 (2012).
19. S.Z. Butler, S.M. Hollen, L. Cao, Y. Cui, J.A. Gupta, H.R. Gutie, T.F. Heinz, S.S. Hong, J. Huang, A.F. Ismach, E. Johnston-halperin, M. Kuno, V. V Plashnitsa, R.D. Robinson, R.S. Ruoff, S. Salahuddin, J. Shan, L. Shi, O.M.G. Spencer, M. Terrones, W. Windl, and J.E. Goldberger, *Opportunities in two-dimensional materials beyond graphene*. ACS Nano **7**, 2898–2926 (2013).
20. M. Han, B. Özyilmaz, Y. Zhang, and P. Kim, *Energy band-gap engineering of graphene nanoribbons*. Phys. Rev. Lett. **98**, 206805 (2007).
21. A. H. Castro Neto, N.M.R. Peres, K.S. Novoselov, and A. K. Geim, *The electronic properties of graphene*. Rev. Mod. Phys. **81**, 109–162 (2009).
22. A. A. Balandin, *Thermal properties of graphene and nanostructured carbon materials*. Nature Mater. **10**, 569–581 (2011).
23. J.-H. Chen, L. Li, W.G. Cullen, E.D. Williams, and M.S. Fuhrer, *Tunable Kondo effect in graphene with defects*. Nature Phys. **7**, 535–538 (2011).
24. O. Yazyev, and L. Helm, *Defect-induced magnetism in graphene*. Phys. Rev. B **75**, 125408 (2007).

25. N. Levy, S. A. Burke, K.L. Meaker, M. Panlasigui, A. Zettl, F. Guinea, A. H. Castro Neto, and M.F. Crommie, *Strain-induced pseudo-magnetic fields greater than 300 tesla in graphene nanobubbles*. *Science* **329**, 544–547 (2010).
26. Y.-J. Yu, Y. Zhao, S. Ryu, L.E. Brus, K.S. Kim, and P. Kim, *Tuning the graphene work function by electric field effect*. *Nano Lett.* **9**, 3430–3434 (2009).
27. F. Wang, Y. Zhang, C. Tian, C. Girit, A. Zettl, M. Crommie, and Y.R. Shen, *Gate-variable optical transitions in graphene*. *Science* **320**, 206–209 (2008).
28. Z. Fei, A. S. Rodin, G.O. Andreev, W. Bao, A. S. McLeod, M. Wagner, L.M. Zhang, Z. Zhao, M. Thiemens, G. Dominguez, M.M. Fogler, A. H. Castro Neto, C.N. Lau, F. Keilmann, and D.N. Basov, *Gate-tuning of graphene plasmons revealed by infrared nano-imaging*. *Nature* **487**, 82–85 (2012).
29. J. Chen, M. Badioli, P. Alonso-González, S. Thongrattanasiri, F. Huth, J. Osmond, M. Spasenović, A. Centeno, A. Pesquera, P. Godignon, A.Z. Elorza, N. Camara, F.J. García de Abajo, R. Hillenbrand, and F.H.L. Koppens, *Optical nano-imaging of gate-tunable graphene plasmons*. *Nature* **487**, 77–81 (2012).
30. F. Schedin, A. K. Geim, S. V Morozov, E.W. Hill, P. Blake, M.I. Katsnelson, and K.S. Novoselov, *Detection of individual gas molecules adsorbed on graphene*. *Nature Mater.* **6**, 652–655 (2007).
31. N.M. Gabor, J.C.W. Song, Q. Ma, N.L. Nair, T. Taychatanapat, K. Watanabe, T. Taniguchi, L.S. Levitov, and P. Jarillo-Herrero, *Hot carrier-assisted intrinsic photoresponse in graphene*. *Science* **334**, 648–652 (2011).

32. J. Yan, M.-H. Kim, J. A. Elle, A. B. Sushkov, G.S. Jenkins, H.M. Milchberg, M.S. Fuhrer, and H.D. Drew, *Dual-gated bilayer graphene hot-electron bolometer*. *Nature Nanotechnol.* **7**, 472–478 (2012).
33. J. Martin, N. Akerman, G. Ulbricht, T. Lohmann, J.H. Smet, K. von Klitzing, and A. Yacoby, *Observation of electron–hole puddles in graphene using a scanning single-electron transistor*. *Nature Phys.* **4**, 144–148 (2007).
34. Y. Zhang, V.W. Brar, C. Girit, A. Zettl, and M.F. Crommie, *Origin of spatial charge inhomogeneity in graphene*. *Nature Phys.* **5**, 722–726 (2009).
35. M. Ishigami, J.H. Chen, W.G. Cullen, M.S. Fuhrer, and E.D. Williams, *Atomic structure of graphene on SiO₂*. *Nano Lett.* **7**, 1643–1648 (2007).
36. E. Stolyarova, K.T. Rim, S. Ryu, J. Maultzsch, P. Kim, L.E. Brus, T.F. Heinz, M.S. Hybertsen, and G.W. Flynn, *High-resolution scanning tunneling microscopy imaging of mesoscopic graphene sheets on an insulating surface*. *Proc. Natl. Acad. Sci. USA.* **104**, 9209–9212 (2007).
37. J.-H. Chen, C. Jang, S. Adam, M.S. Fuhrer, E.D. Williams, and M. Ishigami, *Charged-impurity scattering in graphene*. *Nature Phys.* **4**, 377–381 (2008).
38. M.I. Katsnelson and A. K. Geim, *Electron scattering on microscopic corrugations in graphene*. *Phil. Trans. R. Soc. A* **366**, 195–204 (2008).
39. N. M. R. Peres, *Colloquium: The transport properties of graphene: An introduction*. *Rev. Mod. Phys.* **82**, 2673–2700 (2010).
40. X. Li, X. Wang, L. Zhang, S. Lee, and H. Dai, *Chemically derived, ultrasmooth graphene nanoribbon semiconductors*. *Science* **319**, 1229–1232 (2008).

41. Z.H. Ni, T. Yu, Y.H. Lu, Y.Y. Wang, Y.P. Feng, and Z.X. Shen, *Uniaxial strain on graphene : Raman spectroscopy study and band-gap opening*. ACS Nano **2**, 2301–2305 (2008).
42. G. Giovannetti, P. Khomyakov, G. Brocks, P. Kelly, and J. van den Brink, *Substrate-induced band gap in graphene on hexagonal boron nitride: Ab initio density functional calculations*. Phys. Rev. B **76**, 073103 (2007).
43. Y. Zhang, T.-T. Tang, C. Girit, Z. Hao, M.C. Martin, A. Zettl, M.F. Crommie, Y.R. Shen, and F. Wang, *Direct observation of a widely tunable bandgap in bilayer graphene*. Nature **459**, 820–823 (2009).
44. K. Mak, C. Lui, J. Shan, and T. Heinz, *Observation of an electric-field-induced band gap in bilayer graphene by infrared spectroscopy*. Phys. Rev. Lett. **102**, 256405 (2009).
45. K.I. Bolotin, K.J. Sikes, Z. Jiang, M. Klima, G. Fudenberg, J. Hone, P. Kim, and H.L. Stormer, *Ultrahigh electron mobility in suspended graphene*. Solid State Commun. **146**, 351–355 (2008).
46. X. Du, I. Skachko, A. Barker, and E.Y. Andrei, *Approaching ballistic transport in suspended graphene*. Nature Nanotechnol. **3**, 491–495 (2008).
47. A. F. Young and P. Kim, *Quantum interference and Klein tunnelling in graphene heterojunctions*. Nature Phys. **5**, 222–226 (2009).
48. N. Stander, B. Huard, and D. Goldhaber-Gordon, *Evidence for klein tunneling in graphene p-n junctions*. Phys. Rev. Lett. **102**, 026807 (2009).

49. K.S. Novoselov, Z. Jiang, Y. Zhang, S. V Morozov, H.L. Stormer, U. Zeitler, J.C. Maan, G.S. Boebinger, P. Kim, and A.K. Geim, *Room-temperature quantum hall effect in graphene*. *Science* **315**, 1379 (2007).
50. J. Mañes, *Symmetry-based approach to electron-phonon interactions in graphene*. *Phys. Rev. B* **76**, 045430 (2007).
51. H. Suzuura and T. Ando, *Phonons and electron-phonon scattering in carbon nanotubes*. *Phys. Rev. B* **65**, 235412 (2002).
52. M. Gibertini, A. Tomadin, M. Polini, A. Fasolino, and M.I. Katsnelson, *Electron density distribution and screening in rippled graphene sheets*. *Phys. Rev. B* **81**, 125437 (2010).
53. L. D. Landau and E. M. Lifshitz, *Theory of Elasticity*. (Pergamon Press, New York, 1970).
54. V. Pereira and A. Castro Neto, *Strain engineering of graphene's electronic structure*. *Phys. Rev. Lett.* **103**, 046801 (2009).
55. F. Guinea, M. I. Katsnelson, A. K. Geim, *Energy gaps and a zero-field quantum Hall effect in graphene by strain engineering*. *Nature Phys.* **6**, 30–33 (2009).
56. N.N. Klimov, S. Jung, S. Zhu, T. Li, C.A. Wright, S.D. Solares, D.B. Newell, N.B. Zhitenev, and J. A. Stroschio, *Electromechanical properties of graphene drumheads*. *Science* **336**, 1557–1561 (2012).
57. K. Balasubramanian and M. Burghard, *Chemically functionalized carbon nanotubes*. *Small* **1**, 180–192 (2005).
58. D. C. Elias, R. R. Nair, T. M. G. Mohiuddin, S. V. Morozov, P. Blake, M. P. Halsall, A. C. Ferrari, D. W. Boukhvalov, M. I. Katsnelson, A. K. Geim, and K. S.

- Novoselov, *Control of graphene's properties by reversible hydrogenation: Evidence for graphane*. *Science* **323**, 610–613 (2009).
59. R.R. Nair, W. Ren, R. Jalil, I. Riaz, V.G. Kravets, L. Britnell, P. Blake, F. Schedin, A.S. Mayorov, S. Yuan, M.I. Katsnelson, H.-M. Cheng, W. Strupinski, L.G. Bulusheva, A. V Okotrub, I. V Grigorieva, A.N. Grigorenko, K.S. Novoselov, and A.K. Geim, *Fluorographene: A two-dimensional counterpart of Teflon*. *Small* **6**, 2877–2884 (2010).
60. J.T. Robinson, J.S. Burgess, C.E. Junkermeier, S.C. Badescu, T.L. Reinecke, F.K. Perkins, M.K. Zalalutdniov, J.W. Baldwin, J.C. Culbertson, P.E. Sheehan, and E.S. Snow, *Properties of fluorinated graphene films*. *Nano Lett.* **10**, 3001–3005 (2010).
61. S. Niyogi, E. Bekyarova, M.E. Itkis, H. Zhang, K. Shepperd, J. Hicks, M. Sprinkle, C. Berger, C.N. Lau, W. A. deHeer, E.H. Conrad, and R.C. Haddon, *Spectroscopy of covalently functionalized graphene*. *Nano Lett.* **10**, 4061–4066 (2010).
62. C.-J. Shih, Q.H. Wang, Z. Jin, G.L.C. Paulus, D. Blankschtein, P. Jarillo-Herrero, and M.S. Strano, *Disorder imposed limits of mono- and bilayer graphene electronic modification using covalent chemistry*. *Nano Lett.* **13**, 809–817 (2013).
63. R.R. Nair, M. Sepioni, I.-L. Tsai, O. Lehtinen, J. Keinonen, A. V. Krasheninnikov, T. Thomson, A. K. Geim, and I. V. Grigorieva, *Spin-half paramagnetism in graphene induced by point defects*. *Nature Phys.* **8**, 199–202 (2012).
64. G. Profeta, M. Calandra, and F. Mauri, *Phonon-mediated superconductivity in graphene by lithium deposition*. *Nature Phys.* **8**, 131–134 (2012).

65. V. Georgakilas, M. Otyepka, A.B. Bourlinos, V. Chandra, N. Kim, K.C. Kemp, P. Hobza, R. Zboril, and K.S. Kim, *Functionalization of graphene: covalent and non-covalent approaches, derivatives and applications*. Chem. Rev. **112**, 6156–6214 (2012).
66. Y. Ding, Y. Wang, J. Ni, L. Shi, S. Shi, and W. Tang, *First principles study of structural, vibrational and electronic properties of graphene-like MX_2 ($M=Mo, Nb, W, Ta$; $X=S, Se, Te$) monolayers*. Physica B Cond. Matt. **406**, 2254–2260 (2011).
67. D. Xiao, G.-B. Liu, W. Feng, X. Xu, and W. Yao, *Coupled spin and valley physics in monolayers of MoS_2 and other group-VI dichalcogenides*. Phys. Rev. Lett. **108**, 196802 (2012).
68. M. Chhowalla, H.S. Shin, G. Eda, L.-J. Li, K.P. Loh, and H. Zhang, *The chemistry of two-dimensional layered transition metal dichalcogenide nanosheets*. Nature Chem. **5**, 263–275 (2013).
69. C. Ataca and S. Ciraci, *Functionalization of single-layer MoS_2 honeycomb structures*. J. Phys. Chem. C **115**, 13303–13311 (2011).
70. H. Li, Z. Yin, Q. He, H. Li, X. Huang, G. Lu, D.W.H. Fam, A.I.Y. Tok, Q. Zhang, and H. Zhang, *Fabrication of single- and multilayer MoS_2 film-based field-effect transistors for sensing NO at room temperature*. Small **8**, 63–67 (2012).
71. F.K. Perkins, a L. Friedman, E. Cobas, P.M. Campbell, G.G. Jernigan, and B.T. Jonker, *Chemical vapor sensing with monolayer MoS_2* . Nano Lett. **13**, 668–673 (2013).
72. W. O. Winer, *Molybdenum disulfide as a lubricant: A Review of the Fundamental Knowledge*. Wear **10**, 422–452 (1967).

73. B. Hinnemann, P.G. Moses, J. Bonde, K.P. Jørgensen, J.H. Nielsen, S. Horch, I. Chorkendorff, and J.K. Nørskov, *Biomimetic hydrogen evolution: MoS₂ nanoparticles as catalyst for hydrogen evolution*. J. Am. Chem. Soc. **127**, 5308–5309 (2005).
74. X. Du, I. Skachko, F. Duerr, A. Luican, and E.Y. Andrei, *Fractional quantum Hall effect and insulating phase of Dirac electrons in graphene*. Nature **462**, 192–195 (2009).
75. K.I. Bolotin, F. Ghahari, M.D. Shulman, H.L. Stormer, and P. Kim, *Observation of the fractional quantum Hall effect in graphene*. Nature **462**, 196–199 (2009).
76. X. Li, G. Zhang, X. Bai, X. Sun, X. Wang, E. Wang, and H. Dai, *Highly conducting graphene sheets and Langmuir-Blodgett films*. Nature Nanotechnol. **3**, 538–542 (2008).
77. Y. Hernandez, V. Nicolosi, M. Lotya, F.M. Blighe, Z. Sun, S. De, I.T. McGovern, B. Holland, M. Byrne, Y.K. Gun'Ko, J.J. Boland, P. Niraj, G. Duesberg, S. Krishnamurthy, R. Goodhue, J. Hutchison, V. Scardaci, A.C. Ferrari, and J.N. Coleman, *High-yield production of graphene by liquid-phase exfoliation of graphite*. Nature Nanotechnol. **3**, 563–568 (2008).
78. J.N. Coleman, M. Lotya, A. O'Neill, S.D. Bergin, P.J. King, U. Khan, K. Young, A. Gaucher, S. De, R.J. Smith, I. V Shvets, S.K. Arora, G. Stanton, H.-Y. Kim, K. Lee, G.T. Kim, G.S. Duesberg, T. Hallam, J.J. Boland, J.J. Wang, J.F. Donegan, J.C. Grunlan, G. Moriarty, A. Shmeliov, R.J. Nicholls, J.M. Perkins, E.M. Grievson, K. Theuwissen, D.W. McComb, P.D. Nellist, and V. Nicolosi, *Two-dimensional nanosheets produced by liquid exfoliation of layered materials*. Science **331**, 568–571 (2011).

79. K. V Emtsev, A. Bostwick, K. Horn, J. Jobst, G.L. Kellogg, L. Ley, J.L. McChesney, T. Ohta, S. a Reshanov, J. Röhrl, E. Rotenberg, A.K. Schmid, D. Waldmann, H.B. Weber, and T. Seyller, *Towards wafer-size graphene layers by atmospheric pressure graphitization of silicon carbide*. *Nature Mater.* **8**, 203–207 (2009).
80. A. Reina, X. Jia, J. Ho, D. Nezich, H. Son, V. Bulovic, M.S. Dresselhaus, and J. Kong, *Large area, few-layer graphene films on arbitrary substrates by chemical vapor deposition*. *Nano Lett.* **9**, 30–35 (2009).
81. K.S. Kim, Y. Zhao, H. Jang, S.Y. Lee, J.M. Kim, K.S. Kim, J.-H. Ahn, P. Kim, J.-Y. Choi, and B.H. Hong, *Large-scale pattern growth of graphene films for stretchable transparent electrodes*. *Nature* **457**, 706–710 (2009).
82. X. Li, W. Cai, J. An, S. Kim, J. Nah, D. Yang, R. Piner, A. Velamakanni, I. Jung, E. Tutuc, S.K. Banerjee, L. Colombo, and R.S. Ruoff, *Large-area synthesis of high-quality and uniform graphene films on copper foils*. *Science* **324**, 1312–1314 (2009).
83. Y. Shi, C. Hamsen, X. Jia, K.K. Kim, A. Reina, M. Hofmann, A.L. Hsu, K. Zhang, H. Li, Z.-Y. Juang, M.S. Dresselhaus, L.-J. Li, and J. Kong, *Synthesis of few-layer hexagonal boron nitride thin film by chemical vapor deposition*. *Nano Lett.* **10**, 4134–4139 (2010).
84. Y.-H. Lee, X.-Q. Zhang, W. Zhang, M.-T. Chang, C.-T. Lin, K.-D. Chang, Y.-C. Yu, J.T.-W. Wang, C.-S. Chang, L.-J. Li, and T.-W. Lin, *Synthesis of large-area MoS₂ atomic layers with chemical vapor deposition*. *Adv. Mater.* **24**, 2320–2325 (2012).
85. K.-K. Liu, W. Zhang, Y.-H. Lee, Y.-C. Lin, M.-T. Chang, C.-Y. Su, C.-S. Chang, H. Li, Y. Shi, H. Zhang, C.-S. Lai, and L.-J. Li, *Growth of large-area and highly*

- crystalline MoS₂ thin layers on insulating substrates*. Nano Lett. **12**, 1538–1544 (2012).
86. N. Petrone, C.R. Dean, I. Meric, A.M. van der Zande, P.Y. Huang, L. Wang, D. Muller, K.L. Shepard, and J. Hone, *Chemical vapor deposition-derived graphene with electrical performance of exfoliated graphene*. Nano Lett. **12**, 2751–2756 (2012).
87. A.M. van der Zande, P.Y. Huang, D. A. Chenet, T.C. Berkelbach, Y. You, G.-H. Lee, T.F. Heinz, D.R. Reichman, D. A. Muller, and J.C. Hone, *Grains and grain boundaries in highly crystalline monolayer molybdenum disulphide*. Nature Mater. **12**, 554–561 (2013).
88. F. J. Giessibl, *Advances in atomic force microscopy*. Rev. Mod. Phys. **75**, 949-983 (2003).
89. A. Jorio, M. S. Dresselhaus, R. Saito, G. Dresselhaus, *Raman Spectroscopy in Graphene Related Systems*. (WILEY-VCH, 2011)
90. L.M. Malard, M. A. Pimenta, G. Dresselhaus, and M.S. Dresselhaus, *Raman spectroscopy in graphene*. Phys. Rep. **473**, 51–87 (2009).
91. A. C. Ferrari, J.C. Meyer, V. Scardaci, C. Casiraghi, M. Lazzeri, F. Mauri, S. Piscanec, D. Jiang, K.S. Novoselov, S. Roth, and A. K. Geim, *Raman spectrum of graphene and graphene Layers*. Phys. Rev. Lett. **97**, 187401 (2006).
92. C.H. Lui, Z. Li, K.F. Mak, E. Cappelluti, and T.F. Heinz, *Observation of an electrically tunable band gap in trilayer graphene*. Nature Phys. **7**, 944–947 (2011).
93. W. Bao, L. Jing, J. Velasco, Y. Lee, G. Liu, D. Tran, B. Standley, M. Aykol, S.B. Cronin, D. Smirnov, M. Koshino, E. McCann, M. Bockrath, and C.N. Lau, *Stacking-*

- dependent band gap and quantum transport in trilayer graphene.* Nature Phys. **7**, 948–952 (2011).
94. L. Zhang, Y. Zhang, J. Camacho, M. Khodas, and I. Zaliznyak, *The experimental observation of quantum Hall effect of $l=3$ chiral quasiparticles in trilayer graphene.* Nature Phys. **7**, 953–957 (2011).
95. C.H. Lui, Z. Li, Z. Chen, P. V Klimov, L.E. Brus, and T.F. Heinz, *Imaging stacking order in few-layer graphene.* Nano Lett. **11**, 164–169 (2011).
96. C. Cong, T. Yu, K. Sato, J. Shang, R. Saito, G. F. Dresselhaus, M. S. Dresselhaus, *Raman characterization of ABA- and ABC-stacked trilayer graphene.* ACS Nano **5** 8760–8768 (2011).
97. W. Kohn, *Image of the Fermi surface in the vibration spectrum of a metal.* Phys. Rev. Lett. **2**, 1958–1959 (1959).
98. M. Lazzeri and F. Mauri, *Nonadiabatic Kohn anomaly in a doped graphene monolayer.* Phys. Rev. Lett. **97**, 266407 (2006).
99. S. Pisana, M. Lazzeri, C. Casiraghi, K.S. Novoselov, A. K. Geim, A.C. Ferrari, and F. Mauri, *Breakdown of the adiabatic Born-Oppenheimer approximation in graphene.* Nature Mater. **6**, 198–201 (2007).
100. J. Yan, Y. Zhang, P. Kim, and A. Pinczuk, *Electric field effect tuning of electron-phonon coupling in graphene.* Phys. Rev. Lett. **98**, 166802 (2007).
101. A. Das, S. Pisana, B. Chakraborty, S. Piscanec, S.K. Saha, U. V Waghmare, K.S. Novoselov, H.R. Krishnamurthy, A. K. Geim, A. C. Ferrari, and A. K. Sood, *Monitoring dopants by Raman scattering in an electrochemically top-gated graphene transistor.* Nature Nanotechnol. **3**, 210–215 (2008).

102. M.M. Lucchese, F. Stavale, E.H.M. Ferreira, C. Vilani, M.V.O. Moutinho, R.B. Capaz, C. A. Achete, and A. Jorio, *Quantifying ion-induced defects and Raman relaxation length in graphene*. Carbon **48**, 1592–1597 (2010).
103. L.G. Cançado, A. Jorio, E.H.M. Ferreira, F. Stavale, C. A. Achete, R.B. Capaz, M.V.O. Moutinho, A. Lombardo, T.S. Kulmala, and A. C. Ferrari, *Quantifying defects in graphene via Raman spectroscopy at different excitation energies*. Nano Lett. **11**, 3190–3196 (2011).
104. C. Lee, H. Yan, L.E. Brus, T.F. Heinz, J. Hone, and S. Ryu, *Anomalous Lattice Vibrations of Single- and Few-Layer MoS₂*. ACS Nano **4**, 2695–2700 (2010).
105. B. Chakraborty, A. Bera, D.V.S. Muthu, S. Bhowmick, U. V. Waghmare, and A. K. Sood, *Symmetry-dependent phonon renormalization in monolayer MoS₂ transistor*. Phys. Rev. B **85**, 161403 (2012).
106. A. Fasolino, J. H. Los, and M. I. Katsnelson, *Intrinsic ripples in graphene*. Nature Mater. **6**, 858–861 (2007).
107. C. H. Lui, L. Liu, K. F. Mak, G. W. Flynn, and T. F. Heinz, *Ultraflat graphene*. Nature **462**, 339–341 (2009).
108. J. Xue, J. Sanchez-Yamagishi, D. Bulmash, P. Jacquod, A. Deshpande, K. Watanabe, T. Taniguchi, P. Jarillo-Herrero, and B.J. LeRoy, *Scanning tunnelling microscopy and spectroscopy of ultra-flat graphene on hexagonal boron nitride*. Nature Mater. **10**, 282–285 (2011).
109. Y. Wang, V.W. Brar, W. Regan, H. Tsai, Q. Wu, W. Gannett, A. Zettl, and M.F. Crommie, *Local electronic properties of graphene on a BN substrate via scanning tunneling microscopy*. Nano Lett. **11**, 2291–2295 (2011).

110. W.G. Cullen, M. Yamamoto, K.M. Burson, J.H. Chen, C. Jang, L. Li, M.S. Fuhrer, and E.D. Williams, *High-fidelity conformation of graphene to SiO₂ topographic features*. Phys. Rev. Lett. **105**, 215504 (2010).
111. Y. Huang, J. Wu, and K. Hwang, *Thickness of graphene and single-wall carbon nanotubes*. Phys. Rev. B **74**, 245413 (2006).
112. O. Pierre-Louis, *Adhesion of membranes and filaments on rippled surfaces*. Phys. Rev. E **78**, 021603 (2008).
113. T. Li, and Z. Zhang, *Snap-through instability of graphene on substrates*. Nano. Res. Lett. **5**, 169–173 (2009).
114. Z. H. Aitken and R. Huang, *Effects of mismatch strain and substrate surface corrugation on morphology of supported monolayer graphene*. J. Appl. Phys. **107**, 123531 (2010).
115. S. Viola Kusminskiy, D. K. Campbell, A. H. Castro Neto, and F. Guinea, *Pinning of a two-dimensional membrane on top of a patterned substrate: The case of graphene*. Phys. Rev. B **83**, 165405 (2011).
116. T. J. W. Wagner and D. Vella *The sensitivity of graphene “snap-through” to substrate geometry*. Appl. Phys. Lett. **100**, 233111 (2012).
117. Z. Li, Z. Cheng, R. Wang, Q. Li, and Y. Fang, *Spontaneous formation of nanostructures in graphene*. Nano Lett. **9**, 3599–3602 (2009).
118. S. Scharfenberg, D.Z. Rocklin, C. Chialvo, R.L. Weaver, P.M. Goldbart, and N. Mason, *Probing the mechanical properties of graphene using a corrugated elastic substrate*. Appl. Phys. Lett. **98**, 091908 (2011).

119. S. Scharfenberg, N. Mansukhani, C. Chialvo, R. L. Weaver, and N. Mason, *Observation of a snap-through instability in graphene*. Appl. Phys. Lett. **100**, 021910 (2012).
120. S. N. Magonov, V. Elings, M. -H. Whangbo, *Phase imaging and stiffness in tapping-mode atomic force microscopy*. Surf. Sci. **375**, L385–L391 (1997).
121. A. Lobkovsky, S. Gentges, H. Li, D. Morse, and T.A. Witten, *Scaling properties of stretching ridges in a crumpled elastic sheet*. Science **270**, 1482–1485 (1995).
122. S. P. Koenig, N. G. Boddeti, M. L. Dunn, and J. S. Bunch, *Ultrastrong adhesion of graphene membranes*. Nature Nanotechnol. **6**, 543–546 (2011).
123. D. L. Blair and A. Kudrolli, *Geometry of crumpled paper*. Phys. Rev. Lett. **94**, 166107 (2005).
124. E. Sultan and A. Boudaoud, *Statistics of crumpled paper*. Phys. Rev. Lett. **96**, 136103 (2006).
125. C. André Andresen and A. Hansen, *Ridge network in crumpled paper*. Phys. Rev. E **76**, 026108 (2007).
126. J. Nicolle, D. Machon, P. Poncharal, O. Pierre-Louis, and A. San-Miguel, *Pressure-mediated doping in graphene*. Nano Lett. **11**, 3564–3568 (2011).
127. M. Poot, and H. S. J. van der Zant, *Nanomechanical properties of few-layer graphene membranes*. Appl. Phys. Lett. **92**, 063111 (2008).
128. E. Schwerin, *Über Spannungen und Formänderungen Kreisringförmiger Membranen*. Z. Angew. Math. Mech. **9**, 482 (1929).

129. U. Komaragiri, M. R. Begley, and J. G. Simmonds, *The mechanical response of freestanding circular elastic films under point and pressure loads*. J. Appl. Mech. **72**, 203 (2005).
130. V. M. Pereira, A. H. Castro Neto, H. Y. Liang, and L. Mahadevan, *Geometry, mechanics, and electronics of singular structures and wrinkles in graphene*. Phys. Rev. Lett. **105**, 156603 (2010).
131. M. Barbier, G. Papp, and F. M. Peeters, *Snake states and Klein tunneling in a graphene Hall bar with a pn-junction*. Appl. Phys. Lett. **100**, 163121 (2012).
132. M. Neek-Amal, L. Covaci, and F. M. Peeters, *Nanoengineered nonuniform strain in graphene using nanopillars*. Phys. Rev. B **86**, 041405 (2012).
133. D. L. González, and T. L. Einstein, *Voronoi cell patterns: Theoretical model and applications*. Phys. Rev. E **84**, 051135 (2011).
134. D. Stauffer and A. Aharony, *Introduction to percolation theory*. (Taylor and Francis, Washington, DC, 1992).
135. E. T. Gawlinski and H. E. Stanley, *Continuum percolation in two dimensions: Monte Carlo tests of scaling and universality for non-interacting discs*. J. Phys. A **291**, L291 (1981).
136. D. W. Boukhvalov and M. I. Katsnelson, *Chemical functionalization of graphene with defects*. Nano Lett. **8**, 4373–4379 (2008).
137. L. Liu, S. Ryu, M.R. Tomasik, E. Stolyarova, N. Jung, M.S. Hybertsen, M.L. Steigerwald, L.E. Brus, and G.W. Flynn, *Graphene oxidation: thickness-dependent etching and strong chemical doping*. Nano Lett. **8**, 1965–1970 (2008).

138. R. Sharma, J. H. Baik, C. J. Perera, M. S. Strano, *Anomalously large reactivity of single graphene layers and edges toward electron transfer chemistries*. Nano Lett. **10**, 398–405 (2010).
139. F. M. Koehler, A. Jacobsen, K. Ensslin, C. Stampfer, and W. J. Stark, *Selective chemical modification of graphene surfaces: distinction between single- and bilayer graphene*. Small **6**, 1125–1130 (2010).
140. Y.-W. Tan, Y. Zhang, K. Bolotin, Y. Zhao, S. Adam, E.H. Hwang, S. Das Sarma, H.L. Stormer, and P. Kim, *Measurement of Scattering Rate and Minimum Conductivity in Graphene*. Phys. Rev. Lett. **99**, 246803 (2007).
141. C. Jang, S. Adam, J.-H. Chen, E.D. Williams, S. Das Sarma, and M.S. Fuhrer, *Tuning the Effective Fine Structure Constant in Graphene: Opposing Effects of Dielectric Screening on Short- and Long-Range Potential Scattering*. Phys. Rev. Lett. **101**, 146805 (2008).
142. S. Adam and S. Das Sarma, *Boltzmann transport and residual conductivity in bilayer graphene*. Phys. Rev. B **77**, 115436 (2008).
143. K. Kjems, K. Carneiro, and G. Richards, *Charge Distribution in c Direction in Lamellar Graphite Acceptor Intercalation Compounds*. Phys. Rev. **41**, 763–767 (1978).
144. S. S. Datta, D. R. Strachan, E. J. Mele, and A. T. C. Johnson, *Surface potentials and layer charge distributions in few-layer graphene films*. Nano Lett. **9**, 7–11 (2009).
145. D. W. Boukhvalov and M. I. Katsnelson, *Enhancement of Chemical Activity in Corrugated Graphene*. J.Phys. Chem. C **113**, 14176–14178 (2009).

146. E. -A. Kim and A. H. Castro Neto, *Graphene as an electronic membrane*. EPL. **84**, 57007 (2008).
147. A. Locatelli, K.R. Knox, D. Cvetko, O. Mentès, M.A. Nin, S. Wang, M.B. Yilmaz, P. Kim, R.M. Osgood, and A. Morgante, *Corrugation in exfoliated graphene : An electron microscopy and diffraction study*. ACS Nano **4**, 4879–4889 (2010).
148. X. Fan, R. Nouchi, K. Tanigaki, *Effect of charge puddles and ripples on the chemical reactivity of single layer graphene supported by SiO₂/Si substrate*. J. Phys. Chem. C **115**, 12960–12964 (2011).
149. A. N. Rudenko, F. J. Keil, M. I. Katsnelson, and A. I. Lichtenstein, *Graphene adhesion on mica: Role of surface morphology*. Phys. Rev. B **83**, 045409 (2011).
150. L. A. Ponomarenko, R. Yang, T.M. Mohiuddin, M.I. Katsnelson, K.S. Novoselov, S. V. Morozov, A. A. Zhukov, F. Schedin, E.W. Hill, and A. K. Geim, *Effect of a High- κ Environment on Charge Carrier Mobility in Graphene*. Phys. Rev. Lett. **102**, 206603 (2009).
151. S. Ryu, L. Liu, S. Berciaud, Y.-J. Yu, H. Liu, P. Kim, G.W. Flynn, and L.E. Brus, *Atmospheric Oxygen Binding and Hole Doping in Deformed Graphene on a SiO₂ Substrate*. Nano Lett. 4944–4951 (2010).
152. P. J. Zomer, S. P. Dash, N. Tombros, and B. J. van Wees, *A transfer technique for high mobility graphene devices on commercially available hexagonal boron nitride*. Appl. Phys. Lett. **99**, 232104 (2011).
153. K. Xu, P. Cao, and J. R. Heath, *Graphene visualizes the first water adlayers on mica at ambient conditions*. Science **329**, 1188–1191 (2010).

154. R. Geick, C. H. Perry, and G. Rupprecht, *Normal Modes in Hexagonal Boron Nitride*. Phys. Rev. **146**, (1966).
155. J. Shim, C.H. Lui, T.Y. Ko, Y.-J. Yu, P. Kim, T.F. Heinz, and S. Ryu, *Water-gated charge doping of graphene induced by mica substrates*. Nano Lett. **12**, 648–654 (2012).
156. Q.H. Wang, Z. Jin, K.K. Kim, A.J. Hilmer, G.L.C. Paulus, C.-J. Shih, M.-H. Ham, J.D. Sanchez-Yamagishi, K. Watanabe, T. Taniguchi, J. Kong, P. Jarillo-Herrero, and M.S. Strano, *Understanding and controlling the substrate effect on graphene electron-transfer chemistry via reactivity imprint lithography*. Nature Chem. **4**, 724–732 (2012).
157. M. Chhowalla, and G. Amaratunga, *Thin films of fullerene-like MoS₂ nanoparticles with ultra-low friction and wear*. Nature **407**, 164–167 (2000).
158. J. Wang, K. C. Rose, and C. M. Lieber, *Load-independent friction : MoO₃ nanocrystal lubricants*. J. Phys. Chem. B **103**, 8405–8409 (1999).
159. J. R. Lince and P. P. Frantz, *Anisotropic oxidation of MoS₂ crystallites studied by angle-resolved X-ray photoelectron spectroscopy*. Tribol.Lett. **9**, 211–218 (2001).
160. B. C. Windom, W. G. Sawyer, and D. W. Hahn, *A Raman spectroscopic study of MoS₂ and MoO₃: Applications to tribological systems*. Tribol. Lett. **42**, 301–310 (2011).
161. S.-L. Li, H. Miyazaki, H. Song, H. Kuramochi, S. Nakaharai, and K. Tsukagoshi, *Quantitative Raman spectrum and reliable thickness identification for atomic layers on insulating substrates*. ACS Nano **6**, 7381–7388 (2012).

162. S. Helveg, J. Lauritsen, E. Laegsgaard, I. Stensgaard, J. Norskov, B. Clausen, H. Topsøe, and F. Besenbacher, Atomic-scale structure of single-layer MoS₂ nanoclusters. *Phys. Rev. Lett.* **84**, 951–954 (2000).
163. M. Bollinger, K. Jacobsen and J. Nørskov, *Atomic and electronic structure of MoS₂ nanoparticles*. *Phys. Rev. B* **67**, 085410 (2003).
164. A. Vojvodic, B. Hinnemann, and J. Nørskov, *Magnetic edge states in MoS₂ characterized using density-functional theory*. *Phys. Rev. B* **80**, 125416 (2009).
165. P. Moses, B. Hinnemann, H. Topsøe, and J. Nørskov, *The hydrogenation and direct desulfurization reaction pathway in thiophene hydrodesulfurization over MoS₂ catalysts at realistic conditions: A density functional study*. *J. Catal.* **248**, 188–203 (2007).
166. Y. Li, Z. Zhou, S. Zhang, and Z. Chen, *MoS₂ Nanoribbons : High stability and unusual electronic and magnetic properties*. *J. Am. Chem. Soc.* **130**, 16739–16744 (2008).
167. A. R. Botello-Méndez, F. López-Urías, M. Terrones, and H. Terrones, *Metallic and ferromagnetic edges in molybdenum disulfide nanoribbons*. *Nanotechnology* **20**, 325703 (2009).
168. J. Zhang, J.M. Soon, K.P. Loh, J. Yin, J. Ding, M.B. Sullivan, and P. Wu, *Magnetic molybdenum disulfide nanosheet films*. *Nano Lett* **7**, 2370–2376 (2007).
169. J. Kibsgaard, Z. Chen, B. N. Reinecke, T. F. Jaramillo, *Engineering the surface structure of MoS₂ to preferentially expose active edge sites for electrocatalysis*. *Nature Mater.* **11**, 963–969 (2012).

170. T.F. Jaramillo, K.P. Jørgensen, J. Bonde, J.H. Nielsen, S. Horch, and I. Chorkendorff, *Identification of active edge sites for electrochemical H₂ evolution from MoS₂ nanocatalysts*. *Science* **317**, 100–102 (2007).
171. P. Nemes-Incze, Z. Osváth, K. Kamarás, and L. P. Biró, *Anomalies in thickness measurements of graphene and few layer graphite crystals by tapping mode atomic force microscopy*. *Carbon* **46**, 1435–1442 (2008).
172. M. Yamamoto, T. L. Einstein, M. S. Fuhrer, and W. G. Cullen, *Charge inhomogeneity determines oxidative reactivity of graphene on substrates*. *ACS Nano* **6**, 8335–8341 (2012).
173. S. Lee, Y. Lee, Y. Hwang, J. Hahn, and H. Kang, *Defect-induced oxidation of graphite*. *Phys. Rev. Lett.* **82**, 217–220 (1999).
174. J. S. Ha, H. Roh, S. Park, and E. Lee, *Scanning tunneling microscopy investigation of the surfaces of natural MoS₂*. *Surf. Sci.* **315**, 62–68 (1994).
175. M. Whangbo, J. Ren, S. N. Magonov, H. Bangel, B. A. Parkinson, and A. Suna, *On the correlation between the scanning tunneling microscopy image imperfections and point defects of layered chalcogenides 2H-MX₂ (M = Mo, W; X = S, Se)*. *Surf. Sci.* **326**, 311–326 (1995).
176. J. M. Chen and C. S. Wang, *Second order Raman spectrum of MoS₂*. *Solid State Commun.* **14**, 857–860 (1974).
177. H. Qiu, L. Pan, Z. Yao, J. Li, Y. Shi, and X. Wang, *Electrical characterization of back-gated bi-layer MoS₂ field-effect transistors and the effect of ambient on their performances*. *Appl. Phys. Lett.* **100**, 123104 (2012).

178. W. Park, J. Park, J. Jang, H. Lee, H. Jeong, K. Cho, S. Hong, and T. Lee, *Oxygen environmental and passivation effects on molybdenum disulfide field effect transistors*. *Nanotechnology* **24**, 095202 (2013).